DOCTOR OF PHILOSOPHY

The interplay of sodium and voltage in the regulation of G-protein coupled receptor signalling

Vickery, Owen N.

Award date:
2018

The interplay of sodium and voltage in the regulation of G-protein coupled receptor signalling

by

Owen N Vickery

Supervisor: Dr Ulrich Zachariae

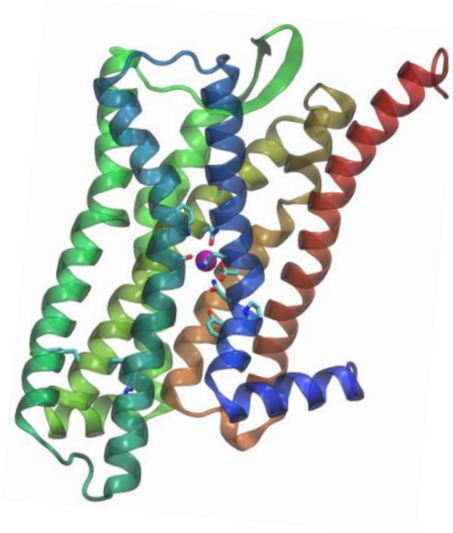

A thesis submitted for the degree of Doctor of Philosophy Dundee University - April 2018

Publications

Associated publications

Vickery ON and Zachariae U. The role of protonation changes in G-Protein Coupled Receptor activation. *In preparation*

Vickery ON, Carvalheda CA, Zaidi SA, Pisliakov AV, Katritch V and Zachariae U. (2018). Intracellular Transfer of Na^+ in an Active State G-Protein Coupled Receptor. *Structure*. 26:171–180. DOI:10.1016/j.str.2017.11.013

Vickery ON, Machtens J-P and Zachariae U. (2016). Membrane potentials regulating GPCRs: insights from experiments and molecular dynamics simulations. *Curr Opin Pharmacol*. 30:44–50. DOI:10.1016/j.coph.2016.06.011

Vickery ON, Machtens J-P, Tamburrino G, Seeliger D and Zachariae U. (2016). Structural Mechanisms of Voltage Sensing in G Protein-Coupled Receptors. *Structure*. 24(6):997–1007. DOI:10.1016/j.str.2016.04.007

Non-associated publications

Kopec W, Kopfer D, **Vickery ON**, De Groot B and Zachariae U. The Direct Coulomb Knock-On Mechanism in K^+ Channels is Intrinsically Ion-Selective. *Submitted*.

Holland CJ, MacLachlan BJ, Bianchi V, Hesketh S, Morgan R, **Vickery ON**, Bulek AM, Fuller A, Godkin A, Sewell AK, Rizkallah PJ, Wells S and Cole DK. *In Silico* and Structural Analyses Demonstrate That Intrinsic Protein Motions Guide T Cell Receptor Complementarity Determining Region Loop Flexibility. (2018). *Frontiers in Immunology*. 9:674. DOI:10.3389/fimmu.2018.00674

Tamburrino G, Llabrés S, **Vickery ON**, Pitt SJ and Zachariae U. (2017). Modulation of the Neisseria gonorrhoeae drug efflux conduit MtrE. *Scientific Reports*. 7: 17091. DOI: 10.1038/s41598-017-16995-x

Lloyd A, **Vickery ON** and Laugel B. Beyond the antigen receptor: editing the genome of T-cells for cancer adoptive cellular therapies. (2013). *Frontiers in Immunology*. DOI:10.3389/fimmu.2013.00221

Contents

List of Figures

List of Tables

Acknowledgements

I would like to express my sincere gratitude to my supervisor Dr Ulrich Zachariae for his help and patience over the years (in particular the last few weeks). I would like to thank Dr Salomé Llabrés for her help and guidance over the last couple of years. I would also like to thank Dr Thomas McWilliams and Dr Juan Bueren-Calabuig for their help and friendship over the years. Thanks to my compatriots Catarina Carvalheda, Elda Iljazi and Giulia Tamburrino for all the good times in Dundee and elsewhere. I would like to thank everyone within the Computational Biology department in particular Dr Andrei Pisliakov and Dr Rastko Sknepnek as well as all of my collaborators. Finally, I would like to thank my family for their support during my unending student life.

Declarations

I declare that this thesis is based on results obtained from research which I have personally carried out in the School of Life Sciences at University of Dundee from April 2014 to December 2017 using funding provided by the BBSRC-CASE PhD Studentship. I declare that the entire thesis is my own composition. Any work other than my own is clearly stated in the text and acknowledged with reference to any relevant investigators or contributors. This thesis has never been presented previously, in whole or in part, for the award of any higher degree. I have consulted all the references cited within the text of this thesis.

Signed Date ……

Mr Owen Niall Vickery

I confirm that Owen Niall Vickery has carried out the research under my supervision and that he has fulfilled the conditions of the relevant Ordinance and Regulations of the University of Dundee, thereby qualifying him to submit this thesis in application for the degree of Doctor of Philosophy.

Signed Date ……

Dr. Ulrich Zachariae

Abstract

Playing a central role in cell signaling, G-protein coupled receptors (GPCRs) form the largest superfamily of membrane proteins and approximately a third of all drug targets in humans. The membrane potential is one of the defining characteristics of living cells. Recent work has shown that the membrane voltage, and changes thereof, modulates signal transduction and ligand binding in GPCRs. As it may allow differential signalling patterns depending on tissue, cell type, and the excitation status of excitable cells, GPCR voltage sensitivity could have important implications for their pharmacology.

However, the structural basis of GPCR voltage sensing has remained enigmatic. Here, I present atomistic simulations on the *Rhodopsin* GPCR family, which suggest a structural and mechanistic explanation for the observed voltage-induced functional effects. The simulations reveal that the position of an internal Na^+ ion, recently detected to bind to a highly conserved aqueous pocket in receptor crystal structures, strongly responds to voltage changes. The movements of a Na^+ ion or a proton from the Na^+ binding site gives rise to gating charges in excellent agreement with previous experimental recordings.

Structural studies have revealed that inactive *Rhodopsin* GPCRs harbor a conserved binding site for Na^+ ions in the center of their transmembrane domain, accessible from the extracellular space. Here, I show that upon the activation of GPCRs, a hydrated channel is formed between the Na^+ binding pocket and the cytosol, thereby providing a conduit for Na^+ egress to the cytosol. Coupled with the protonation change of $D^{2.50}$, the Na^+ ion movement occurs without significant energy barriers, and can be driven by physiological transmembrane ion and voltage gradients. I propose that Na^+ ion exchange with the cytosol is a key step in GPCR activation. Further, I hypothesize that this transition locks receptors in long-lived active-state conformations.

Biochemical studies on GPCRs have demonstrated that their basal signalling is allosterically modulated by pH. Here, I show that the global receptor conformation of the δ-opioid receptor and two constitutive mutants is tightly tied to the protonation state of two ultra conserved aspartate residues. I describe a sequential activation pathway linking the Na^+ binding site and the $D(E)R^{3.50}Y$ motif to the activation of the receptor.

Abbreviations

5-HT	5-hydroxytryptamine
A_{2A}AR	adenosine $A2_A$ receptor
ABS	allosteric binding site
AGTR	angiotensin receptors
β_1AR	β_1 adrenergic receptor
β_2AR	β_2 adrenergic receptor
cAMP	cyclic adenosine monophosphate
CASR	calcium-sensing receptor
cGMP	cyclic guanosine monophosphate
CNS	central nervous system
CompEL	computational electrophysiology
DAG	diacylglycerol
E1	ubiquitin activating enzyme
E2	ubiquitin conjugating enzyme
E3	ubiquitin ligase
ECL	Extracellular loop
ESCRT	endosomal-sorting complex required for transport
GABAR	gamma-aminobutyric acid receptors
GDP	guanine diphosphate
GEF	GTP-exchange factor
GNRHR	gonadotropin releasing hormone receptor
GPCR	G-protein coupled receptor
GDP	guanine diphosphate
GRM	metabotropic glutamate receptors
GTP	guanine triphosphate
ICL	intracellular loop
Ins(1,4,5)P3	inositol (1,4,5)triphosphate
M2R	m2 muscarinic receptor
MD	Molecular Dynamics
NMDG	N-methyl-D-glucamine
NSF	N-ethylmaleimide-sensitive fusion protein
Par1	protease-activated receptor 1
PTH	Parathyroid hormone
PTHrP	Parathyroid hormone-related peptide
PBC	periodic boundary conditions
PI3K	phosphoinositide 3-kinase
PLA2	phospholipase A2
PLC	phospholipase C

PMF	potential of mean force
POPC	1,2-palmitoyl-oleoyl-sn-glycero-3-phosphocholine
PtdIns(3,4,5)P3	phosphatidylinositol (3,4,5)triphosphate
RMSD	root-mean-squared deviation
SSTR	somatostatin receptor
TAS1R	sweet and umami taste receptors
TBS	transient binding site
TM	transmembrane
UPS	ubiquitin proteasome system
VFTM	venus fly trap mechanism
V_m	transmembrane voltage
wt	wild type
δ-OR	δ-opioid receptor
μ-OR	μ-opioid receptor

Chapter 1. Introduction

Membrane proteins act as the initial checkpoint forming an interface between the cell and the external environment, mediating the transduction of a broad range of extracellular stimuli into a wide range of signalling cascades in the cell. The exceptional diversity of these receptors has allowed them to be sensitive to nearly every conceivable environmental stimulus: light, electrical, ionic concentrations, mechanical stresses, hormones, odorants, pH and proximity to other cells, to name but a few.

Of particular importance are G-protein coupled receptors (GPCRs), which are named after by their ability to recruit and regulate the activity of intracellular heterotrimeric G-proteins. To date, these receptors are the largest superfamily of transmembrane receptors to be discovered with more than 800 members, involved in nearly every aspect of cell signalling. Due to their intrinsic roles, signal transduction by GPCRs is fundamental for the majority of physiological processes, from taste, smell and vision to endocrine, neurological and cardiovascular functions. Owing to this remarkable diversity, they are the targets of >30% of all therapeutic drugs.

1.1 GPCR families

The extensive diversification of GPCRs allows for a functional versatility not seen in many other protein superfamilies. There are over 800 distinct genes encoding GPCRs in humans, and they are classified based on phylogenetic criteria. In 1994, Kolakowski introduced the well-known A, B, C and F classification system, used by the International Union of Pharmacology, Committee on Receptor Nomenclature and Classification (NC-IUPHAR)(1). It should be noted that classes D and E only exist in invertebrates and therefore will not be discussed further in this thesis. In 2003, this was updated by Fredriksson and colleagues to comprise of five main families. The major difference between classifications is the splitting of class B receptors into disparate families (2). The five main GPCR families (shortened to GRAFS) are: Glutamate (class C), Rhodopsin (class A), Adhesion (class B), Frizzled/Taste-2 (class F), and Secretin (class B) (Figure 1-1, Figure 1-2) (please see below for a comparison of receptor families). Throughout the text I will refer to the GPCR families using the GRAFS nomenclature together with the extended Kolakowski classification system, the families will be referred to in italics and with a capitalised first letter (*Glutamate, Rhodopsin, Adhesion, Frizzled/Taste2* and *Secretin*) to prevent confusion with the receptors e.g. secretin and rhodopsin.

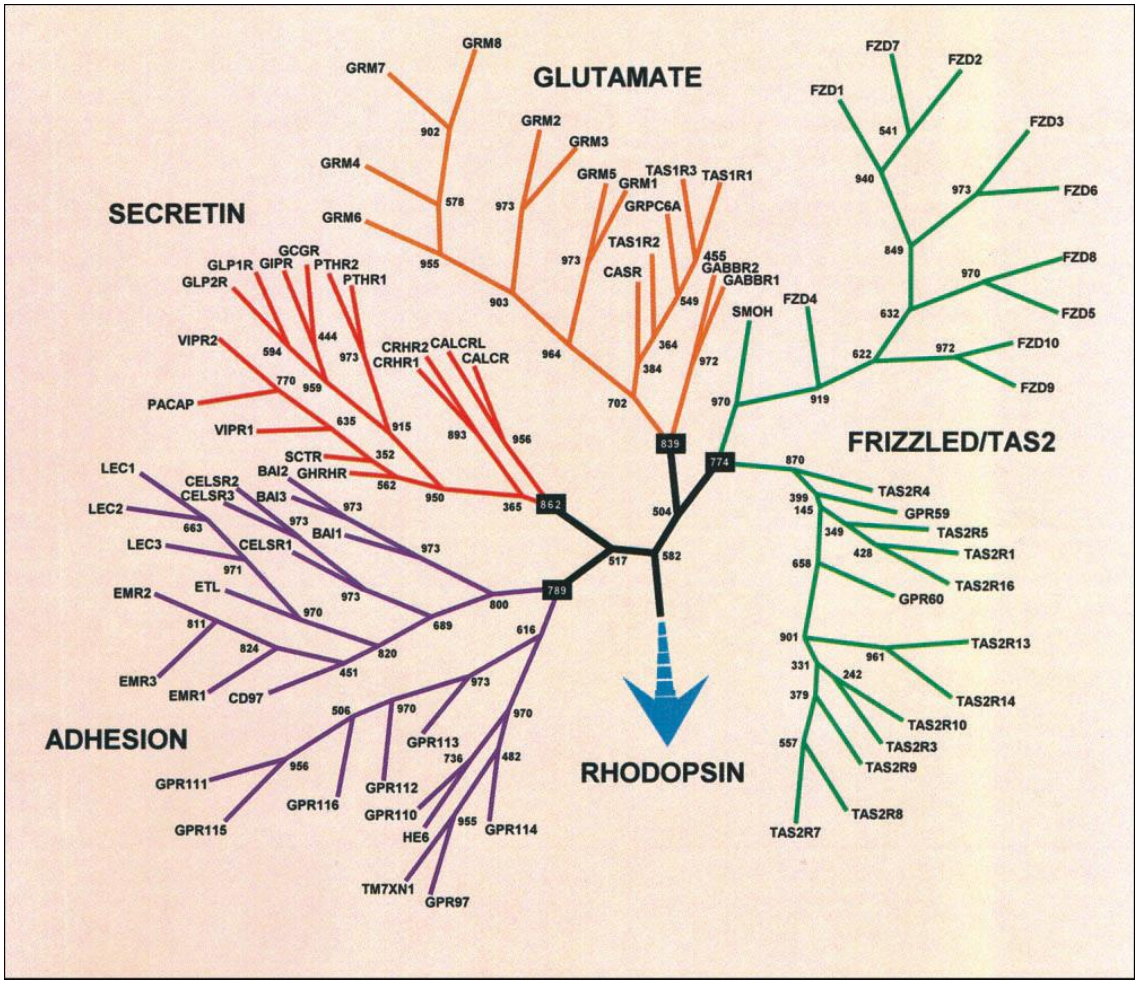

Figure 1-1: Phylogenetic relationship between GPCRs in the human genome

The tree displays four of the 5 classes of GPCRs, the fifth class Rhodopsin is displayed below in section 1.1.1. This figure was adapted from (2).

1.1.1 The Rhodopsin receptor family/class A

The largest GPCR family is the *Rhodopsin* containing over 700 receptors (3). In contrast to the other GPCR families, their diversity lies within their TM region. Whilst they contain short N-terminal domains, there are a few exceptions. The protease-activated receptors (PAR1-4) contain a cleavage site within their N-terminus, which, upon cleavage by thrombin/trypsin exposes its tethered ligand. In contrast, most *Rhodopsin* receptors are activated by interactions between the TM domains, extracellular loops and their ligand.

The *Rhodopsin* family can be further divided into four phylogenetic subgroups: α, β, γ and δ, in which the greatest variation can be seen within the α and γ subgroups. Interestingly, there is no correlation between the phylogenetic group of the receptor and the endogenous ligand (2). For example, peptide-binding receptors are found amongst all four subgroups, whilst lipid-like binding receptors are found in three of the subgroups of the *Rhodopsin* family. However, some of the subgroups bind similar ligand types. For

instance, the α subgroup is composed mainly of amine binding receptors, all receptors in the β subgroup bind peptides and the glycoproteins and nucleotide binding receptors are within the δ subgroup (2).

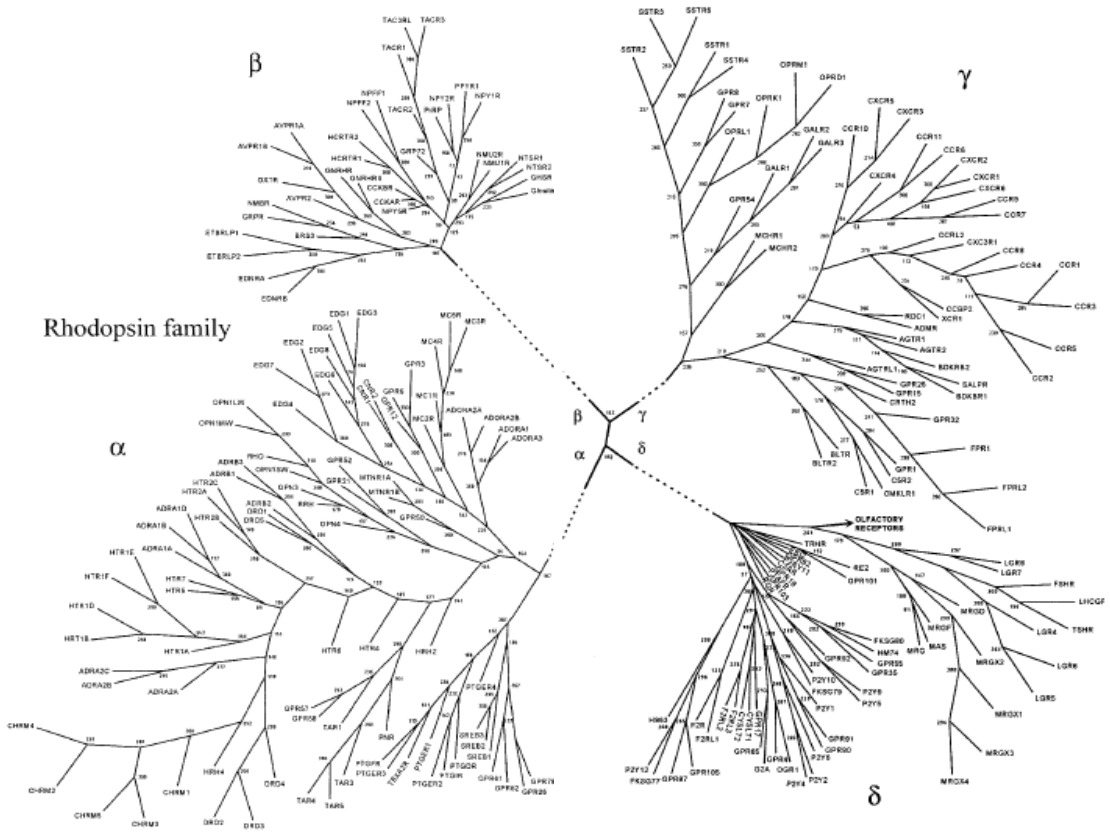

Figure 1-2: Phylogenetic relationship between the *Rhodopsin* GPCRs family in the human genome
The tree displays four subgroups of the Rhodopsin GPCR family: α, β, γ and δ. This figure was adapted from (2).

The *Rhodopsin* family to date includes most of the clinically relevant drug targets. The α subgroup contains more than 15 important drug targets including the histamine, dopamine, 5-hydroxytryptamine (5-HT), adrenoceptor, aminergic and prostanoid receptors. Current drugs, which target this subgroup are; antihistamines, antacids, cardiovascular and antipsychotics. The β subgroup mainly contains peptide-binding receptors, and is the target for a range of hormones such as: oxytocin, gonadotropin-releasing hormone and endothelin. There are relatively few drugs for the β subgroup, due to the flexibility and the number of interactions the endogenous peptide ligands have with the receptors. These are difficult to recreate artificially, and small molecules are unable to mimic the full range of interactions required for full signal transduction. The γ subgroup comprises a range of important receptors, such as the opioid, somatostatin (SSTR) and angiotensin (AGTR) receptors. The opioid receptors are predominantly targeted for the treatment of pain, whilst the AGTRs are targeted by antagonistic drugs for the treatment of hypertension. The δ subgroup predominantly contains purinergic, protease-activated, glycoprotein-binding and olfactory receptors. These *Rhodopsin* sub-families are extensively reviewed in references 2 and 4.

1.1.2 Non-Rhodopsin families

The *Secretin* family consists of only 15 members, predominantly involved in homeostatic functions. This family shares between 21% and 67% sequence identity amongst its members. Most of the variation is found within the N-terminal domain, which has been shown to be heavily involved in ligand recognition and binding by a plethora of experimental techniques. The majority of the *Secretin* family the N-terminal domain is stabilised by three highly conserved disulphide bridges (5). The *Secretin* family contains three ligand-binding domains, namely the proximal region, juxtamembrane region of the N-terminus and the extracellular loops in conjunction with TM6. Ligand binding is thought to form a bridge between the N-terminus, transmembrane domains and extracellular loops, thereby shifting the receptor conformation to a more active state (6).

The *Adhesion* family is the second largest family of GPCRs with 33 members, is separated from the *Secretin* family primarily based upon the phylogenetic analysis of the transmembrane domain as opposed to the structural differences between families. The distinction between families is further supported by the large differences in the architecture of the N-terminal domains. For instance the *Adhesion* family contain a GPCR proteolytic domain (GPS) in contrast to the *Secretin* family and the ligand preferences of the families also deviate with the *Secretin* family binding peptides and the *Adhesion* binding extracellular matrix molecules (2, 4, 7). The *Adhesion* GPCR family mediates the cytoskeletal organisation, thereby modulating the architecture of the cell. This facilitates the formation of dendrites in neurons as well as membrane shrinkage driving cellular rearrangements (for review see reference 43).

The *Glutamate* family consists of 22 members, composed of metabotropic glutamate receptors (GRM), gamma-aminobutyric acid receptors (GABAR), calcium-sensing receptor (CASR), sweet and umami taste receptors (TAS1R1-3). Most of these receptors bind glutamate in a mechanism likened to that of the Venus fly trap (VFTM), where glutamate binds in a cavity formed between 2 lobes in the extracellular N-terminal domain (9). The transmembrane domain of *Glutamate* family is generally well conserved, and contains analogous motifs and microswitches to those present in the *Rhodopsin* family (see section 1.3). Amongst these is WL motif in TM 6, which aligns with its counterpart CWxP$^{6.50}$, the PKxY aligns with NP$^{7.50}$xxY motif in TM 7 (2, 4) (superscript numbers refer to the Ballesteros and Weinstein residue numbering system (51)).

The *Frizzled/Taste2* GPCR family includes two distinct groups, the Frizzled and Taste receptors. The frizzled receptors mediate signals from the secreted glycoproteins termed Wnt, these receptors have a long 200 amino acid N-terminus which is thought to coordinate Wnt (2, 4). This family of receptors are predominantly involved in embryonic development, tissue and cell polarity (10). The function of these receptors in the Wnt signalling pathways is critical within the vertebrate central nervous system and has been implicated in the formation of neuronal circuits, such as synaptic assembly, dendritic development and axon pathfinding (11).

1.2 GPCR signalling pathways

Receptors are a physical conduit for the transmission of extracellular binding information across the cell membrane, triggering intracellular signal transduction cascades. The classical model for GPCR activation and signalling, in which it was suggested that GPCRs activate heterotrimeric G-proteins and that the receptors are down-regulated by β-arrestin, thereby stopping signal transduction, has been shown to be severely oversimplified (12). In the last decade, it has been shown that GPCR signalling is much more complex and sensitive than originally thought. For instance, it has been demonstrated that there is an array of G-protein independent signalling routes involving the effectors (β-arrestin, ubiquitin, etc; see below for more detail). With the inclusion of a more greyscale approach to GPCR signalling it has been shown that individual ligands are able to bias the signalling pathway taken by their receptor (13).

The activation of GPCRs thus triggers a diverse signal pattern along either G-protein-dependent or G-protein independent signalling routes. These individual signal patterns modulate a range of downstream proteins, dependent on their intracellular binding partner. They can inhibit or stimulate downstream processes including: adenylyl and guanylyl cyclases, phosphoinositide 3-kinase (PI3K), phospholipase A2 (PLA2), phospholipase C (PLC), phosphodiesterases and various ion channels. The modulation of these proteins leads to the production or inhibition of a plethora of secondary messengers; cyclic adenosine monophosphate (cAMP), cyclic guanosine monophosphate (cGMP), diacylglycerol (DAG), inositol (1,4,5)triphosphate (Ins(1,4,5)P3), phosphatidylinositol (3,4,5)triphosphate (PtdIns(3,4,5)P3), arachidonic acid and phosphatidic acid as well as the changes in intracellular concentration of ions such as Na^+, K^+ and Ca^{2+} (Figure 1-3).

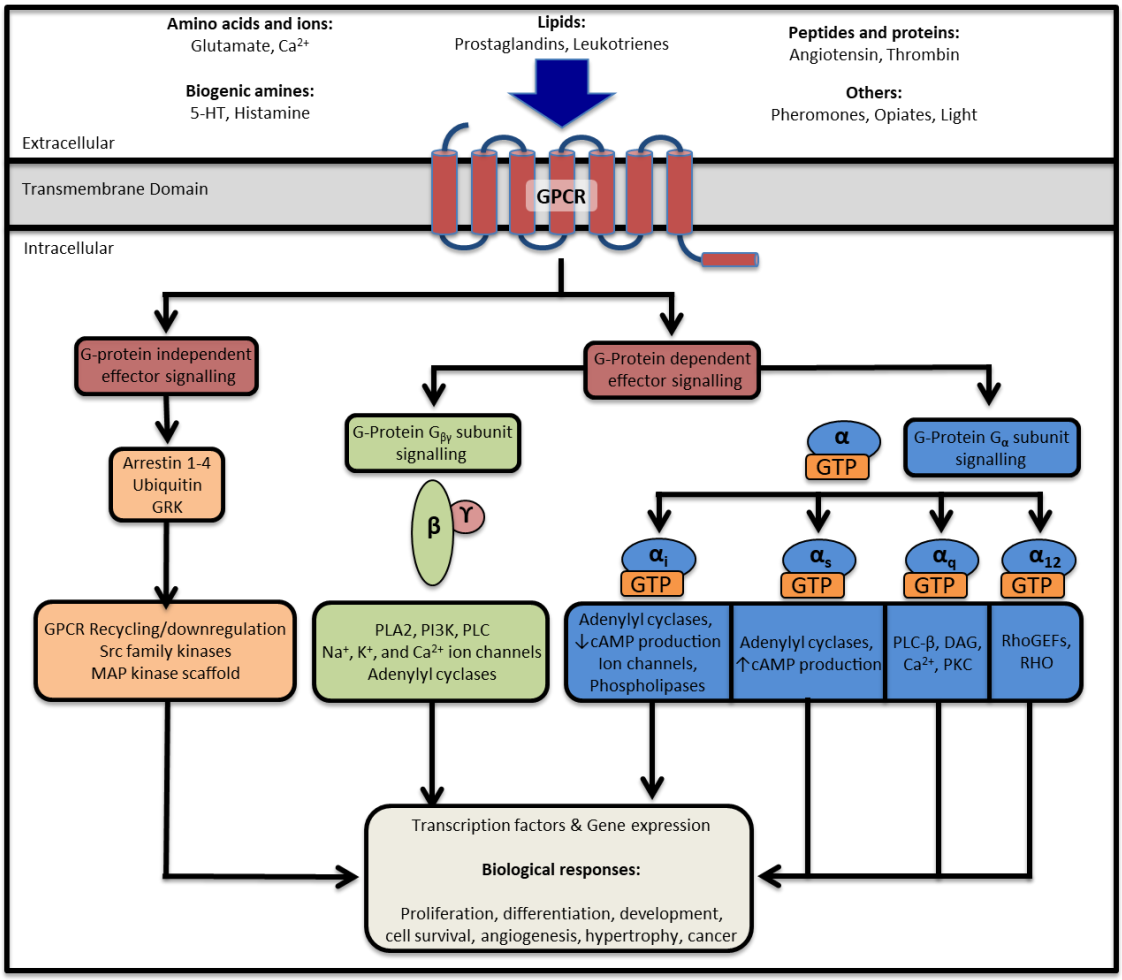

Figure 1-3: A schematic describing the downstream GPCR activation pathways

(Top) A vast range of ligands can bind to the extracellular domains of GRCRs, whereupon the GPCRs transmit this binding information across the membrane to the cytoplasm (only select examples shown). **(Bottom)** The GPCR can activate both G-protein dependent (green and blue) and independent (salmon) routes: The G-protein independent route can activate a range of kinases as well as regulating receptor turnover, while β-arrestin activation can also act as a scaffold for other signalling pathways. The activation of the G-protein trimer results in the dissociation of the Gα (blue) and Gβγ (green) subunits. Both the G-protein dependent and independent routes have significant impact upon the cells response (silver).

1.2.1 G-protein dependent signalling

The canonical signalling pathway of GPCRs occurs via the binding and activation of intracellular heterotrimeric G-proteins composed of Gα, Gβ and Gγ subunits. In its basal state, the GDP-bound Gα subunit is in complex with the dimer Gβγ and is localised to the plasma membrane where it can interact with the activated receptor. GPCRs act as a GTP-exchange factor (GEF) for the G-protein complex. This results in conformational changes, leading to the exchange of GDP-GTP in the bound Gα subunit Figure 1-4). Consequently the Gα and Gβγ subunits dissociate and can stimulate (e.g. $G\alpha_s$) and/or attenuate (e.g. $G\alpha_i$) their respective signalling pathways.

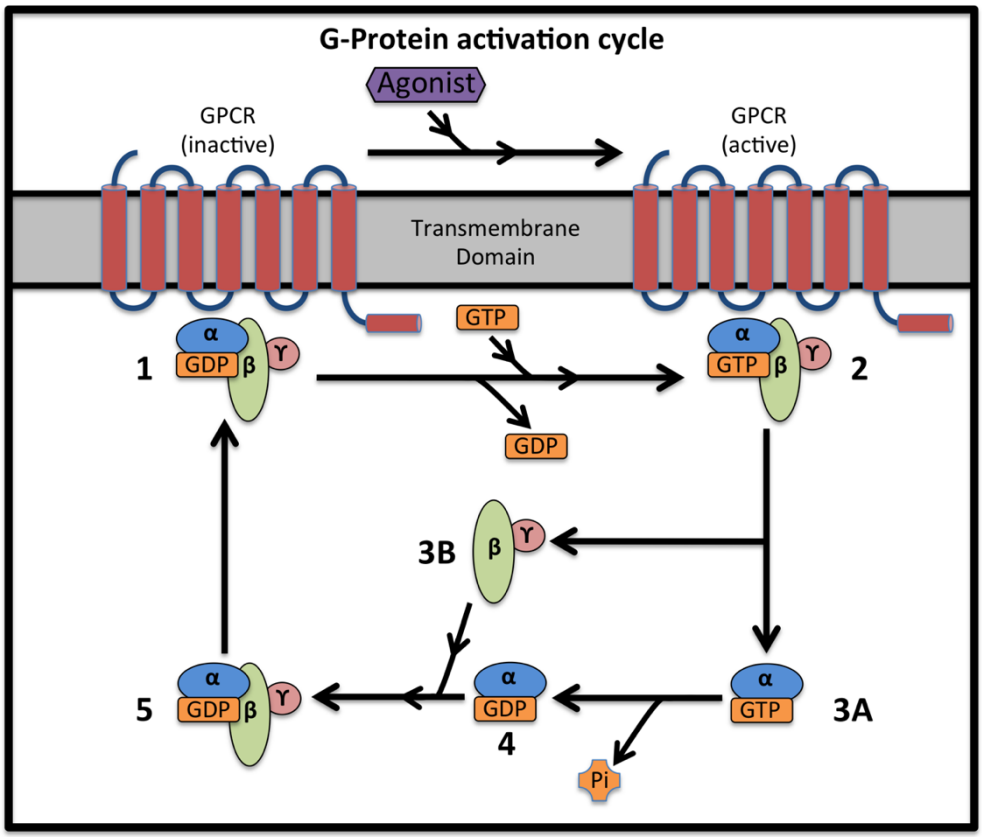

Figure 1-4: G-protein activation cycle

Schematic representation of the G-protein activation process by GPCRs (red cylinders) and subsequent inactivation. **(1)** The trimeric G-protein (Gαβγ-GDP) in a prebound form with an inactive GPCR. **(2)** Agonist binding to the GPCR allows the receptor to act as a guanine exchange factor (GEF) exchanging GDP with GTP. Only upon the activation of the downstream effectors is the receptor deemed truly active. **(3)** Upon GDP-GTP exchange, the G-protein dissociates to Gα-GTP **(3A)** and dimeric Gβγ **(3B).** Both of these signalling proteins subsequently activate their respective pathways (Figure 1-3). **(4)** The GTP bound to the Gα is catalysed into GDP, releasing the phosphate into the cytoplasm. This process marks the inactivation of the Gα subunit. **(5)** After the catalysis of GTP to GDP, the subunits Gα and Gβγ recombine to form the inactive Gαβγ-GDP. Subsequently they can either reform the prebound complex or associate with the receptor after agonist binding.

In humans, there are 21 Gα subunits encoded by 16 genes. The Gα subunits are separated into 4 classes: $G\alpha_s$, $G\alpha_i$, $G\alpha_q$ and $G\alpha_{12}$, dependent on their primary sequence similarity (14, 15). The $G\alpha_s$, $G\alpha_i$ are named after their ability to stimulate and inhibit, adenylyl cyclases, respectively. Whilst $G\alpha_q$ predominantly signals via phospholipase C (PLC) and $G\alpha_{12}$ activates Rho family of GTPases. The modulation of adenylyl cyclases by GPCRs regulates the concentration of the ubiquitous intracellular secondary messenger cAMP, involved in nearly every signalling cascade (see Figure 1-3 for more details).

The Gα subunit is composed of two domains: a 6-helix bundle unique to large Gα subunits, which forms a lid over the nucleotide-binding pocket burying the GDP within the core Gα, and a GTPase domain

conserved across all members of the G-protein superfamily. The GTPase domain hydrolyses GTP to GDP and provides a binding surface to the Gβγ dimer and the GPCR (16–18). An extended N-terminal α-helix can be covalently modified with fatty acids. Myristoylation is an irreversible covalent modification necessary for membrane attachment, whilst palmitoylation is reversible and may have a role in the receptor bias between different G-proteins (19). The tip of the C-terminal α-helix coordinates with the active state GPCR within the core the transmembrane helices on the intracellular side (20).

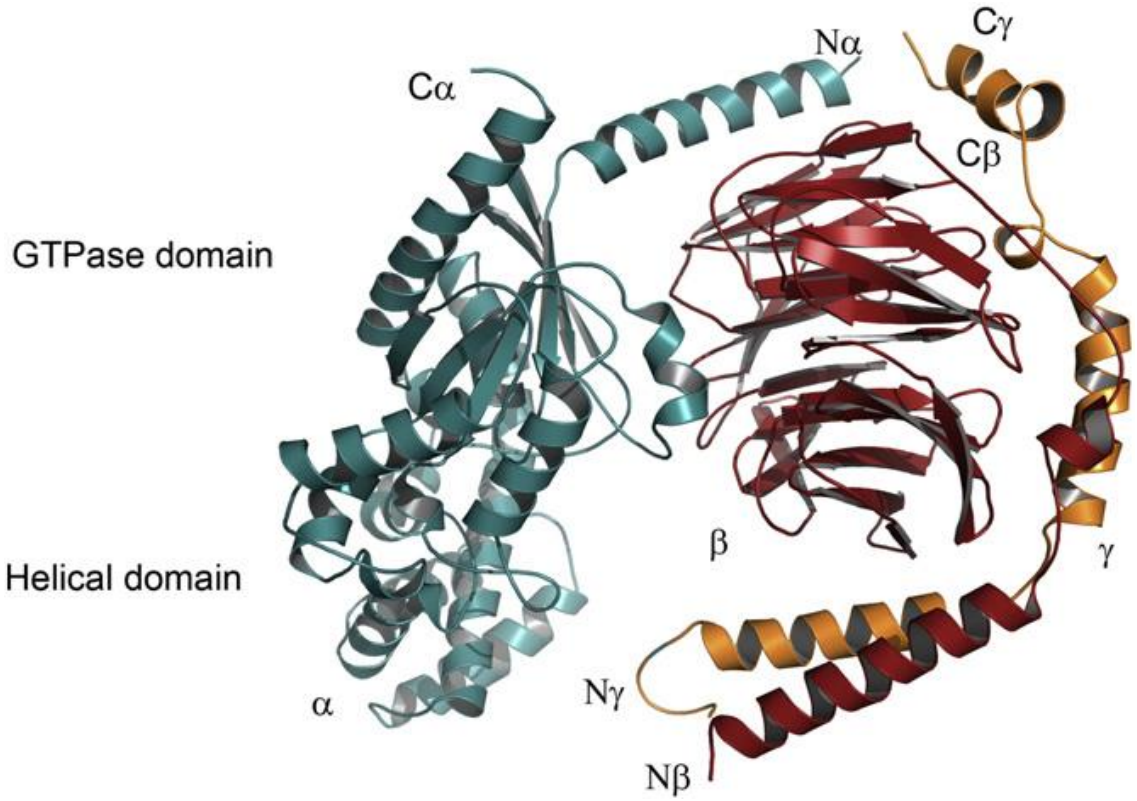

Figure 1-5: Structural representation of a trimeric G-protein

The typical structure of a G-protein as exemplified by transducin. The Gα, Gβ and Gγ subunits are coloured in cyan, red and orange respectively. Figure adapted from (21)

The process of GDP-GTP exchange in the Gα subunit upon activation by activated GPCRs is still very poorly understood. However, it is known that following the nucleotide exchange of GDP with GTP the γ-phosphoryl group of the newly bound GTP results in a conformational rearrangement. The structural rearrangements occur within 3 switch regions, which are critical for the protein-protein interactions between Gα and its nucleotide state specific binding partners Gβγ (16–18).

Gβ consists of an N-terminal α-helix and a β-propeller composed of 7 segments of WD-40 repeats. In contrast to the Gβ subunit, the Gγ protein is very small. The N-terminus forms a coiled coil interaction with the N-terminus of the Gβ subunit, whilst the remainder of the Gγ subunit coordinates with the outer edge of the Gβ toroid (22). The Gγ subunit is prenylated post-translationally at the C-terminus, receiving either a 20-carbon geranylgeranyl group or a 15-carbon farneryl group facilitating the membrane localisation of the Gβγ dimer (23).

Originally, the Gβγ subunit was thought to be involved in the inactivation of the Gα subunit, thereby acting as a negative regulator of Gα signalling (24). However, the Gβγ subunit has been shown to interact with many effector proteins including some, which are also modulated by the Gα subunits. With five Gβ and twelve Gγ proteins within humans, most Gβ and Gγ subunits can form dimers, the combination specificity between Gβ and Gγ subunits could contribute to the selectivity needed to generate the wide range of G-protein signalling fingerprint. For example, $G\beta_1\gamma_1$ support binding of $G\alpha_t$ to rhodopsin whereas $G\beta_1\gamma_2$ does not (for review see reference 59).

Whilst the activation process of G-proteins by their GPCR is currently unknown, recent crystal structures have revealed the possible binding modes of the G-protein and GPCR. In recent years, two mechanisms of interaction between the G-protein and GPCR have been proposed: the collision coupled model and the precoupled complex model. The collision-coupled model was originally proposed by Tolkovsky and Levitzki (26). Here, GPCRs and G-proteins interact by collision, whilst freely diffusing laterally on the plasma membrane. In this model only activated agonist bound GPCRs can couple to and activate their downstream processes. In contrast, the precoupled model proposes that the GPCR and G-protein exist in a prebound state before agonist binding (27). The physiological significance of this complex is entirely dependent on the rate-limiting steps of the downstream processes, as preassembly of the complex will have little effect on the inhibition of cAMP production (slow), while it will have a significant effect on the activation of ion channels in excitable tissue (fast). However it is becoming clear that a combination of the two occurs, which is highly dependent on the GPCR and G-protein subtype (28).

1.2.2 G-protein independent signalling

GPCRs are modulated by a multitude of mechanisms such as internalisation, desensitisation and interactions with cytosolic proteins. The aforementioned mechanisms are often mediated via posttranslational modifications (eg. glycosylation, palmitoylation, phosphorylation and ubiquitination), which in turn activate G-protein independent pathways, predominantly mediated by a small family of arrestins (Figure 1-6). However, it has been shown that ubiquitination has a far wider role in GPCR signaling than purely targeting activated receptors for lysosomal degradation.

Arrestins are a family of four intracellular proteins (arrestin 1-4). Arrestin 1 and 4 are exclusively expressed within the visual rhodopsin system, in contrast, arrestin 2 and 3 are ubiquitously expressed and have since been renamed β-arrestin 1 and 2, respectively (29). The binding of arrestin 1 and 4 to GPCRs desensitises GPCR signalling, however only the binding of β-arrestin 1 and 2 results in the internatisation of the GPCR (30, 31). During the β-arrestin mediated internalisation of GPCRs, β-arrestins act as adaptor proteins for scaffold trafficking proteins clathrin, N-ethylmaleimide-sensitive fusion protein (NSF) and AP-2 (for review see reference 66).

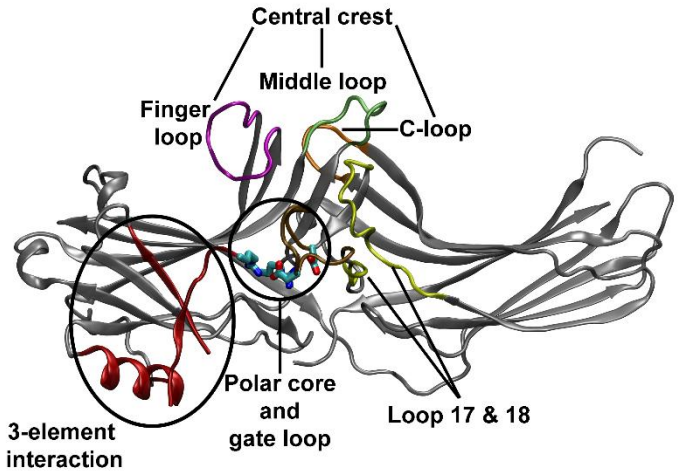

Figure 1-6: Structural representation of β-arrestin
The typical structure of a β-arrestin as exemplified by bovine β-arrestin 1 (33). Domains important for the binding to GPCRs (central crest) and activation (polar core and 3 element interaction) are highlighted.

Ubiquitin is a 76 amino acid protein that is covalently attached to surface-exposed lysine residues. Three types of enzymes regulate the attachment of ubiquitin to its substrate: ubiquitin activating enzyme (E1), ubiquitin conjugating enzyme (E2) and ubiquitin ligase (E3). There are 2 major pathways involving the degradation of GPCRs: endosomal-sorting complex required for transport (ESCRT) pathway to lysosomal degradation and the ubiquitin proteasome system (UPS). GPCRs, which undergo agonist-induced ubiquitination, are predominantly internalised and are tagged for degradation, however once within the endosome they can be deubiquitination and redirected back to the plasma membrane (for review see reference 68).

1.2.3 Biased signalling

As described above, GPCRs are able to trigger a range of signalling pathways. However the specific subset of signalling pathways activated, is governed by individual ligands, an effect termed biased agonism (Figure 1-7). A balanced ligand would equally activate both the G-protein dependent and independent signaling pathways, whilst a biased ligand would activate one pathway preferentially over the other. Therefore, different ligands can have disparate efficacies ("pluridimensional efficacy"), and consequently drug efficacy cannot be measured in only terms of affinity and response magnitude, but the specific array of signals elicited from the receptor.

The simple concept of agonist, antagonist and inverse agonist within the GPCR research field, has therefore led to the unexpected behaviour of some antagonists in the pharmaceutical industry. The introduction of biased agonism could explain distinct outcomes in patients treated with different antagonists for the same receptor. For example, Carvedilol, a common drug used in heart failure, is a G-protein antagonist. However it is also a β-arrestin and ERK biased agonist. In this case, it improves the therapeutic action of the drug

(35, 36). In contrast, Famotidine, an inverse agonist for the $G\alpha_s$ signalling pathway, also acts as a G-protein independent agonist, leading to the up regulation of histidine carboxylase and deleterious side effects after withdrawal (37).

In recent years, a third signal class has been added to the G-protein dependent and independent signal patterns. It was originally thought that GPCR signalling occurs at the plasma membrane and was quickly terminated by receptor internalisation caused by β-arrestin binding, however the internalisation of some GPCRs after activation does not terminate their signalling processes. Instead, they have been shown to continue to signal via the Gα pathway from the endosome (38–42). Therefore, signalling via endosomal G-proteins can be classified as new type of bias, as the signalling is temporally and spatially distinct from the canonical signalling present at the plasma membrane. As with the classical GPCR bias, different ligands have differential effects on the same receptor. However in this case, the ligands change the duration and location of the same signal pathway, thereby altering the distribution of secondary messengers with the cell (43). For example, parathyroid hormone (PTH) and PTH-related-Peptide (PTHrP) both modulate the PTH receptor, however, the dynamics of activation are vastly different, with only PTH inducing a sustained cAMP production via the early endosome, after a short exposure to the ligand (39).

As previously mentioned, ligands are able to stabilise biased conformations. Interestingly, however ligand affinities are also allosterically modulated by the binding of β-arrestin and G-proteins (44). Therefore, it is important to note that the available subset of binding partners varies greatly across cell types as well as within the same cell under different conditions (45). Consequently, even if the same genetically encoded receptor was expressed in different cells and exposed to the same ligand, the biased responses might not be conserved across cells types and would display differential binding and/or signalling patterns.

The mechanisms involved in biased signalling are to date unknown. Therefore, it is notoriously difficult to design ligands with a specific signal pattern (46, 47). Of particular note, opioid signalling is an excellent cultural, physiological and pharmacological example of the effects of biased signalling. In the case of μ-OR signalling, β-arrestin 2 activation causes undesired side effects such as gastrointestinal dysfunction, respiratory depression and tolerance, whereas G-protein activation displays analgesic efficacy. The first clinical trial of the biased agonist TRV130, selective for the G-protein pathway binding to the μ-OR, produced analgesia in comparable levels to morphine whilst mitigating the unwanted side effects (48).

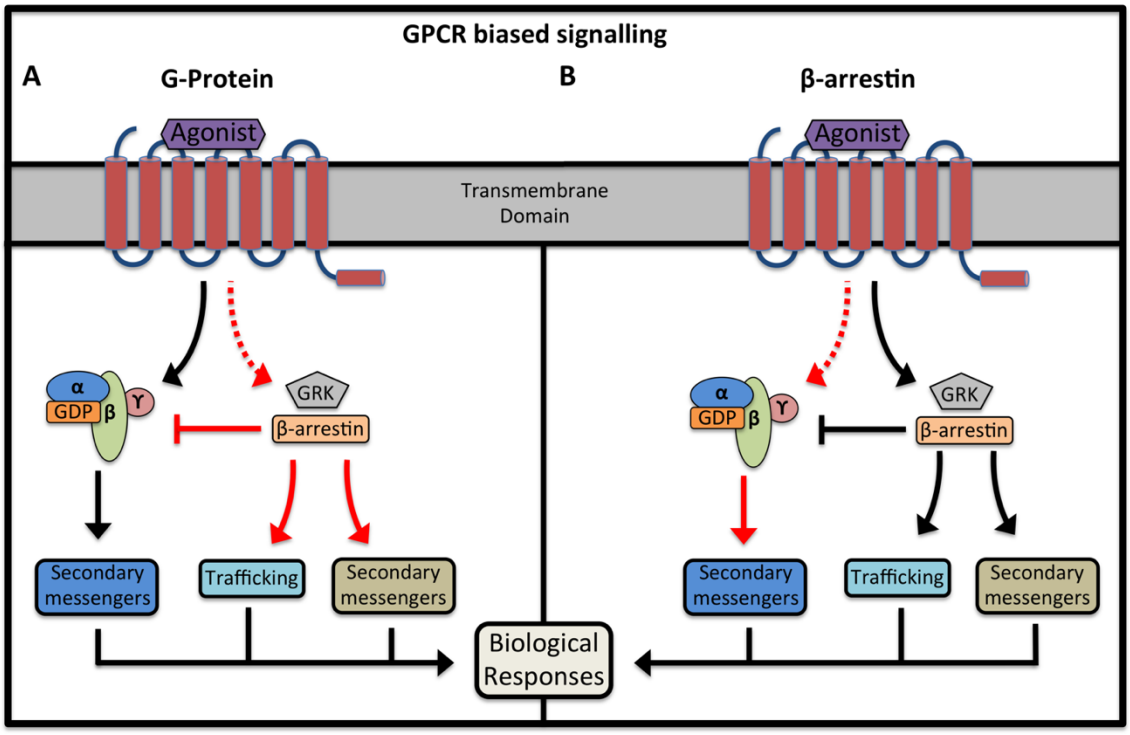

Figure 1-7: A schematic representation of biased signalling

(A) A G-protein biased ligand is shown which predominantly activates the G-protein dependent pathway controlling secondary messengers shown in dark blue. **(B)** A G-protein independent biased ligand, where the β-arrestin pathway is predominantly activated. This leads to receptor internalisation, receptor trafficking (light blue) and the activation of a different set of secondary messengers (tan).

1.3 Rhodopsin receptor family/class A structure

As previously mentioned, GPCRs are composed of seven transmembrane helices and a horizontal helix, connected by either intra or extracellular loops. GPCRs are composed of three domains: The extracellular domain, consisting of the N-terminus and three extracellular loops (ECL 1-3); the transmembrane domain, consisting of the seven α-helices; and the intracellular domain, consisting of the intracellular loops (ICL 1-3), an amphipathic helix (H8) and the C-terminus (Figure 1-8).

In the *Rhodopsin* family, the extracellular region regulates access of ligands to the core of the receptor. The transmembrane domain forms the structural core of the receptor, binding the ligand, and transmitting the signal through the membrane to the cytosol. Whilst the intracellular domain coordinates the binding of cytosolic effector proteins with the receptor, thereby helping to mediate the signalling specificity of the receptor.

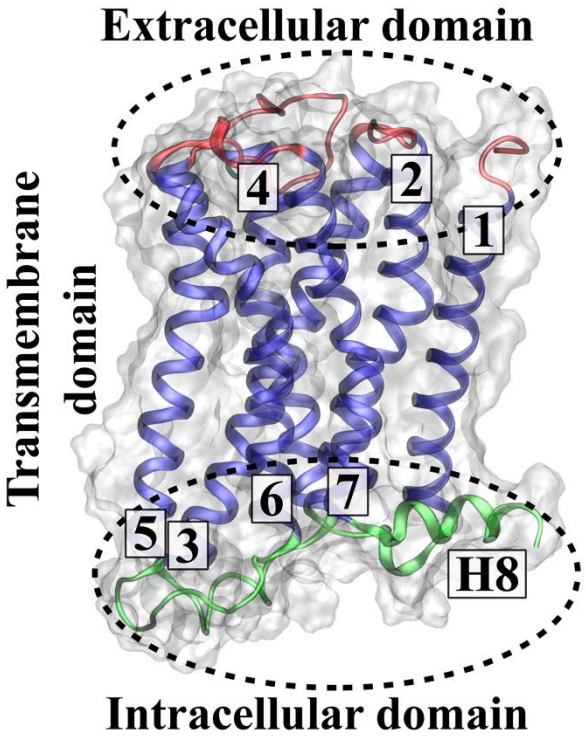

Figure 1-8: The three domains in the *Rhodopsin* GPCR family

Shown here are the three domains within the Rhodopsin GPCR family as exemplified by the M2R. The extracellular domain is highlighted in pink, the transmembrane domain is shown as blue helices and the intracellular domain is highlighted in green.

1.3.1 Extracellular region

The *Rhodopsin* family of receptors shows two distinct types of extracellular region. In most receptors the ligand binding pocket is accessible to the bulk solvent, whilst in others the ligand binding pocket is occluded such as in the rhodopsin, $S1P_1$ and FFAR1 receptors. This has been proposed to be due to the access of ligand to the receptor from the lipid bilayer in these receptors (49). Of the three ECLs, ECL 1 and 3 are unremarkable short loops lacking any obvious structural features. In contrast, for receptors that bind water-soluble ligands, the ECL 2 loop differs structurally throughout the family, though it is conserved in a subfamily specific manner. The secondary structure of the ECL 2 can contain helices (adenosine receptors), sheets (peptide-binding receptors) or can be disordered (muscarinic receptors). In all cases the ECL 2 partially folds over the extracellular region, shaping the ligand entry pathway into the binding pocket within the transmembrane domain. The conformational flexibility of the ECL 2 is delineated by a conserved disulphide bridge, between residue $C^{3.25}$ in the TM domain and ECL 2, which anchors the loop and thereby decreases its flexibility. In certain subfamilies, additional intra-loop disulphide bridges provide further structural stability and limit its conformational freedom (for review see reference 48).

1.3.2 Transmembrane Domain

The helical bundle within the transmembrane domain acts as a physical conduit for the signal between the ligand binding site and cytosolic binding partners. An analysis of available GPCR structures has revealed a consensus network of 24 inter-helix contacts mediated by 36 topologically equivalent amino acids (Figure 1-9). These contain the highly conserved residues: $N^{1.50}$, $D^{2.50}$, $W^{4.50}$ and $P^{7.50}$. However, in some positions, there is a high tolerance to amino acid variation, while predominantly similar non-bonded interactions between residues are retained. For example, the contacts between residue 2.42 and 3.46 are seen in all GPCR structures, while the sequence is highly variable. For instance, in bovine rhodopsin, they are isoleucine and leucine, whilst in κ-OR they are tyrosine and methionine, respectively. This consensus network is thought to provide an evolutionary structural scaffold of non-covalent contacts (for review see reference 15). The positioning of the inter-helical contacts is predominantly within the central TM domain and towards the cytoplasmic face of the receptor, primarily clustered between the helices 1-2-7, 2-3, 3-4, 3-5-6. It has been proposed that TM3 provides a structural hub for the transmembrane region (Figure 1-9).

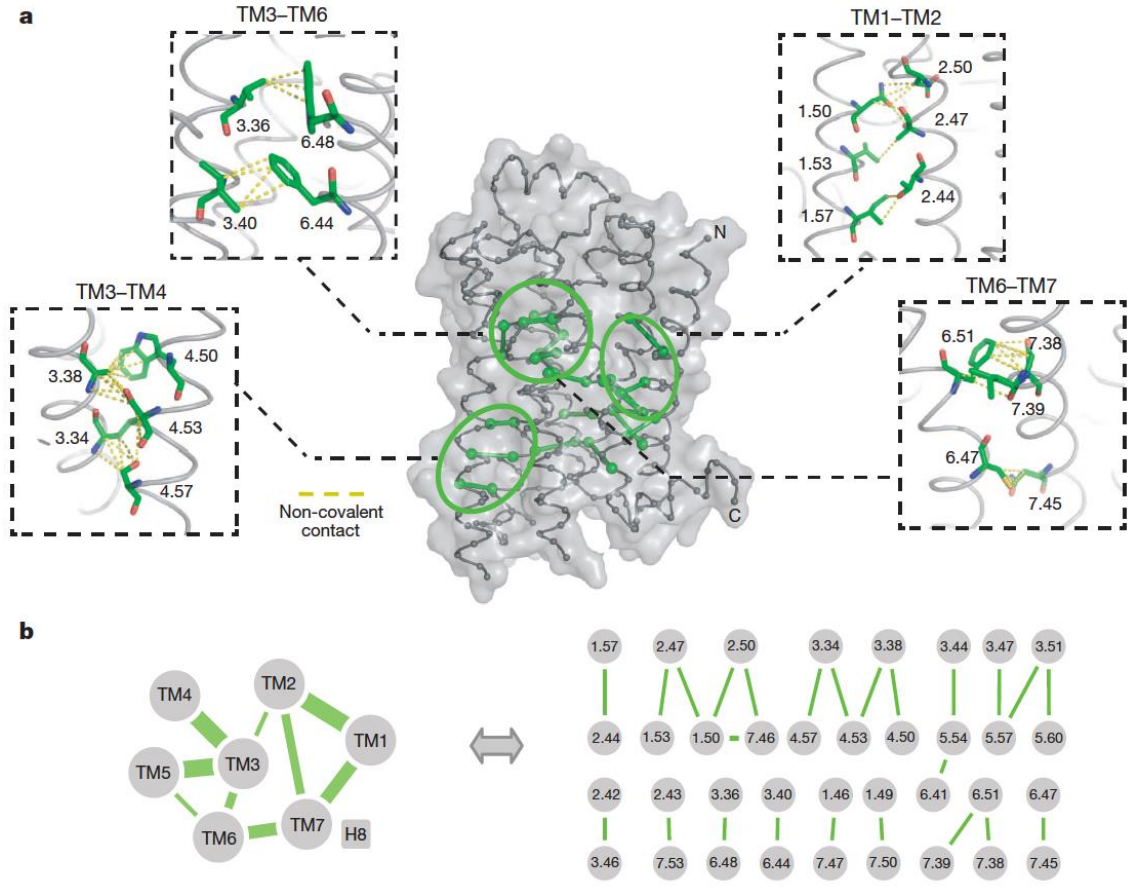

Figure 1-9: Consensus scaffold non-covalent contacts within the *Rhodopsin* GPCR family

(A) A network of 24 inter-helical contacts between 36 topologically equivalent residues exists in GPCRs as exemplified by the inactive β_1AR. **(B)** Schematic depicting the inter-TM contact network. The thickness of the lines denotes the number of contacts between the TM helices. Figure adapted from (52).

A remarkable feature of the *Rhodopsin* family is the ability to coordinate highly diverse ligands, differing in chemical properties, shape and size. Throughout the *Rhodopsin* family, ligands bind in the extracellular portion of the transmembrane region, within a large hydrophilic pocket extending halfway through the receptor. In most receptors, the ligand-binding site is formed by a scaffold of the residues at 3.32, 3.33, 3.36, 6.48, 6.51, 6.52 and 7.39 (Figure 1-10)(53).

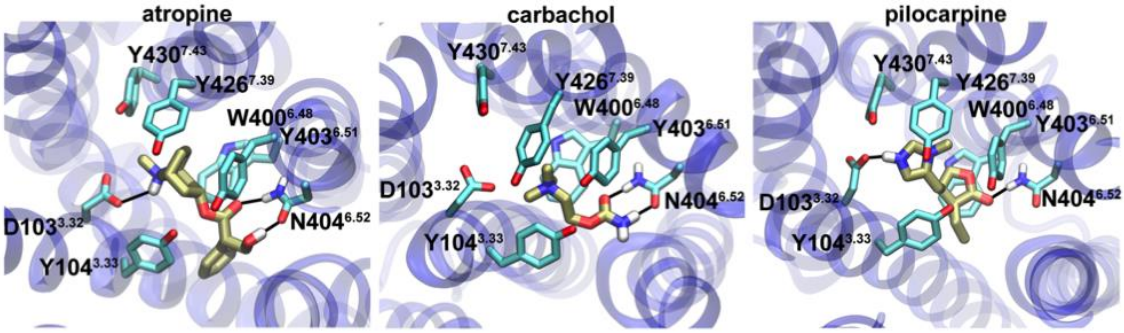

Figure 1-10: Ligand binding site within the m2 muscarinic receptor

Three ligands bound within the M2R orthosteric ligand-binding site are shown. The ligands are bound within a cage of tyrosine residues. The two key ligand-binding residues within the m2 muscarinic receptor are $D103^{3.32}$ and $N404^{6.52}$. The receptor is shown in a top down view and hydrogen bonds between the ligand and receptor are depicted as black bars.

1.3.3 Intracellular domain

As discussed in section 1.2, GPCRs can bind a vast repertoire of intracellular binding partners such as G-proteins, G-protein Receptor Kinases (GRKs) and arrestins. The intracellular section of the receptors is composed of three intracellular loops and a C-terminal tail. In some receptors such as the δ-OR, ICL 2 can contain an arginine, which forms a salt bridge with $D^{3.49}$ at the end of TM3 anchoring the loop and therefore reducing the loop's flexibility. In contrast to ICL 1 and 2, ICL 3 is disordered with no secondary structure. Finally, the C-terminal region is composed of an amphipathic helix (H8), typically 3 turns in length and a disordered section. The disordered section has been implicated in the pre-coupling of G-proteins, binding of arrestins and as a target for a variety of post-translational modifications (phosphorylation, ubiquitination, etc).

1.3.4 GPCR domain evolution

Of interest, there has been increasing evidence of a "bar code" present in the intracellular domain, in which each G-protein recognises a specific sequence of residues on the receptor (54). In contrast to the previous theory, it has perhaps unsurprisingly come to light, that G-protein binding is far more dynamic than previously thought. GPCR repertoires are thought to have been generated via gene duplication from an

ancestral receptor. Upon gene duplication, both GPCR copies are identical. However, over time these identical copies diverge, by accumulating mutations, in two predominant ways: (1) altering G-protein selectivity whilst maintaining ligand-binding properties (e.g. adrenoceptors; Figure 1-11, green bar), (2) altering their ligand-binding properties but retaining G-protein selectivity (e.g. olfactory receptors; Figure 1-11, blue bar). In subsequent duplication events and further divergence, the receptors accumulate mutations allowing for different or additional G-protein and/or ligand binding (e.g. aminergic or opioid receptors) (55).

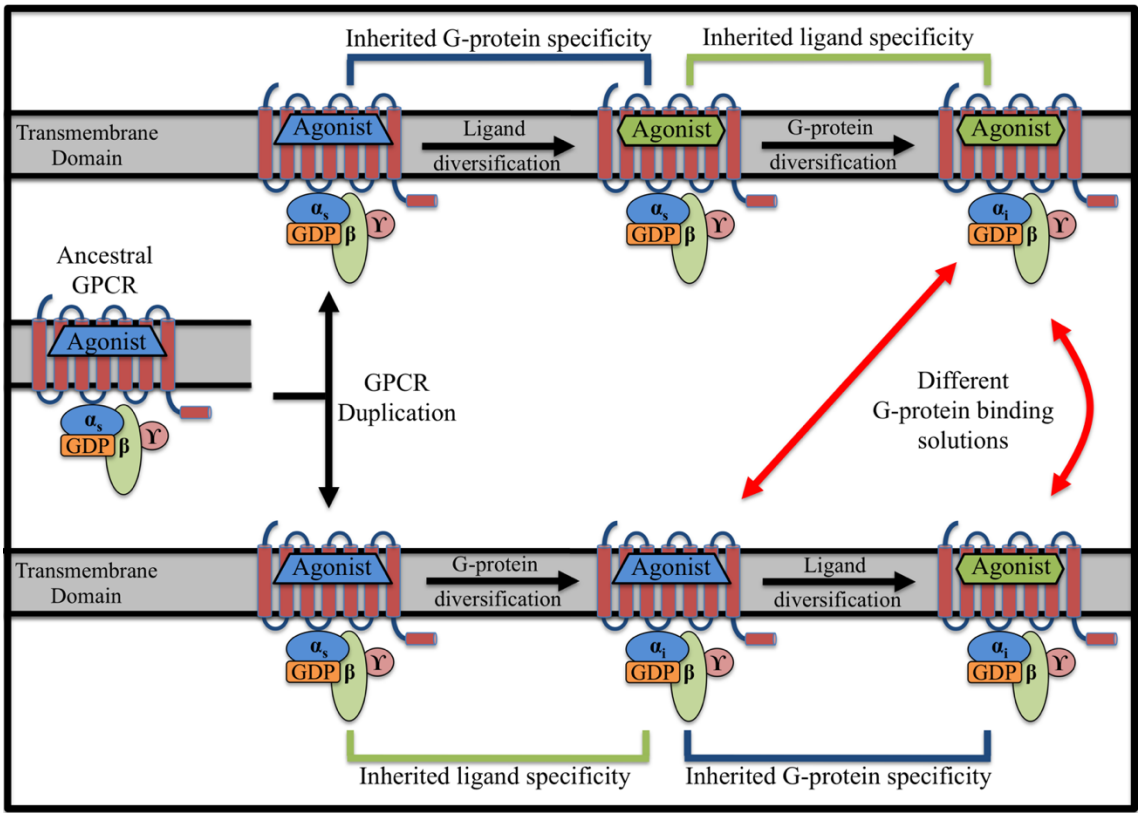

Figure 1-11: A schematic depiction of the domain evolution of GPCRs

Starting from an ancestral GPCR on the left, a gene duplication occurs, giving rise to two identical copies. Each copy accumulates different mutations modulating ligand specificity (green bars) and/or the G-protein specificity. After subsequent mutations the receptors might still couple to the same G-protein except have different binding characteristics. Adapted from (55).

1.4 Rhodopsin receptor family/class A microswitches and motifs

It is believed that there is a common activation mechanism within the *Rhodopsin* GPCR family (56, 57). Biochemical and crystallographic analysis of inactive and active states have been combined into a unified activation model termed “global toggle switch”. In this model activation the receptor undergoes a vertical see-saw movement pivoted around the Na^+ binding pocket (section 1.4.2) during activation (58). The

extracellular portion (TM 6 and 7) of the receptor is thought to tilt inwards towards the orthosteric ligand binding site , whilst the intracellular portion (TM 6 and 7) tilts outwards opening a binding site for the intracellular effector (Figure 1-14). There have been many structural motifs and so-called "molecular switches" that alternate between substantially different conformations in the inactive and active states, these are proposed to be integral components of the activation mechanism.

Here I describe the four most conserved: (1) Toggle switch – C/S/TWxP$^{6.50}$, (2) Transmission switch – P$^{5.50}$I/V$^{3.40}$F$^{6.44}$, (3) D(E)R$^{3.50}$Y motif, (4) NP$^{7.50}$xxY motif. The aforementioned motifs have all been implicated in receptor activation, however as yet, no consensus within the GPCR community exists as to the precise number or functional role of these motifs (Figure 1-12).

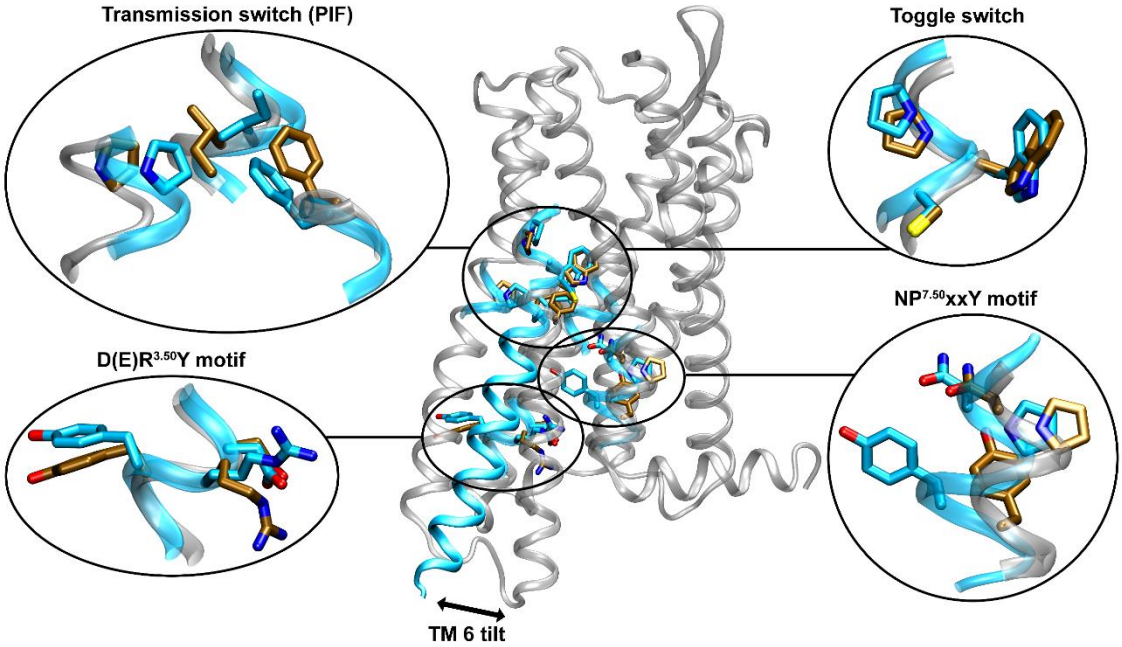

Figure 1-12: Location of microswitches implicated in activation

Depicted here are the four main microswitches conserved across the Rhodopsin GPCR family as exemplified by the M2R. The active conformation of the microswitches are shown in blue whilst the inactive are shown in orchre. In order of sequence, the toggle switch and transmission switch link the ligand-binding site to the Na^+ binding site (see section 1.4.2). Below the Na^+ binding site in the intracellular portion of the receptor are the NP$^{7.50}$xxY and D(E)R$^{3.50}$Y motifs. Also highlighted is the conformation change of TM 6 from the inactive (silver) to the active (blue).

1.4.1 Toggle switch (C(S/T)WxP$^{6.50}$) and transmission switch (P$^{5.50}$I(V)$^{3.40}$F$^{6.44}$)

Within all crystal structures of the active *Rhodopsin* family receptors, several conserved residues are observed to change conformation in a concerted manner. The transmission and toggle switch link the ligand-binding site with the movement of TM 5 & 6 through a rearrangement of the interface between TM 3-5-6. The original data and hypothesis originates from work on rhodopsin and β_2A receptors, describing the movements of F$^{6.44}$ towards P$^{5.50}$, I(V)$^{3.40}$ away from P$^{5.50}$, and the rotation of W$^{6.48}$. The toggle switch was originally proposed to alternate between two rotamer states (59, 60), however, the rotameric state and function of the residue has since been shown to be likely dependent upon the receptor and ligands studied (61–63).

1.4.2 Na$^+$ binding pocket

The recently solved crystal structures of the A_{2A} adenosine receptor, β_1 adrenergic receptor, protease-activated receptor and δ-Opioid receptor reveal a Na^+/water cluster within the core of transmembrane bundle (Figure 1-14)(64–67). Crucially, these structures represent three of the four major branches (α, δ and γ) in the Rhodopsin GPCR family (see section 1.1.1). Interestingly, this pocket is highly conserved, both conformationally and chemically with a reported all atom RMSD of 0.8 Å, whilst the Na^+ ion and surrounding waters shows an RMSD of 0.5 Å between the A_{2A}AR (PDB: 4EIY) and β_1AR (PDB: 4BVN)(68).

The δ-OR (γ-branch) shows a distinct variation in the Na^+ binding pocket when compared to the previously mentioned structures. Whilst 15 of the conserved pocket residues are similar to the A_{2A}AR and β_1AR, the position 3.35 is the least conserved (Figure 1-13). In roughly 33% of receptors position 3.35 contains an asparagine, whereas in the majority of receptors within the *Rhodopsin* GPCR family, this position is occupied by a hydrophobic residue. Mutations of this residue dramatically alters the signalling of GPCRs in a receptor specific manner, for example within the δ-OR receptor the mutation of N$^{3.35}$ results in a constitutively active β-arrestin biased receptor (65, 68).

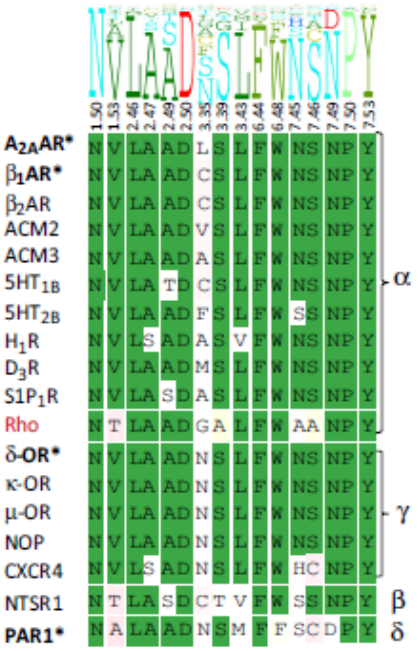

Figure 1-13: Sequence conservation of the Na^+ binding pocket

(**Top**) shows the residue conservation in all non-olfactory Rhodopsin GPCRs, where the height of the residue letter corresponds to the frequency of the residue at this position. (**Bottom**) Individual residues are shown for some Rhodopsin GPCRs structures, conserved residues are highlighted in green. Greek letters on the right denote the 4 major branches of Rhodopsin GPCRs (section 1.1.1). Receptors in which Na^+ binding has been determined by crystallography are in bold and marked with a '*'. The rhodopsin receptor which lacks the Na^+ binding site is highlighted in red. Figure adapted from (68).

These structures also provided a detailed description of the Na^+ binding site within the *Rhodopsin* GPCR family. The ion is predominantly coordinated by the sidechain of $D^{2.50}$ with four additional polar interactions with the receptor side chains ($S^{3.39}$, $N^{7.45}$) or water molecules. Interestingly, a retrospective analysis of previous inactive crystal structures strongly suggests that the electron density, previously modelled as water is compatible as a Na^+ ion in many cases.

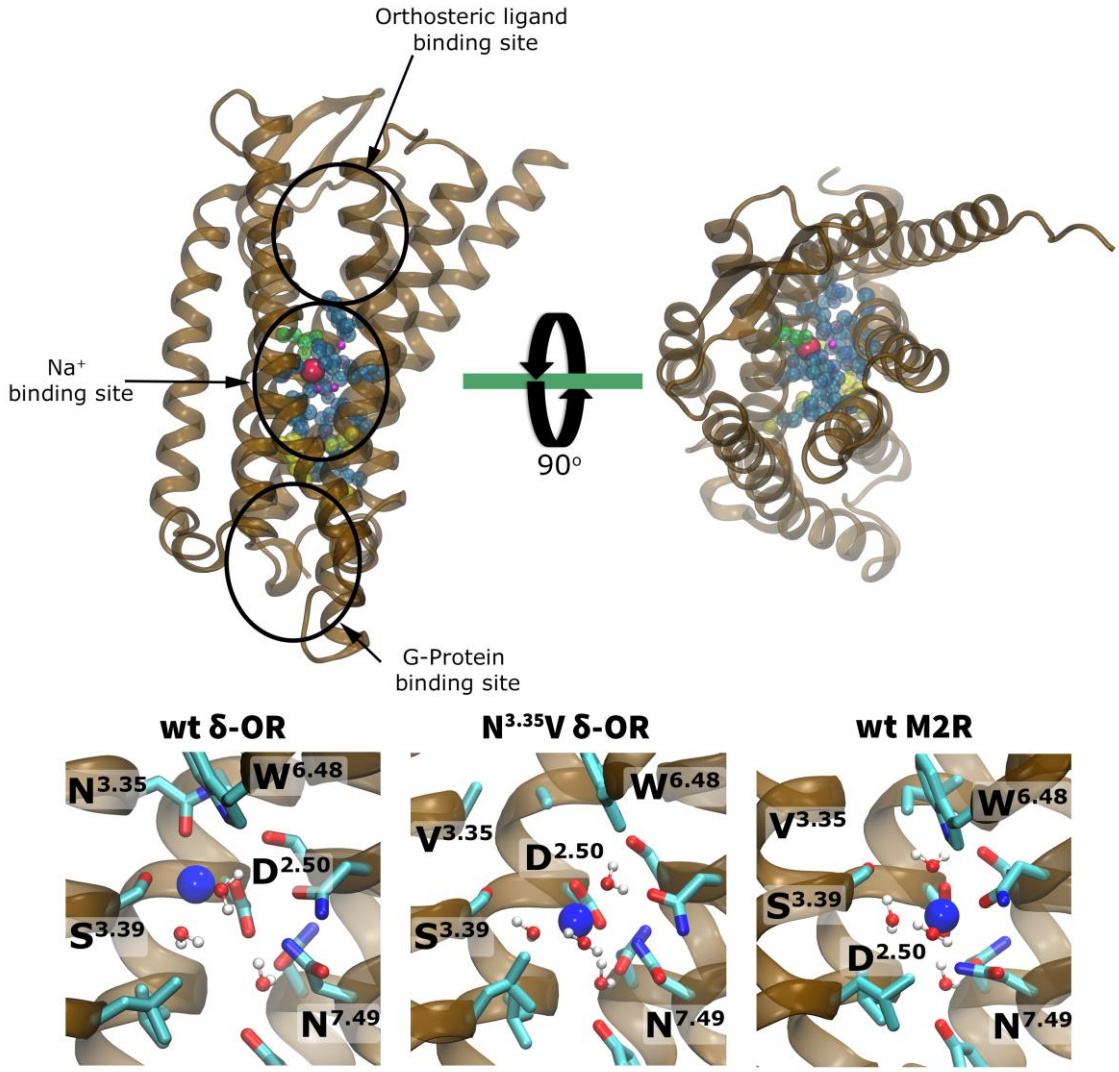

Figure 1-14: Conserved residues forming the internal hydrophilic pocket of Rhodopsin family of GPCRS

(Top) Sixteen conserved residues (blue/red spheres) line the hydrophilic pocket in GPCRs (68). The pocket connects the orthosteric ligand-binding site and the G-protein binding site (black eclipses). The pocket is accessible from the extracellular side but separated from the intracellular side by a hydrophobic layer (yellow spheres) (69). Fifteen of the 16 residues are highly conserved (blue); the less conserved position 3.35 is shown in green. At the allosteric binding site for Na^+, water molecules are depicted as purple spheres (water oxygen atoms), and the Na^+ ion is shown in red. The receptor is shown in side view on the left; the right panel displays a top view from the extracellular side. **(Bottom)** Close-up views of the binding site for Na^+ (blue sphere) within the hydrophilic pocket of the wt δ-OR, $N131^{3.35}V$ δ-OR, and the wt M2R, as observed in our simulations. The binding site for Na^+ in the M2R was inferred from the position and interactions of the ion in the wt δ-OR and the conservation level of the Na^+ binding residues. Figure adapted from (70).

In the protease-activated receptor 1 (Par1), the Na^+ ion is predominantly coordinated by $D^{2.50}$ and $N^{7.49}$, though interestingly 7% of the *Rhodopsin* GPCR family have an aspartate at both 2.50 and 7.49. Many δ-

branch GPCRs and most of the large olfactory receptors family (>380 receptors) contain a second acidic residue at position 3.39. Only 36 *Rhodopsin* GPCRs do not contain an aspartate at position 2.50 and of these 26 are described as non-signalling, decoy, putative, orphan or a pseudogene as described by the International Union of Pharmacology (IUPHAR) or UniProt databases. Interestingly, the receptors which do not contain an acidic residue at position 2.50, it is alternatively positioned at 3.39, 7.49 or 7.50. For example, the receptor GnRHR has an asparagine in position 2.50 and an aspartate at position 7.49. It has been shown that this receptor is still allosterically modulated by Na^+ ions (see section 1.5.3), supporting the hypothesis that alternate acidic residues within the Na^+ binding pocket are still able to coordinate Na^+ (71).

Upon GPCR activation, the Na^+ binding pocket collapses from 200 to < 70 $Å^3$ due to the inward movement of TM 7 and outward movement of TM 6 (68). These observations suggest that the activated *Rhodopsin* GPCRs are incompatible with Na^+ binding. Therefore, although it has been shown by crystallography that the activation of the receptor abolishes Na^+ binding, the question remains as to what happens to the Na^+ ion upon activation and how it leaves the receptor.

Studies into the Na^+ binding pocket have shown that small mutations can lead to a pronounced signal bias. The point mutations $D^{2.50}A$, $N^{7.49}A$, $N^{7.45}A$ transform the classical δ-OR antagonist naltrindole into a β-arrestin biased agonist (65). Furthermore, mutations of $N^{3.35}$ to Valine or Alanine reduce and abolish Na^+ binding, respectively. However, these point mutations create a constitutively active β-arrestin biased receptor, which cannot be modulated by ligand binding (65). These mutation studies on the δ-OR receptor provide support to the idea that the Na^+ binding pocket has a strong role in regulating signal bias.

1.4.3 $NP^{7.50}xxY$ motif

The $NP^{7.50}xxY$ motif is located at the intracellular side of TM 7, bridging the hydrophobic layer which separates the Na^+ ion-binding pocket and the transmission switches from the intracellular effector-binding site and the $D(E)R^{3.50}Y$ motif (see section 1.4.4). The residue $N^{7.49}$ is highly conserved, however in some cases it can be replaced with an acidic residue such as in the GnRHR, in which the residues occupying positions 2.50 and 7.49 are switched (71). The $Y^{7.53}$ is another highly conserved residue within this motif, and one of the major micro-switches for activation. In the inactive receptor conformation, the $Y^{7.53}$ sidechain is in an upward orientation bridging the hydrophobic layer and coordinates with the sidechains of $N^{1.50}$ and $D^{2.50}$ via a water molecule (Figure 1-12). Upon receptor activation, the sidechain of $Y^{7.53}$ changes its rotamer conformation from a vertical to a horizontal (65, 72) or downward (73) state interacting with TM 3, 5 and 6 (65, 72, 74). This causes a rearrangement of the hydrogen bond network extending from the ligand binding site through the core of the receptor to the $D(E)R^{3.50}Y$ motif and effector binding site. Though not classified as part of the $NP^{7.50}xxY$ motif, the side chain of the highly conserved $Y^{7.58}$ forms a water mediated hydrogen bond with $Y^{7.53}$ when it resides in the horizontal conformation. Interestingly, this residue is located towards the intracellular section of TM V and has itself been crystallised in two conformations: either the sidechain faces outwards into the lipid head groups or inward towards the

$NP^{7.50}xxY$ motif. Both inward and outward conformations have been seen within inactive and active crystal structures (65, 72), leading to a lack of consensus as to the role of this residue, although point mutations of $Y^{7.58}$ appears to contribute to the stabilisation of the inactive state (75, 76).

1.4.4 D(E)R$^{3.50}$Y motif

The $D(E)R^{3.50}Y$ motif was first characterised in rhodopsin and was thought to be involved the formation of an ionic lock between the $D(E)R^{3.50}Y$ motif and $E^{6.30}/T^{6.34}$, stabilising the inactive structure. However, a similar glutamic acid or threonine is only present in 39 and 28% of the *Rhodopsin* family (14), respectively, and within those containing the requisite residues several do not form an ionic lock (77–79). In all inactive structures, $R^{3.50}$ forms a salt-bridge with the preceding $D(E)^{3.49}$, very likely stabilising the negatively charged form of the residue, and has been implicated in protonation change and activation (80). In the active state, $R^{3.50}$ exists in an extended conformation projecting into the effector binding site, where it is proposed to be involved in G-protein binding and/or activation (62). However, in many X-ray structures the $D(E)R^{3.50}Y$ motif is not resolved at high resolution and it generally displays high B-factors, therefore rendering the analysis of the crystal structures inconclusive (20). However mutagenesis studies on this motif demonstrate its importance, as any mutation of $R^{3.50}$ prevents the activation of G-proteins, thereby inhibiting the receptors ability to signal down this particular pathway (81).

1.4.5 Motifs and their role in GPCR activation

The microswitch motifs take a central role in the activation process of the receptor, though their functional aspects are still debated hotly. Two major models for receptor activation have been proposed; a sequential activation mechanism and the global toggle switch model. Many research groups attribute the activation of GPCRs to single residues, preferring to treat activation as a sequential process, propagating from the toggle switch located below the orthosteric ligand binding site through the Na^+ ion binding site, $NP^{7.50}xxY$ and $D(E)R^{3.50}Y$ motifs to the effector binding site. This model requires that the agonist interact with key residues, leading to a domino effect through the receptor, before triggering the large conformational changes at the intracellular face. However, not all agonists bind within the orthosteric site, and so do not coordinate with these key residues (58).

Alternatively to the sequential activation mechanism proposed above, a concerted action allosteric activation, as described in the global toggle switch model, has been suggested, based upon the Monod-Wyman-Changeux model (82). The microswitches function as important components of the allosteric interface between domains or helices that perform the global conformational change during activation. The interface can then alternate between different states in which the side chains of the microswitches and water molecules are found in different interaction patterns. These distinct states of the allosteric interface can then stabilise different inactive and active conformations. An interesting advantage of the concerted activation model is that it does not require all the components of the microswitches to be present. Moreover, this

model allows for the possibility that different microswitch conformations or binding alters the allosteric interface stabilising slightly different active conformations, giving rise to the biased signalling present in GPCRs. This is supported by the bi-directional allosteric mechanism within GPCRs, where the ligand binding affinity is strongly influenced by G-protein binding at the cytoplasmic face (83).

1.5 Physiological environment and its allosteric impact

In any research undertaken on proteins, their physiological environment must be taken into account. In the case of integral membrane proteins such as GPCRs, this predominantly consists of the plasma membrane, pH, the transmembrane voltage, chemical gradients and ionic composition of the solution. The allosteric impact of each particular environment will be discussed below.

1.5.1 Lipids and their allosteric modulation of GPCRs

Throughout the biological world, a thin hydrophobic film of 30 Å thickness delimits the external environment and internal machinery of the cell. Inside the cell, specialised compartments, often containing important (nucleus) or toxic (lysosome) cargo are also delimited by their own membranes. One of the most important components of the cell is the plasma membrane, harbouring many essential cellular functions, such as: communication with the environment, transport of molecules and metabolic functions. The plasma membrane is composed predominantly of proteins (18-77% (84)), lipids and other small molecules (for review see reference 85). The lipid-protein interactions within the membrane are important as shown by (86, 87).

From the ongoing classification of lipids, there have been over 40,000 different structures as of January 2017 (LIPID MAPS Structure Database; LMSD)(88). Lipids fulfil many functions within the cell, these can be generalised into three main groups: first, in their reduced (saturated) state they are used for long term energy storage by many organisms whereupon β-oxidation they can feed into the citric acid cycle and electron transfer chain. Secondly, they function as a barrier, with the matrix of all membranes composed of polar lipids, consisting of a hydrophilic head group and a hydrophobic tail. Thirdly, lipids are able to act as secondary messengers in signalling cascades and molecular recognition processes. For a more comprehensive background see (89).

As described previously, GPCRs exist as integral membrane proteins and as such it is likely that they can be allosterically modulated by lipid composition and density. Over the years, cholesterol has been shown to bind to GPCRs, with the first direct evidence of cholesterol binding shown in the crystal structure of β_2AR (90). Despite a wealth of information, the allosteric effects of cholesterol are receptor-dependent, with reports of down and up regulation as well as direct and indirect effects (for reviews see reference 91, 92). Recently, it has been shown that phospholipids modulate the activity of GPCRs. For example, a study on the β_2AR, showed that negatively charged phospholipids shift the receptor into a more active state, whist

positively charged phospholipids stabilise the inactive state (93). In the crystal structure of β_2AR, a high proportion of positively charged residue clusters at the receptor-lipid head group interface (90). It is therefore conceivable that the lipid allostery is also receptor specific, dependent on the charge distribution of residues. The modulation of the active conformation by lipids fits together with the proposed allosteric activation model.

1.5.2 Modulation by pH and receptor protonation

The pH within both the cytoplasm and the extracellular environments is strictly regulated to be between pH 7-7.4 (
Table **1-1**). However in certain conditions typically accompanied by inflammation and tissue acidosis (e.g. arthritis, tissue damage, etc.), the extracellular pH decreases to a pH of 5-7. In the specific situation of receptor signalling, tissue acidosis modulates the signalling patterns of proteins expressed on the cell surface. This can have significant effects on the protonation of ligands (94) as well as the function of GPCRs (95).

Research by Kobilka *et al* has shown that the basal activity and agonist induced activation in the β_2AR are pH sensitive, with greater activity at pH 6.5 than that at pH 8 (96). The majority of ionisable residues in the *Rhodopsin* GPCR family are solvent exposed and correspond either to arginine and lysine residues, which pK_as are typically >= 10, or to glutamates and aspartates, which pK_as are generally ~4. Such residues are, therefore, unlikely to be titrating under physiological pH conditions (~7). The only likely exceptions are histidine residues which typically titrate at pH 7. The *Rhodopsin* GPCR family contains three acidic residues within the transmembrane domain: $D^{2.50}$, $D^{3.32}$ and $D^{3.49}$. Due to their buried position within the receptor, these aspartate residues are likely to have a higher pK_a than that of a solvent exposed aspartate, and therefore have a higher probability of changing protonation state at neutral pH. The $D^{3.32}$ is unlikely to be the pH sensor due to its relatively low conservation when compared to $D^{2.50}$ and $D^{3.49}$. Therefore only the aspartate residues at positions 2.50 and 3.49 remain likely to be the pH sensor, both of these residues are coordinated by positive groups. As previously described, the $D^{2.50}$ is located in the Na^+ ion-binding pocket, where its negative charge is likely to be stabilised by the Na^+ ion, whilst the charged state of $D^{3.49}$ is stabilised by the salt bridge formation with $Arg^{3.50}$. Of interest, these effects can also be seen in the Dopamine D2 receptor, where the receptor is strongly sensitive to both pH and the presence of Na^+ (97).

1.5.3 Ionic conditions and the Na^+ effect

The driving force of many physiological processes in the membrane, originate from ionic gradients across the aforementioned plasma membrane. Plasma membranes contain many transporters and channels, which have evolved to maintain strict ionic compositions on both sides of the membrane (
Table 1-1). Here I will not describe all the roles and effects of ion concentration, but will highlight an important phenomenon, which has been present in GPCRs since they evolved.

Component	Intracellular concentration (mM)	Extracellular concentration (mM)
Na^+	5-15	145.0
K^+	140	5.0
Mg^{2+}	0.5	1-2
Ca^{2+}	10^{-4}	1-2
H^+	pH 7.2	pH 7.4
Cl^-	5-15	110.0

Table 1-1: Ion concentrations within cells
Comparison of ion concentrations between the intracellular and extracellular solutions.

Almost half a century ago, a striking effect was reported for the opioid receptors (98). The concentration of Na^+ was shown to negatively modulate agonist binding to opioid receptors without significantly modulating antagonist binding. This was termed the "sodium effect" and was used as a biochemical assay to differentiate agonist and antagonistic drugs in opioid receptors (99). Since then, many receptors classes have displayed similar biochemical properties; histamine, dopamine, adrenergic, opioid and neuropeptide receptors etc. (68, 100). Prior to the structural information on the Na^+ binding site, Na^+ was shown to bind to $D^{2.50}$ by mutational studies of the Na^+ binding pocket. However, these mutations severely disrupt the signalling of the receptor, though are still able to retain their agonist binding properties (65, 75). The allosteric effects triggered by Na^+ have been described at physiological concentrations (~10 – 140 mM) suggesting a biological role (101, 102). The Na^+ concentration can significantly affect the constitutive activity of receptors, in a similar manner to point mutations within the Na^+ binding pocket (103–105). These published results support the notion that the Na^+ ion stabilises the inactive state of the receptor.

Though contradictory in their reported functional effects, all mono and divalent cations as well as anions have been shown to modulate GPCR signalling to varying degrees (100, 106, 107). The variability of results arises initially from the intention to optimise the experimental conditions, by the use of purified cell membranes (98, 102, 107). The functional studies on GPCR ion allostery, are therefore highly heterogeneous in terms of receptor types, membrane composition, parameters and consequently the results obtained, especially the order of efficacy (100, 101).

1.5.4 Transmembrane voltage

The resting potential of the cell is governed by the concentration gradients of multiple ionic species such as K^+, Na^+ and Cl^-, maintained by an array of ATP driven ion pumps. The movement of each ionic species down its chemical gradient through its respective ion channels will generate a charge imbalance across the membrane, thereby shifting the membrane potential to the equilibrium potential of that ion. The equilibrium potential is the point at which there is no net flow through any open channels. Where the opposing electrical and chemical gradients are at equilibrium, for each ionic species this can be calculated using the Nernst equation (Eq. 1-1).

$$V_{eq} = \frac{RT}{zF} ln\left(\frac{[X]_{out}}{[X]_{in}}\right) \qquad \textbf{[1-1]}$$

Where V_{eq} is the equilibrium potential, R is the universal gas constant, T is temperature (K), z is the valence of the ionic species, F is Faraday's constant, $[X]_{out}$ is the concentration of ionic species in the extracellular solution and $[X]_{in}$ is the concentration of ionic species in the intracellular solution.

Therefore, the movement of each of the aforementioned ions through the membrane will contribute to the membrane potential. However, the membrane potential is also determined by the permeability of the membrane to each ion. The permeability of each ion is directly proportional to the total number of open channels for that particular ion, therefore the membrane potential can be calculated using the Goldman-Hodgkin-Katz equation (Eq. 1-2).

$$V_m = \frac{RT}{F} ln\left(\frac{P_k[K]_o + P_{Na}[Na]_o + P_{Cl}[Cl]_i}{P_k[K]_i + P_{Na}[Na]_i + P_{Cl}[Cl]_o}\right) \qquad \textbf{[1-2]}$$

Where V_m is the membrane potential, R is the universal gas constant, T is temperature (K), F is Faraday's constant, P_κ is the membrane permeability of K^+ (permeability of ions are relative to P_κ), P_{Na} is the relative membrane permeability of Na^+, P_{Cl} is the relative membrane permeability of Cl^-, $[X]_o$ is the concentration of ionic species in the extracellular solution and $[X]_i$ is the concentration of ionic species in the intracellular solution.

The electrochemical driving forces (V_{DF}) of each ionic species is quantified by the difference between the membrane potential and the equilibrium potential ($V_{DF} = V_m - V_{eq}$). Therefore, if Na^+ has a V_{eq} of 60 mV and the cell has a V_m of -70 mV, the V_{DF} of Na^+ is -130 mV, giving rise Na^+ influx into the cell. In contrast, the V_{eq} of K^+ is ~ -96 mV, giving rise to a V_{DF} of ~26 mV, leading to K^+ efflux.

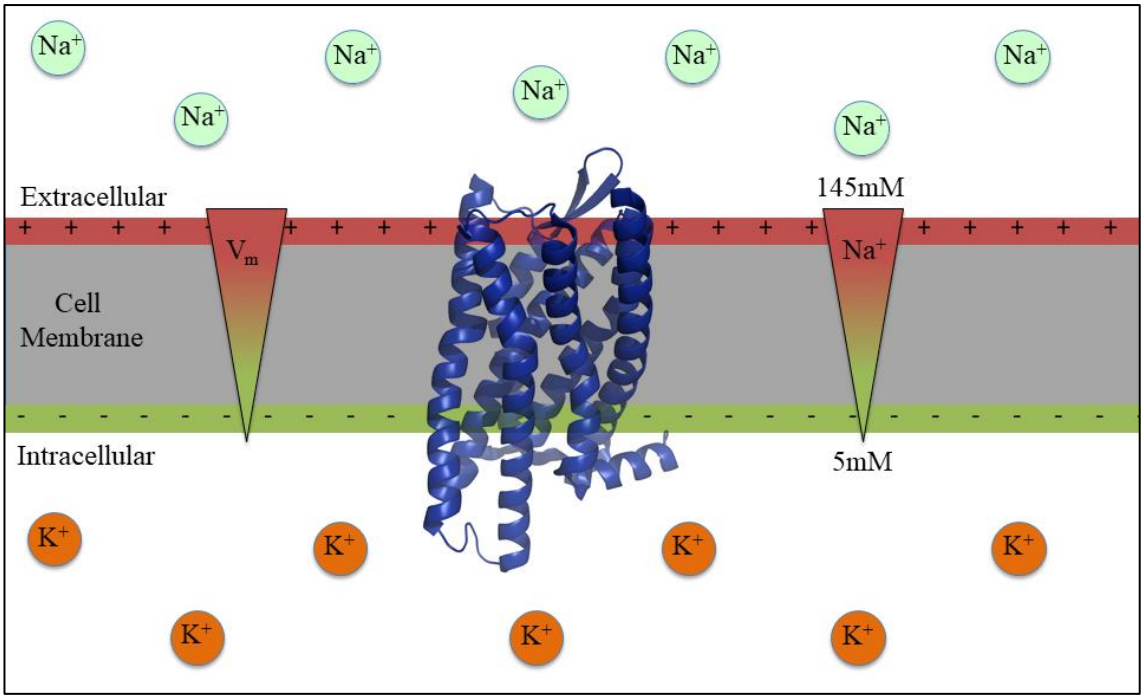

Figure 1-15: Electrical and chemical gradients across a cell membrane

The constituents in a simplified electrochemical gradient: electrical and Na^+ concentration gradient. **(Left)** Displays the electrical gradient from positively charged extracellular surface to the negatively charged intracellular surface of the membrane. The approximate strength of the electric field is 10^8 Vm^{-1}. **(Right)** Displays the concentration gradient of Na^+ from ~140mM in the extracellular to the low 5mM intracellular concentration. In this particular case both the Na^+ concentration gradient and the V_m act synergistically. However, they can oppose each other, as is the case of K^+ concentration gradient and V_m.

The hydrophobic core of the lipid bilayer acts as the dielectric of the capacitor, separating the charge differences and thereby yielding the membrane potential (Eq. 1-3).

$$V_m = \frac{\Delta q}{C} \qquad \textbf{[1-3]}$$

The transmembrane ion gradients generate the V_m by leading to a small charge imbalance (Δq) across the lipid bilayer (capacitor), which has a specific capacitance (C)

Since the membrane core is extremely thin (20-30 Å), V_m is translated into an intense electric field of up to ~10^8 Vm^{-1}. Many proteins can sense this electric field and use it to regulate their function, such as ion channels during action potentials. As all proteins contain charged residues, it is simple to imagine how these charges can be reorganised, inducing a conformational change in response to the V_m. The portion of the protein that is sensitive to changes in the V_m is called a voltage sensor. The movement of the voltage sensor charges induces a transient current (gating current), which can be measured both computationally and experimentally, thereby providing direct information on the conformational changes induced (see below).

As previously mentioned the membrane electric field is often sensed through the translocation of charges. The predominant method of voltage sensing, is with charged residues and elicit gating currents, for example the shaker potassium channel Kv1.2 (108). Of note, changes in electric fields can also move free ions (109), and modulate the pK_a of charged residues and lead to changes of the protonation state, which would also be able to initiate conformational changes.

Many transporters, ion channels and receptors conformationally respond to changes in the V_m. As all membrane bound proteins exist within a strong electric field of up to ~10^8 Vm^{-1}, any charge (Q_g) within the TM region of these proteins are therefore moving within an electric field and will produce an electric current (Figure 1-16, Figure 1-17). To maintain continuity, the charges in both the intra and extracellular solutions also move in proportion to the total amount of charge moving within the membrane, thereby generating a current that is measurable in the external circuit (Figure 1-16). The most common experimental method of measuring gating charges is via the cut open oocyte (xenopus) technique (Figure 1-17)(110). The movement of a gating charge is a direct electrical marker of any conformational change within most membrane proteins (for review see reference 111).

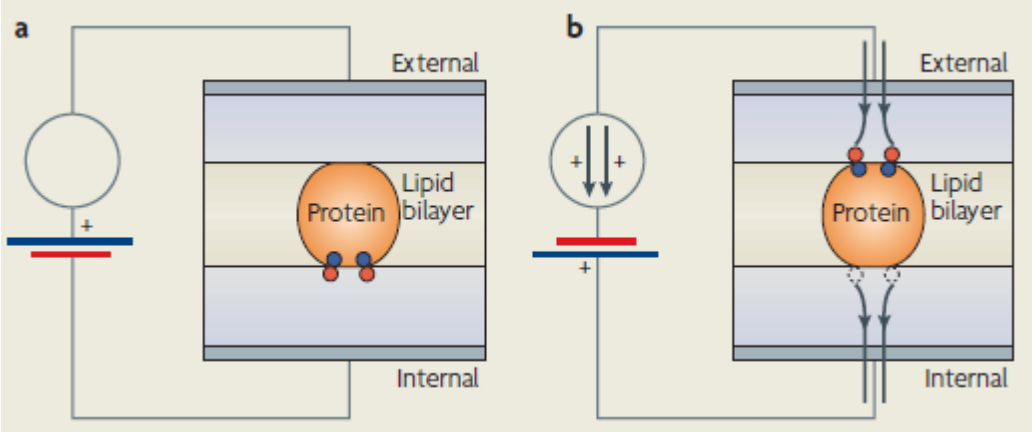

Figure 1-16: What is a gating charge?

In the above example a membrane and protein are immersed between two solutions (internal and external), which connected by electrodes via the voltage clamp (battery). Here, the membrane protein contains 2 positive charges (blue circles), and negative counter ions (red circles) in the internal solution (**A**). On the reversal of the V_m (**B**) the proteins positive charges move from the internal surface to the external surface. In order to keep the V_m constant, the voltage-clamp circuit removes 2 negative charges (dashed circles) from the internal membrane solution and adds 2 negative charges to the external membrane solution. The recorded current upon the voltage switch therefore reflects the movement of 2 positive charges moving from the internal solution towards the external solution. However, if the 2 charges only move halfway across the electric field (transmembrane domain), then only 1 external counter ion will move. In the terms of the current, the charge transferred is the product of the total charge moved times the fraction of the electric field. Using the aforementioned example: the total charge (2) * by the fraction of electric field (0.5) = the gating charge (1). Figure adapted from (111).

As described above, gating charges are able to provide a direct measurement of the movement of charges in membrane proteins influenced by the V_m. It is possible to quantify gating charges either computationally or experimentally. The advantages of using a computational approach allows us to be able to look at one protein at a time, easily mutate and change parameters of specific residues though are limited by simulation time and the high V_m used. In contrast, the majority of electrophysiology experiments use membrane patches with an estimated number of proteins, and they rely heavily on an estimation of the number of receptors in the patch area. Therefore, the measurements can vary widely between groups (Table 3-1). The advantage of the experimental methodology is the use of native membranes, physiological V_m and no prior structural knowledge of the protein of interest.

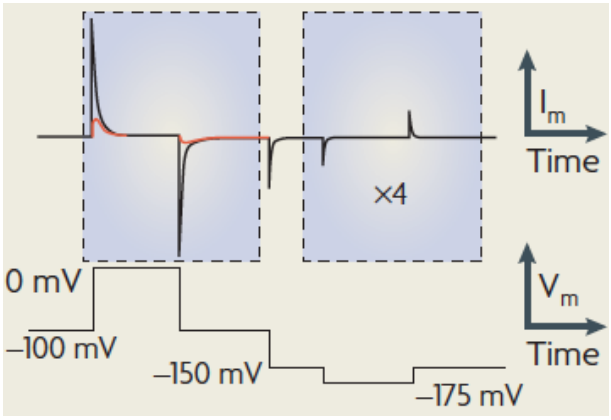

Figure 1-17: Experimental recordings of gating currents

To measure gating currents, the membrane patch is subjected to a voltage step; in the case shown above, this is from -100 mV to 0 mV. This generates a brief spike in current (I_m). This current contains both the gating current (I_g: red line) and the linear capacitive current (I_c: black line). Therefore to separate these currents, the subtracting pulse (P4) which is a voltage step that does not affect the voltage sensor, and therefore only generates a linear current is subtracted from the I_m. Figure adapted from (111).

Importantly in recent years, the conformation, function and downstream signalling of GPCRs has been experimentally shown to be modulated by V_m (112–117). As shown by Rinne *et al* (112), the V_m can either enhance or attenuate the transmitted agonist signal depending upon the ligand and the environment of the ligand binding site. The small point mutation of $N^{6.52}Q$ in the muscarinic receptor, can reverse the voltage effects of the bound ligand. However the reasons behind this switch are still unknown, the mechanism underpinning GPCR activation remains elusive. In addition to GPCR signalling being V_m sensitive, the ligand binding affinity has also shown to be voltage-dependent (117, 118).

The V_m sensitivity of GPCRs may have significant physiological impact upon the cell. For example, neurons exhibit a shifted V_m in various regions of the brain and during development (119). Therefore the exact action of GPCR ligands is likely to depend upon the cellular context. In excitable cells, the physiological V_m during action potentials fluctuates between -90 and 50 mV, in extreme cases as demonstrated by hair cells in the inner ear a V_m of 150 mV can be reached (120). This could dynamically alter the signalling profile of each receptor and ligand by changes in the excitation state of the cell (Figure

1-18). For example this has been demonstrated in synaptic neurotransmission, where the kinetics of neurotransmitter release is reshaped on a millisecond timescale (121). Smaller long term changes in the V_m, such as the slow oscillations throughout its cell cycle (122). As well as distinct spatial V_m differences in subcompartments and substructures (123). Interestingly, a range of malignant cells types possess a more depolarised membrane than quiescent cell, although the medical relevance of this observation remains unclear (122, 124)

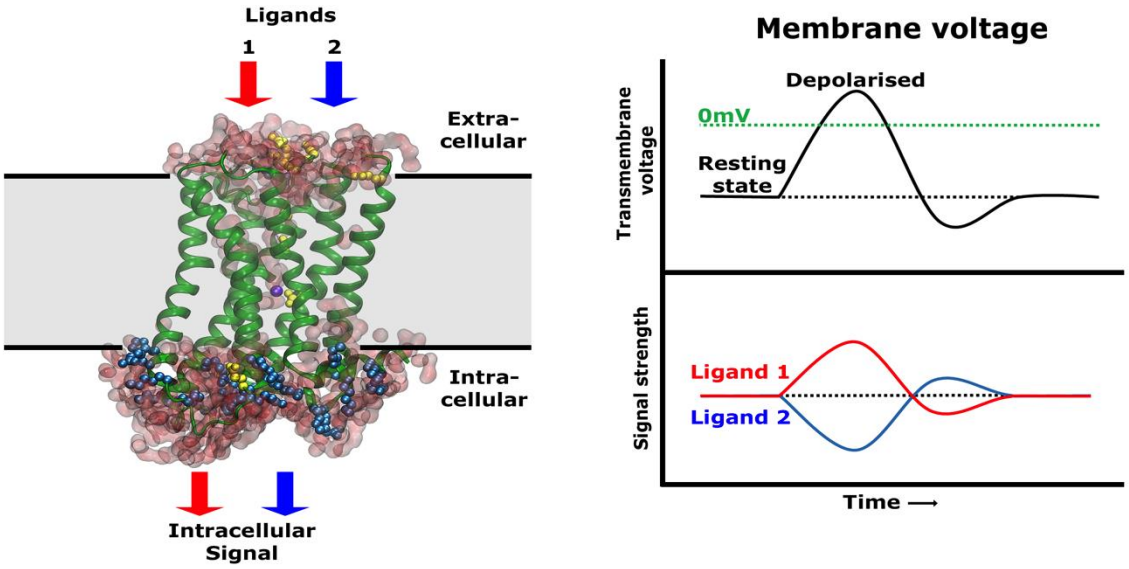

Figure 1-18: The dynamic modulation of GPCR signalling in excitable cells

(Left) An example of two ligands activating the same receptor and two distinct downstream signalling processes. **(Right)** Effects of V_m upon each ligand: upon depolarisation the signal strength induced by ligand 1 is attenuated whilst the signal by ligand 2 is enhanced. This potentially allows the V_m of the cell to dynamically modulate the signalling profile of individual ligands. Figure adapted from (125).

1.6 Project aims

Previous research on GPCR activation and signalling, have demonstrated that the physiological environmental factors such as transmembrane voltage, The Na^+ effect, pH and lipid composition are strong allosteric modulators (see section 1.5). In 2006 it was demonstrated by Ben-chaim et al (118), that the modulation of V_m on the physiological range induces conformational changes within the m2 muscarinic receptor, giving rise to gating charges between 0.7 - 0.85 e. Since then gating charges in the range of 0.5 - 0.85 have been recorded in several members of the *Rhodopsin* GPCR family: m1, m2 muscarinic receptors and the α_{2A} adrenergic receptor (112, 113, 118, 126). Despite these measurements, the nature and location of the voltage sensor has remained elusive, therefore eluding to a more complex voltage sensor composed of multiple components.

The initial aims of this project were to understand the effects of V_m changes upon the receptor. This was achieved by looking at the structural and consequences of V_m upon two GPCRs via atomistic molecular dynamics (MD). I first chose to investigate the δ-Opioid receptor, due to the availability of a high quality

crystal structure, its clinical importance and its exclusive distribution within the central nervous system (CNS), where it is frequently exposed to rapid and extreme changes to V_m. In addition, I included the m2 muscarinic receptor, on which the majority of experimental measurements of charge rearrangements were performed (118, 126).

Since the crystallisation of the A_{2A} adenosine, β_1 adrenergic, protease-activated and δ-Opioid receptors revealing a Na^+/water cluster within the core of transmembrane bundle (Figure 1-14)(64–67). It has become established that the inactive *Rhodopsin* GPCR family structures contain a Na^+ bound within the ion binding pocket. However, interestingly, subsequent crystal structures of *Rhodopsin* GPCRs in an active state show a collapsed Na^+ ion binding site (20, 74, 127–131), prompting the question of what happens to the Na^+ ion upon activation, how does it leave the receptor and what are the consequences?

Therefore, using a combination of computational techniques on the m2 muscarinic receptor. I will investigate the position of the Na^+ ion and any subsequent changes in receptor conformation upon receptor activation. The M2R will be simulated under physiological conditions using the CompEL approach, allowing the inclusion of ion gradients and transmembrane voltage.

Small mutations in the *Rhodopsin* family of GPCRs can drastically alter GPCR signalling profiles from β-arrestin to G-protein and vice versa. In the paper published by Fenalti et al (65), they presented a single residue mutation at position 3.35 in the δ-OR, one of the least conserved residues within the Na^+ binding site. This mutation to either a valine or alanine resulted in a significantly reduced or abolished Na^+ binding. These mutations also had a major impact upon the signalling pattern of the receptor, resulting in a constitutively active receptor in the β-arrestin biased pathway.

To investigate the effects of the $N131^{3.35}$ δ-OR mutants, I will use microsecond length simulations to study any conformational changes within the receptor. Additionally, I will examine the effects of the protonation states of $D95^{2.50}$ and $D145^{3.49}$ upon the receptor conformation.

Chapter 2. Theory and simulation setup

2.1 Theory

It has been more than 40 years since the first Molecular Dynamics (MD) simulation of a macromolecule with a biological interest has been published (132). The original simulations were less than 10 ps in length, to compare; simulations now easily access the microsecond range, however with the availability of resources such as the Anton supercomputer, simulations can reach the millisecond range. However, much of the improvements in MD simulations are reinvested back into studying much larger and more complex systems of large protein complexes. In the subsequent sections, I will explain specialised state-of-the-art MD techniques, which are pertinent to the following chapters, such as: computational electrophysiology, gating charge calculations and umbrella sampling (for in depth information see (133)).

Proteins typically consist of between ten to hundreds of amino acids, this amounts to several thousand atoms for the protein alone. The dynamics of the proteins include bond vibrations at the femtosecond timescale to conformational changes of protein domains at the mico- to milli-second timescale. To date, the best computational method that can accurately describe the molecular dynamics of proteins and access physiologically relevant timescales is Molecular Dynamics (MD) simulations.

2.1.1 The core concepts of molecular dynamics

The classical forcefields in MD simulations allow for the calculation of the potential energy of a system, as a function of the nuclear position of each atom. Under the Born-Oppenheimer approximation, the motions of the atomic nuclei and electrons can be treated independently.

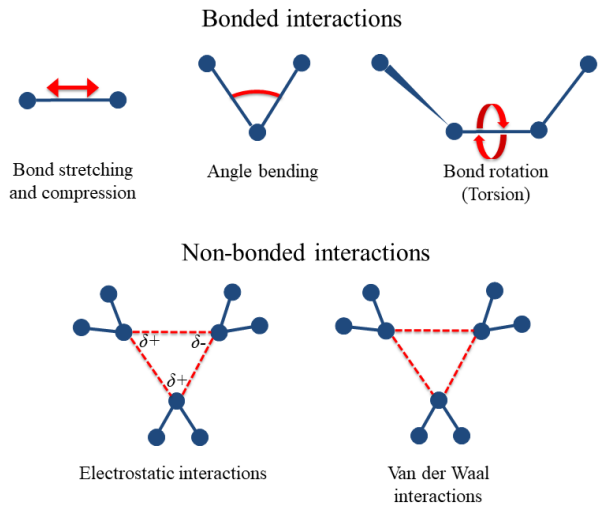

Figure 2-1: The molecular dynamics force field

A schematic representation of the five key elements which compose empirical molecular dynamics forcefields. **(Top)** The three bonded interactions comprise terms for bonded interactions: U_{bonds}, U_{angles} and $U_{torsions}$. **(Bottom)** The two non-bonded interactions comprise of electrostatic modelled by a Coulomb potential (U_{Coul}) and the Van der Waals modelled by a Lennard-Jones potential(U_{LJ}).

$$U(\boldsymbol{r}^N)_{bonded} = U_{bonds} + U_{angles} + U_{torsion}$$

$$U(\boldsymbol{r}^N)_{bonded} = \sum_{bonds} \frac{K_i}{2}(l_i - l_{i,0})^2 + \sum_{angles} \frac{K_i}{2}(\theta_i - \theta_{i,0})^2 + \sum_{torsions} \frac{K_i}{2}(1 + \cos(n_i - \gamma_i))^2$$

$$U(\boldsymbol{r}^N)_{non-bonded} = U_{LJ} + U_{coul}$$

$$U(\boldsymbol{r}^N)_{non-bonded} = \sum_{i=1}^{N} \sum_{j=i+1}^{N} \left(4\varepsilon_{ij} \left[\left(\frac{\sigma_{ij}}{r_{ij}} \right)^{12} - \left(\frac{\sigma_{ij}}{r_{ij}} \right)^{6} \right] + \frac{q_i q_j}{4\pi\varepsilon_0 \varepsilon_r r_{ij}} \right)$$

$$U(\boldsymbol{r}^N)_{system} = U(\boldsymbol{r}^N)_{bonded} + U(\boldsymbol{r}^N)_{non-bonded} \qquad \textbf{[2-1]}$$

Where U denotes the potential energy which is the function of the vector (**r**) of N particles ($\mathbf{r}^N = \mathbf{r}_1, \mathbf{r}_2, \ldots, \mathbf{r}_N$). The force field parameters for the bonded interactions; bond length and angles are described as a harmonic potential around their reference value $l_{i,0}$ and $\theta_{i,0}$, respectively, with their respective force

constants k_i. The third bonded interaction is described by a torsional potential around the dihedral angle with a multiplicity of n, K_i is the torsional barrier height and γ_i is the phase of the dihedral. The electrostatics interactions are treated using Coulomb's law describing the interactions between the partial charges q_i and q_j on their respective atoms, separated by the distance r_{ij}, ε_r is the relative permittivity of the medium included within the non-bonded term, which is given by the permittivity of the substance ε_s in relation to the absolute permittivity of a vacuum ε_0. The van der Waals (vdW) interactions can be treated using the 12-6 Lennard-Jones potential, where the repulsive interactions arising from the overlap of the electron cloud can be treated as $\left(\sigma_{ij}/r_{ij}\right)^{12}$ whilst the attractive interactions arising from the dispersive forces are treated by $\left(\sigma_{ij}/r_{ij}\right)^{6}$. The width (finite distance at which the inter-particle potential is zero) is described by σ_{ij} and depth of the Lennard-Jones potential by the ε_{ij}. The Lennard-Jones potential provides a computationally efficient approach to modelling the vdWs interaction as the r^{12} term can be computed as the square of the r^6 term.

The non-bonded interactions are the most computationally expensive part of the force calculations. A simple way of enhancing the calculation efficiency is by applying a cut off to the non-bonded interactions, this is typically in the range of 10-14 Å, though throughout this work an intermediate cutoff of 12 Å was chosen. This cutoff works well with the rapidly decaying Lennard-Jones potential, however produces errors when applied to the Coulomb potential (134). Therefore, a Particle Mesh Ewald sum (PME) for the electrostatic interactions is implemented within the simulations, which separates the electrostatics into short and long range interactions. The short range interactions are calculated directly whilst the long range are calculated in reciprocal space (135).

MD forcefields developed varying strategies to parameterise the above terms. Throughout this thesis, I will use the amber99sb-ildn force field (136). The amber99sb-ildn is one of the most commonly used forcefields from the amber package, updated in 2010 from the original amber forcefield amber99sb in which it was found to over stabilise α-helices (137). The backbone dihedrals for isoleucine, leucine, aspartate and asparagine were updated to correct for this (136). The amber99sb-ildn forcefield has been developed for both proteins and nucleic acids, therefore the non-protein/nucleic portions of the system require additional parameters.

Throughout my simulations, I used updated Berger lipid parameters which were parameterised using a united atom approach, in which the non-polar hydrogens are unified with the carbon they are bound to (138, 139). The resulting CH, CH2 and CH3 groups are treated then as a united atom, which has been adjusted for the correct Lennard-Jones parameters, mass and charge. Explicit water molecules were used throughout this thesis, the SPCE water model (140) was used in Chapter 3, whilst TIP3P (141) was used in Chapters 4 and 5 due to the increased diffusion coefficient accuracy. In both cases the water bond angles and distances were constrained by SETTLE (142).

The nuclear dynamics in MD simulations are described by Newton's second law (Eq. 2-2).

$$-\frac{\partial U}{\partial \boldsymbol{r}_i} = \boldsymbol{F}_i = m_i \boldsymbol{a}_i = m_i \frac{d\boldsymbol{v}_i}{dt} = m_i \frac{d^2 \boldsymbol{r}_i}{dt^2} \qquad \textbf{[2-2]}$$

The negative gradient of the potential energy (U) is the force ($\boldsymbol{F}_i$) acting on an atom at position $\boldsymbol{r}_i$. Where m_i is the atomic mass, $\boldsymbol{a}_i$ is acceleration, $\boldsymbol{v}_i$ is the velocity. The forces on each atom over a given timestep (dt) are assumed to be constant. Therefore, after each timestep the new atomic coordinates and forces are updated iteratively, over the desired MD trajectory length.

Newton's equations of motion are integrated with the Verlet leapfrog algorithm, where the integration timestep is generally chosen to be smaller than the fastest motion of the system. The bond vibrations involving hydrogen occur on the femtosecond timescale, preventing the timestep from exceeding 1fs, however, throughout this thesis I include the LINCS algorithm which allows for greater timesteps to be chosen (143). Despite using the LINCS algorithm, the time step is still limited by the high-frequency bond-angle vibrations involving hydrogen atoms. The removal of these degrees of freedom from the system by constructing certain hydrogen atoms as dummy atoms (termed virtual sites) such as methyl groups, allowing the time step to be increased to 4 fs (144).

The microscopic behaviour of the MD simulations described here, can be linked to the experimentally measured macroscopic properties, such as pressure and energy by statistical mechanics. In MD simulations a statistical ensemble is obtained by the evolution of the system over time (MD trajectory), from which macroscopic properties can be taken as time averages. According to the ergodic hypothesis, the resulting time average is equal to the ensemble average observed in experiments (Eq. 2-3).

$$\langle A \rangle_{ensemble} = \langle A \rangle_{time}$$
$$Ensemble\ average = Time\ average \qquad \textbf{[2-3]}$$

For a realistic simulation of a protein it must be as close to *in vivo* as possible. For a membrane bound protein, a lipid bilayer, water and ions (NaCl) are added to the system. However, the addition of these solvating molecules within a finite system box generates large artifacts, such as boundary artifacts. Here, this is solved by using periodic boundary conditions (PBC) in which the system is modelled as an infinitely replicating box. The PBC removes errors generated from artificial boundaries, however care must be taken not to choose a too small box in which the particles can interact with each other.

Due to approximations when calculating the non-bonded interactions, the potential energy of the system fluctuates. Therefore, the simulation temperature T is adjusted to compensate, the systems temperature is coupled to a heat bath by the v-rescale method with a reference temperature of T_0 (310 K) with the coupling constant of τ_T 0.2 ps (145). The simulation system is grouped in its main constituents; protein and lipids, whilst the water and ions are combined into one group. The separation of the system into its main

constituents increases the accuracy of the simulation temperature, as the bulk solvent contains a higher number of interactions and therefore undergoes a higher degree of thermal fluctuation in comparison to the protein and lipids. The temperature coupling assumes that the system is at thermal equilibrium, therefore the aforementioned groups are treated individually, consequently removes any differences between the main constituents.

2.1.2 Computational electrophysiology (CompEL)

The use of PBC, which are required to remove surface effect artifacts, prevents the generation of electrochemical gradients across a single bilayer system (Figure 2-2 A). For the CompEL setup, a single bilayer is therefore duplicated along the z axis, thereby forming two discrete aqueous compartments (Figure 2-2: black and blue squares) (as previously described in (146, 147)). Under physiological conditions the lipid bilayer is impermeable to water and ions, which allows the conditions for each compartment to be distinct from each other. In this way, the ion type and concentration, pH, osmotic pressure and electric charge in each compartment can be altered independently according to the aim of the study. Upon the insertion of a channel within the membrane rendering the membrane permeable. The CompEL protocol implemented within GROMACS monitors the number of ions within each compartment. If an ion moves from one compartment to another, creating a mismatch from the chosen concentration, an ion is swapped with a water molecule in the other compartment until the mismatch is corrected.

To generate a transmembrane potential, a charge imbalance (Δq) between the aqueous compartments is required (Figure 2-2 B). If a single ion with a charge of 1e is moved from compartment A to compartment B, this generates a Δq of 2e in the convention used by CompEL, therefore by using the capacitance (1.28×10^{-18} F) of the membrane and protein in this particular system, we obtain a V_m of ~250mV per ion exchange in agreement with equation 1-3. In spite of the internal charge imbalance within the system, the total charge of the double bilayer system remains zero. The perturbations arising from the ion-water exchange are minimised by only selecting molecules which fulfill a certain distance criterion from the membrane boundary, and therefore from the protein of interest.

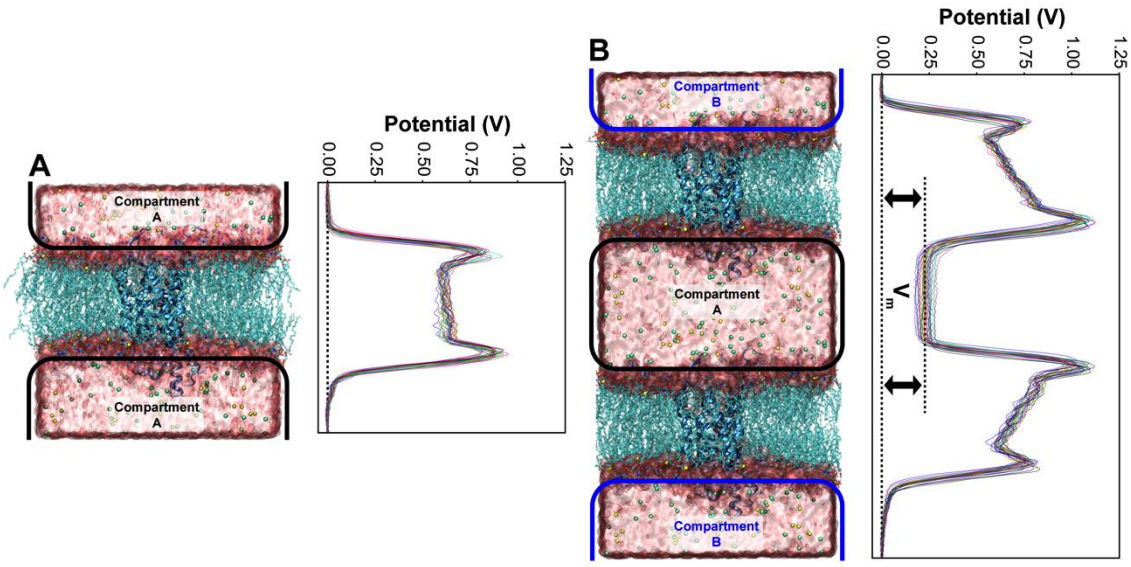

Figure 2-2: Single bilayer and dual bilayer (CompEL) setup

(**A**) Left: a standard single bilayer system (~92 x 88 x 97 $Å^3$) containing a membrane bound GPCR with the two compartments connected by periodic boundary conditions (PBC). Right: No potential difference exists between the intracellular and extracellular sides of the lipid bilayer. The potentials are continuous due to the periodic boundary conditions (**B**) Left: Example of the dual bilayer approach, with compartment A and B (blue and black squares, respectively) delimited by the impermeable lipid bilayer. Right: Shows an example of the potential between compartments, with the application of a single ion imbalance, generating a V_m of ~250mV.

2.1.3 Deriving the gating charge

There are three main methods to determine gating charges computationally: the first evaluates the dependence of the local electrostatic potential on the V_m, this approach requires the calculation of the electrostatic potential over three dimensions and the convergence of the local potential (148). The second is the use of perturbative free energy calculations to determine the contributions to the Q_g via the charging free energy of chosen amino acids (149). The aforementioned methods are computationally expensive and are difficult to apply to a large range of residues and cannot encompass all movements involved in voltage sensitivity. Throughout the thesis, I used a method derived from computational electrophysiology (see above), enabling both accurate estimates and mechanistic insight into the contributions of charges to the Q_g. This method is based upon the simulation of the membrane protein capacitor charging process, originally developed by Treptow et al (150), allowing the direct determination of the Q_g, and any change in capacitance resulting from most components of the voltage sensitivity (Figure 2-3)(151).

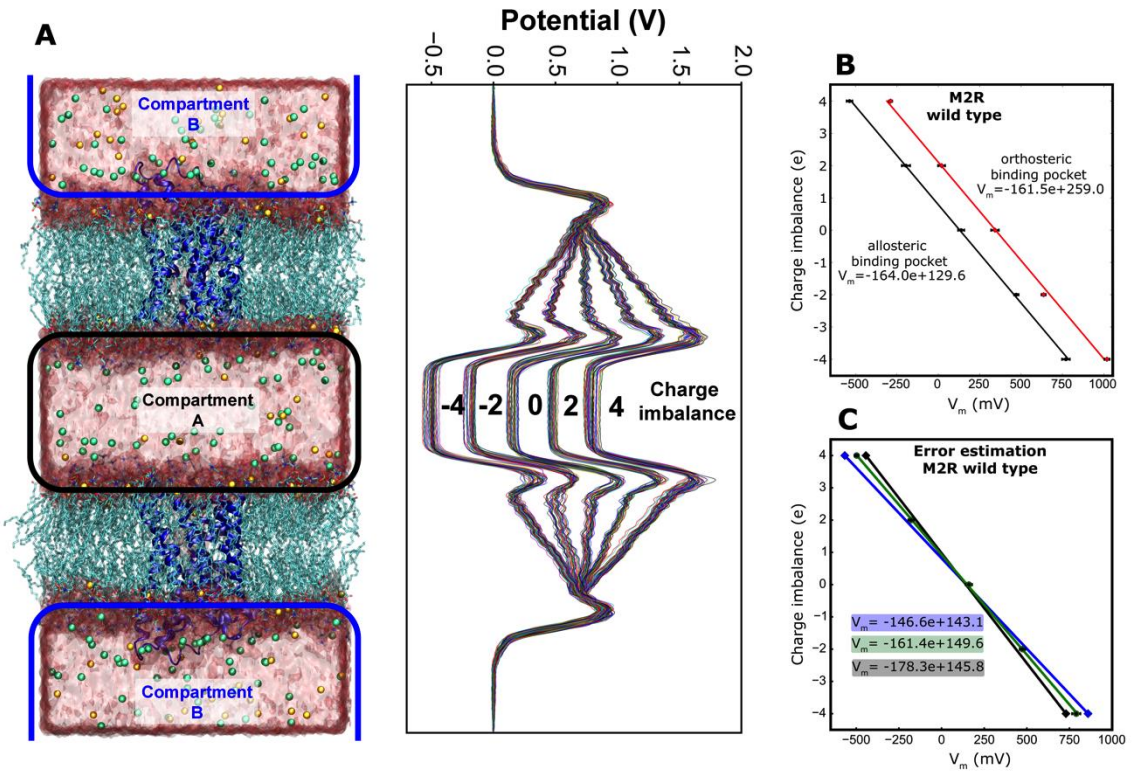

Figure 2-3: Gating charge recordings

(**A**) Left: Example of the inverted bilayer approach, with compartment A and B (blue and black squares, respectively) delimited by the impermeable lipid bilayer. Right: Example Potential between compartments calculated along the z-axis. Each ion imbalance generates a Potential imbalance of ~250mV (Figure 2-2). (**B**) An example of the membrane voltage plotted against charge imbalance, exhibiting a linear relationship. The slope of the curves denotes the inverse capacitance of the system, which is nearly identical for the two Na^+ ion positions. The voltage can display either a right of left shift depending on the direction of ion movement, the example shown here displays the effect of the ion movement from the allosteric binding pocket to the transient binding site within the orthosteric ligand binding site. Error bars are the standard deviation of the voltage fluctuation. (**C**) Shows the minimum and maximum capacitances derived from the lowest and highest V_m and vice versa measured in the M2R. This gives the error in the capacitance determination.

The use of an adapted CompEL system is required for determining gating charges. In contrast to the standard CompEL, one of the protein/membrane groups are inverted. Therefore, the intracellular and extracellular domains of the receptor face each other, respectively. In this inverted setup, the charge distributions of the proteins do not cancel each other out, but are additive to one another. Therefore, in most cases the charge imbalance arising between the compartments purely due to the distribution of charges in the proteins is neutralised by adding ions (NaCl). The inverted double system also has the benefit of doubling the signal to noise ratio. The signal noise of 10-30mV arises from the association and dissociation of the bulk solution ions to the membrane.

An initial charge titration of the system is conducted, which provides the capacitance (C) of the system. In the case of proteins with deep hydrophilic pockets low position restraints in the z direction upon the ions in the bulk solvent can be applied to prevent ingress. In the example shown above (Figure 2-3 B), the charge imbalance and V_m have a linear relationship, with any charge movement within the membrane-giving rise to a left or right shift in V_m. Regardless of the charge movement within the receptor the capacitance of the system remains constant. The gating charge (Q_g) can therefore be calculated by equation 2-4.

$$Q_g = \frac{\Delta V_{m(i,j)} C}{4} \qquad \textbf{[2-4]}$$

During the calibration of the system (Figure 2-3 B), the slope of the relationship refers to the inverse capacitance (C) of the membrane and protein. Once the capacitance of the system is known, the V_m difference between each conformational state ($\Delta V_{m(i,j)}$) at a given charge imbalance allows the determination of the gating charge (Q_g). Due to the CompEL convention, the movement of a single charge from the intracellular to the extracellular induces a charge imbalance of Δq of 2 e. Additionally, the inverted protein/membrane system doubles the calculated gating charge, therefore the gating charge must be halved.

$$\mathrm{Q_{err}} = \frac{V_{m(i)} C_{min} - V_{m(i)} C_{max}}{8} \qquad \textbf{[2-5]}$$

Equation 2-5 describes the error estimation for the gating charge calculation. The error (Q_{err}) is derived from the minimum and maximum possible capacitances of the system, C_{min} and C_{max}, respectively (Figure 2-3 C). Throughout the remaining chapters, all errors involving the CompEl derived gating charges are denoted with ± Q_{err}.

2.1.4 Umbrella sampling and potential of mean force

To calculate the potential of mean force along a specific reaction coordinate, a technique called umbrella sampling is typically used. This technique aims to overcome sampling problems arising from energetically unfavourable conditions by restraining specific subsections of the simulation by an additional potential (harmonic potential, equation 2-6).

$$w_i(\xi) = \frac{K_i}{2}(\xi - \xi_i^c)^2 \qquad \textbf{[2-6]}$$

A set of simulations (umbrella windows) are carried along the reaction coordinate which are restrained at the position $\xi_i^c (i = 1, \dots, N_w)$ by an umbrella potential with a force constant of K_i. From each simulation an umbrella histogram is extracted $h_i(\xi)$, which represents the probability distribution $P_i^b(\xi)$ along the previously described reaction coordinate which is biased by the umbrella potential $w_i(\xi)$ (Eq. 2-7). One of

the widely used methods to unbias the probability distributions is the weighted histogram analysis method (WHAM).

$$P(\xi) = \frac{\sum_{i=1}^{N_w} g_i^{-1} h_i(\xi)}{\sum_{j=1}^{N_w} n_j g_j^{-1} \exp[-\beta(w_j(\xi) - f_i)]} \quad \textbf{[2-7]}$$

$$\exp(-\beta f_i) = \int d\xi \exp[-\beta w_j(\xi)] P(\xi) \quad \textbf{[2-8]}$$

The β denotes the inverse temperature $1/k_B T$, with the Boltzmann constant k_B and the temperature T, n_j is the number of data points in the histogram h_j. The statistical inefficiency g_i is given by $g_i = 1 + 2\tau_i$, with the integrated autocorrelation time of τ_i of umbrella window i. The $P(\xi)$ denotes the unbiased probability distribution related to the PMF by equation 2-9, the ξ_0 is the reference point where $W(\xi_0)$ is set to zero. The WHAM equations 2-7 and 2-8 contain the free energy constant f_i and the unbiased distribution $P(\xi)$ which must be solved iteratively. For the derivations of the equations see reference (152)

$$W(\xi) = -\beta^{-1} \ln[\frac{P(\xi)}{P(\xi_0)}] \quad \textbf{[2-9]}$$

2.2 Methods

2.2.1 Receptor preparation

Throughout the following chapters I will concentrate upon 2 GPCRs, namely the δ-Opioid (δ-OR) and the m2 muscarinic receptors (M2R). The δ-OR and M2R simulation systems were constructed using the inactive state crystal structures (PDB: 4N6H and 3UON, respectively (65, 153)). Extraneous subunits added to the receptor to aid in the crystallisation process were removed. However, as is common in the crystallisation of GPCRs, this subunit was inserted in place of the intracellular loop 3 (ICL 3) in the M2R, I therefore reconnected the cleaved ICL 3 loop using Modeller v9.14 (154). In both systems, all external water and lipid molecules were removed, whilst all internal molecules were retained (except for the antagonists). After all extraneous material was removed, the charged N- and C- termini were neutralised using acetyl and methyl moieties, respectively. The receptors were simulated with default protonation states, including a negatively charged $D^{3.49}$ and $D^{2.50}$ unless otherwise mentioned. The δ-OR mutants $N131^{3.35}V$ and $N131^{3.35}A$ used in Chapters 3 and 5 were generated from the previously described δ-OR system.

To study the active state of the M2R in Chapter 4, I used a different approach to generate the system: I first parameterised the agonist carbachol using the AMBER16 software suite, GAFF2 atom types and the AM1-BCC charge model (155). The agonist carbachol was then docked into the orthosteric ligand-binding site

of the previously described inactive M2R using GOLD (v5.2.2). As I wished to study the role of Na^+ in the active M2R a Na^+ ion was placed within the Na^+ binding site in the inactive M2R structure. A targeted MD approach using the RMSD of the active receptor backbone (PDB: 4MQT (131)) as a reference. To enforce the transition from the inactive (PDB: 3UON) to the active state, position restraints of 50 kJ mol^{-1} nm^{-2} were applied to the Cα atoms within the transmembrane domain, this system was then further equilibrated for a total of ~250 ns. To help keep the receptor in an active conformation despite the absence of G-protein, I applied a minimal set of four distance restraints to the Cα atoms of the terminal groups of TM helices 2,5,6 and 7, namely residues 2.39-6.33, 2.39-5.61, 2.43-7.54 and 6.36-7.54, at this interaction site (Figure 2-4). In the active M2R simulations, two major conformations of $Y440^{7.53}$ were observed during the simulation. These were probed systematically in the PMF calculations using distance restraints between $N^{1.50}$-C_α and $D^{2.50}$-C_α to $Y^{7.53}$-C_ζ or dihedral restraints on the sidechain of $Y^{7.53}$.

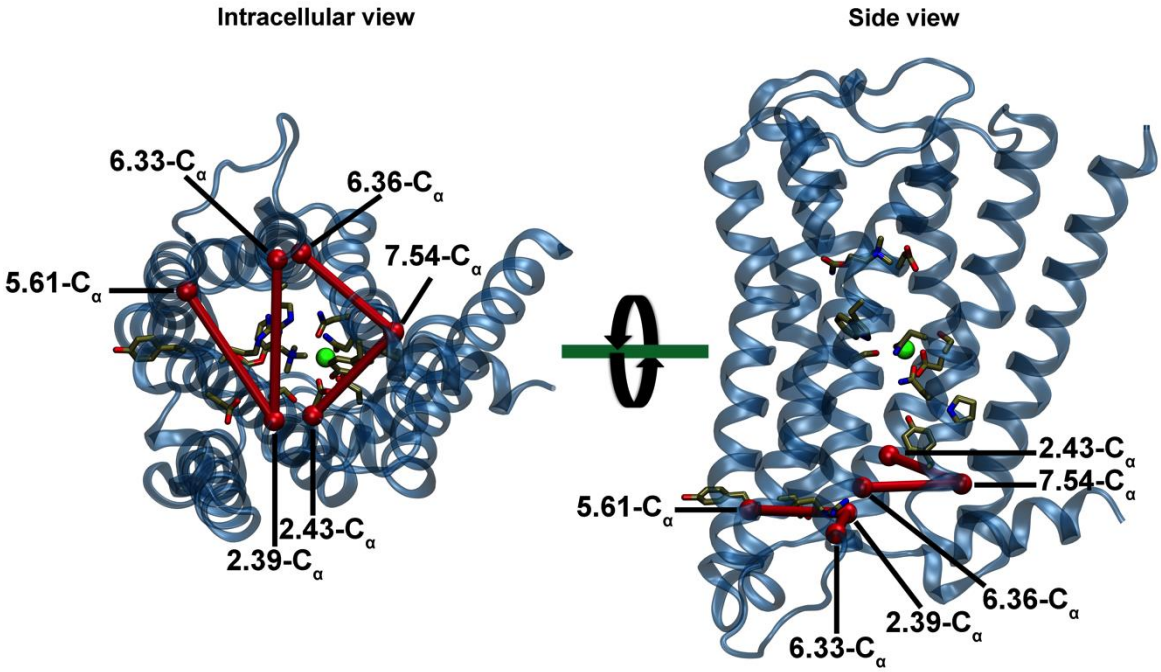

Figure 2-4: Minimal set of distance restraints used to maintain the active conformation of the M2R
A set of four distance restraints (shown by red bars) was applied to the intracellular portion of the transmembrane helices as described above. This procedure serves to maintain the M2R in an active state despite the absence of a bound G-protein. With bound Na^+ at the negatively charged $D^{2.50}$, the receptor regains its inactive conformation on time-scales below microseconds in most simulations without these restraints, which is agreement with the role of sodium as stabilizer of the inactive conformation. Figure adapted from (156).

2.2.2 Simulation setup

Each of the aforementioned receptors was inserted into a fully equilibrated and hydrated 1,2-palmitoyl-oleoyl-sn-glycero-3-phosphocholine (POPC) lipid bilayer using the GROMACS utility g_membed (157). The single bilayer simulation box is approximately ~92 x 88 x 97 $Å^3$. A NaCl concentration of 145 mM

was used in the aqueous solution in the single bilayer systems. For the initial equilibration, all protein heavy atoms were position restrained with a force constant of 1,000 kJ mol^{-1} nm^{-2} was applied for 5-10 ns. In contrast to the δ-OR crystal structure, the M2R crystal structure was resolved at a much lower resolution and showed minimal hydration. Therefore the system was equilibrated for a further 100 ns without restraints to enable full hydration.

2.2.3 CompEL setup

For the CompEL simulations, the aforementioned systems (see section 2.2.1) were duplicated along the z-axis to create a double membrane system. Charge imbalances of between one and four were used between aqueous compartments, generating a range of V_m from ~0 to 1,000 mV. For a 100x100x200 Å simulation box, a V_m of 250 mV was generated per each charge imbalance. The slightly supra-physiological V_m was used in order to accelerate voltage-induced effects to a computational timescale. The V_m was determined using the GROMACS utility g_potential using overlapping 2 ns windows with a 1 ns running average throughout the trajectories. For the work in Chapter 3 and 5, I used symmetric NaCl concentration in both compartments of 145 mM. For the work in Chapter 4, I included a physiologically relevant NaCl gradient of 150 mM: 10 mM between the extracellular and intracellular compartments.

2.2.4 Gating charge

I throughout this work, the focus was on the gating charge arising from cation movement from the allosteric binding pocket (ABS) and the bulk solution, therefore to minimise signal noise arising from the protein, position restraints of 1000 kJ mol^{-1} nm^{-2} were applied to the heavy atoms.

To scan Na^+ ion position effects upon the gating charges within the δ-OR and M2R, the Na^+ ion was restrained at 2.5 Å intervals along the z-axis from the ABS to the extracellular or intracellular bulk solution. Each position was simulated for 50ns with the first 5 ns discarded. For the M2R the Na^+ ion was positioned in the ABS identically to the δ-OR, coordinated by $D^{2.50}$ and $S^{3.39}$. Whilst for the wt δ-OR system, the positional restraints for the residue $N131^{3.35}$ was removed due to clashes with the Na^+ ion. The gating charges arising from the protonation state changes of $D69^{2.50}$, $D103^{3.32}$ and the extracellular bulk solution ($D173^{ECL2}$) within the M2R, were undertaken in a similar manner as with the Na^+ ion movement. The V_m was determined at each protonation state and the gating charge difference was calculated as per equation 3. For the calculation gating charges arising from the conformational change of the M2R transitioning from the inactive to active, I used the same protocol whereupon the V_m was determined for the inactive (PDB: 3UON (153)) and active crystal structure (PDB: 4MQT (131)). The system was equilibrated for 30ns before calculating the gating charge arising from the conformational change.

2.2.5 Forcefield parameters

For all simulations, the amber99sb_ildn force field was used for the protein (136), Berger parameters for lipids (138), which were adapted for use with the amber99sb force field (139), and the SPC/E or TIP3P model for water molecules (140). Water bond angles and distances were constrained by SETTLE (142) while all other bonds were constrained using the LINCS method (143). The temperature and pressure were kept constant throughout the simulations at 310 K and 1 bar, respectively, with the protein, lipids, and water/ions coupled individually to a temperature bath by the v-rescale method using a time constant of 0.2 ps and a semi-isotropic Berendsen barostat (145, 158). Employing a virtual site model for hydrogen atoms (144) allowed the use of 4-fs time steps during the simulation. All simulations were performed with the GROMACS software package, Chapter 3: Version 4.6 (159), Chapter 4 and 5: version 5.1.2 (160).

2.2.6 Potential of Mean Force

To calculate the potential of mean force (PMFs) in Chapter 3 for the movement of the Na^+ ion within the ABS through to the orthosteric pocket at neutral V_m, umbrella sampling was utilised in conjunction with the GROMACS utility g_wham (161). Bins of < 0.5 Å were used with simulation time of >150ns for each umbrella window. To record the PMF of ion movement within the pocket of the M2R, the system was first simulated under a hyperpolarised V_m until a Na^+ ion had relocated to the ABS. The error bars of the PMF profiles was were derived by using the Bayesian bootstrap method with 200 runs. The free energy minima of the Na^+ ion within the wt, $N131^{3.35}V$ δ-OR and M2R were set to G = 0 $kJmol^{-1}$. Throughout Chapter 3, the position of the Na^+ ion (z-coordinate) is reported relative to the $D^{2.50}$-Cα atom of the respective receptor.

To calculate the PMFs in Chapter 4 for the movement of the Na^+ ion within the hydrophilic pocket through to the intracellular solution at neutral V_m, umbrella sampling calculations were performed in bins of 0.25Å and analysed with the GROMACS utility gmx wham. I used a simulation time of 50ns in each window and harmonic potentials of 900–2000 kJ mol^{-1} nm^{-2} to restrain the Na^+ ion in the z-direction. The standard deviation of the PMF profiles was estimated by using the Bayesian bootstrap method, as implemented in gmx wham, with 200 runs. The free energy of the Na^+ ion in bulk solution was set to 0. The position of the Na^+ ion (Z-coordinate) is reported relative to the $D103^{3.32}$-C_α atom (ligand binding site).

To calculate the voltage induced tilt of the PMFs. The gating charges calculated for each position along the receptor was taken as a direct measure of the shape of the underlying voltage drop. The energy supplied by the voltage drop can be derived from Mitchells equation (Eq. 2-10).

$$\Delta G = zFV + RT ln\left(\frac{[X]_{out}}{[X]_{in}}\right) \qquad \textbf{[2-10]}$$

Where the ΔG is the free energy supplied, z is the charge of the ion species, F is Faraday's constant, V is the transmembrane voltage, R is the gas constant, T is the temperature, $[X]_{out}$ is the concentration of ionic

species in the extracellular solution and $[X]_{in}$ is the concentration of ionic species in the intracellular solution. The resulting energy is multiplied by *e* with a linear interpretation between points, was added to the PMF obtained from the umbrella sampling, in order to illustrate the effects of V_m upon the energetics of the Na^+ ion within the receptor.

2.2.7 pK_a calculations

The pK_a calculations in Chapter 4 were undertaken by Ms Catarina A. Carvalheda. These were performed on the basis of simulation snapshots taken at 2 ns intervals (between 10 and 20ns) from each umbrella windows (see section 2.2.6). The pK_a calculations were performed using a continuum electrostatics method, namely the Poisson-Boltzmann/Monte Carlo (PB/MC) approach. PB calculations were performed using MEAD (version 2.2.9)(162) with a dielectric constant (ε_p) of 4 for the protein and 80 for the solvent (ε_w), in the presence of an explicit membrane. The temperature was set to 310 K and the ionic strength to 0.145 M. The same temperature was used for MC calculations (10^3 steps in each calculation), which were performed using MCRP (163). Each MC step consisted of a cycle of random choices of a state for all individual sites and pairs of sites with couplings above 2.0 pK_a units (163), whose acceptance/rejection followed a Metropolis criterion (164). Tautomeric forms were not included.

Chapter 3. Putative voltage sensor in class A GPCRs

3.1 Introduction

Transmembrane voltage (V_m) is a fundamental property of all membranes, generated by electrochemical ion gradients across semi-impermeable lipid bilayer (122). As the V_m drops across a thin hydrophobic core of the membrane, < 30 Å thick along the membrane normal, extremely strong electric fields of up to 10^7-10^8 Vm^{-1} exist (165). Whilst extensive work has been done on the effects of V_m upon ion channels in particular voltage-gated ion channels, the effect of V_m upon the function of other membrane proteins has been given little thought.

3.1.1 GPCR voltage sensitivity

As discussed within Chapter one, GPCRs form the largest group of integral membrane proteins in the human genome (4). It has been shown that the modulation of V_m within the physiological range elicits functional and conformational changes in several GPCRs and families: muscarinic, dopamine, adrenoceptor, glutamate, 5-HT and P2Y (112–117, 166, 167). Of particular interest, voltage-induced rearrangement of charges (gating currents) were uncovered by electrophysiological recordings of the α_{2A} adrenergic, m1 and m2 muscarinic receptors (M1R and M2R), from these experiments, evidence of a gating charge of ~0.5 - 0.85 were obtained (Table 3-1, Figure 3-1) (112, 113, 126, 168). Most of these measurements converge to a gating charge of near 0.55 e (125).

Receptor	Gating charge (e)	Reporter method	Ref
m1 muscarinic:			
wt	0.72	FRET	(112)
	0.76	FRET	(112)
m2 muscarinic:			
wt	0.55	Electrophysiology	(126)
wt	0.7	Electrophysiology	(118)
wt	0.85	Electrophysiology	(118)
$D69^{2.50}A$	Not resolved	Electrophysiology	(126)
$W99^{3.28}A$	0.8	Electrophysiology	(126)
$D103^{3.32}A$	0.5	Electrophysiology	(126)
$Y104^{3.33}A$	0.54	Electrophysiology	(126)
$S107^{3.36}A$	0.49	Electrophysiology	(126)
$D120^{3.49}N$	0.66	Electrophysiology	(118)
$D120^{3.49}N$-$R121^{3.50}N$	Not resolved	Electrophysiology	(118)
$D120^{3.49}N$-$R121^{3.50}N$	0.52	Electrophysiology	(126)
$Y403^{6.51}A$	0.57	Electrophysiology	(126)
α_{2a}-Adrenergic:			
wt	0.5	Electrophysiology	(113)

Table 3-1: Gating charges reported for the *Rhodopsin* GPCR family

This table shows all previously reported gating charges for the M1, M2 muscarinic receptor and the α_{2a}-Adrenergic receptor.

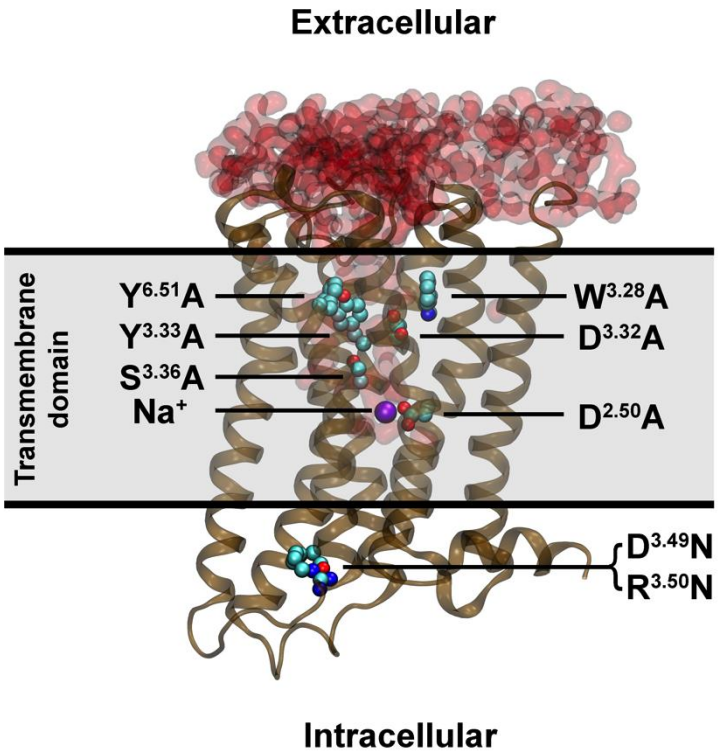

Figure 3-1: Experimental mutations of the M2R to elucidate the origin of the gating charges
All mutated M2R residues that were listed in Table 1, probing the origin of voltage sensor are shown in cyan. Mutation of these residues was shown to have no effect upon the measured gating charges with the exception of $D^{2.50}$. Water molecules are depicted as red surface and the allosteric Na^+ ion as a purple sphere.

3.1.2 Chapter overview

Throughout this chapter, I will address the structural and functional consequences of V_m upon two GPCRs via atomistic molecular dynamics (MD) employing state of the art computational techniques. I first chose to investigate the δ-Opioid receptor, due to the availability of a high quality crystal structure, its clinical importance and its distribution within the nervous system. The δ-OR is predominantly expressed within neurons in the brain and in the dorsal root ganglion, where it is frequently exposed to rapid and extreme changes to V_m (120, 170, 171). In addition, I included the m2 muscarinic receptor, on which the majority of experimental measurements of charge rearrangements were performed (118, 126).

Here, I will demonstrate that the allosteric Na^+ ion is the most mobile charge within the TM domain of the *Rhodopsin* family, and sensitive to alterations in V_m. The coordination pattern of the Na^+ ion within the hydrophilic pocket depends strongly on the V_m. Additionly; the voltage induced transition of the Na^+ ion generates a gating charge in excellent agreement with the previous experimentally obtained values. It is possible for other cations to bind within the hydrophilic pocket, thereby replacing the Na^+ ion (100, 101). The large scale transitions of the receptor from inactive to active as derived from the crystal structures of the M2R, gives rise to gating charges far smaller than the experimental observations. The data suggests that the movement of a single charge from the ABS through the hydrophilic pocket is the most plausible mechanism to explain the experimentally obtained gating currents.

3.2 Results

3.2.1 Voltage-induced mobility of the allosteric Na^+ ion

A series of atomistic simulations were conducted using the computational electrophysiology (CompEL) protocol (146) on the wt and mutant δ-OR with a depolarised V_m, with a total simulation time of >30 μs (Table 3-2). By applying a Na^+ electrochemical gradient (1-4 ions) across the membrane, evoking a V_m between -1000 mV and 1000 mV in 250mV increments, the amplitude of the V_m enables us to accelerate any effects that might be missed due to the limited simulation timescale. Due to its conservation as an ionisable residue and its close interaction with a Na^+ ion within the crystal structure, the side chain of the $D95^{2.50}$ was modeled in the negatively charged protonation state. Furthermore, I found that the protonation and therefore the neutralisation of the $D95^{2.50}$ sidechain abolished the affinity of the ABS for the Na^+ ion, even under 0 mV, such that the ion can spontaneously dissociate in very short timescales. The protonation of $D^{2.50}$ is therefore incompatible with the crystallographically observed Na^+ ion in the inactive receptor conformation.

Receptor	Ion imbalance (1 ion = ~ 250mV)				
	0	1	2	3	4
δ-OR wt	3x	1x	5x	8x	4x
δ-OR $N131^{3.35}A$	2x	1x	1x	1x	1x
δ-OR $N131^{3.35}V$	2x	1x	2x	1x	1x
δ-OR $D95^{2.50}A$	1x	1x	—	—	—
M2R wt	2x	4x	4x	—	10x

Table 3-2: Simulation conditions specifying the ionic imbalances and replicates.
A complete list of simulations run, displaying the number of repeats and ionic imbalances used on the wt M2R, wt δ-OR and the three δ-OR mutants: $N131^{3.35}A$, $N131^{3.35}V$ and $D95^{2.50}A$. Note that at each ion imbalance, both hyper- and depolarised receptors are simulated simultaneously (see section 2.1.2).

The simulations under V_m show that the coordination of the Na^+ ion in the δ-OR receptor is strongly influenced by the electric field. In the case of the wt δ-OR, when the depolarised V_m exceeds 700 mV the Na^+ ion is expelled from the ABS in the core of the receptor, and moves to a conserved aspartate ($D128^{3.32}$) within the orthosteric ligand binding site (Figure 3-2 A, B). At this site, the Na^+ ion is coordinated by the side chains of $D128^{3.32}$, $N131^{3.35}$, and the backbone of $D128^{3.32}$; this binding site is extended further towards the orthosteric site, where the Na^+ ion predominantly coordinates with the side chain oxygen atoms of $D128^{3.32}$. From this transient binding site (TBS), the Na^+ ion can either leave the receptor completely and enter the extracellular space, or reenter the ABS. Within simulations under neutral or negative V_m, no movement of the Na^+ ion to the extracellular space is recorded (Figure 3-3).

In experiments undertaken by Fenalti *et al*, the δ-OR mutant N131$^{3.35}$V decreases the allosteric effect, and lowers the Na^+ dependence of δ-OR agonists, whilst retaining a low binding affinity (77 mM) in contrast to the wt (13.3mM)(65). Therefore, I mutated the position N131$^{3.35}$ to a Valine to study the effects of a hydrophobic residue upon the voltage-induced movements of the Na^+ ion. The position 3.35 is the only residue within the 15 residues of the hydrophilic pocket, which is not highly conserved, with the residue evenly split between hydrophilic and hydrophobic residues across all of the *Rhodopsin* family (68).

The simulations of the N131$^{3.35}$V mutant demonstrate a much higher sensitivity of V_m upon the Na^+ ion. In contrast to the wt, the Na^+ ion can be transiently displaced from the ABS by V_m above ~250mV in the mutant. Whilst voltages of >500mV are able to remove the Na^+ ion from the ABS in under 0.1μs, as with the wt, the V_m induced movements of the Na^+ ion leads to the coordination of the Na^+ ion to D128$^{3.32}$ within the TBS. Interestingly, my simulations also show that the mutation of N131$^{3.35}$ destabilises the Na^+ binding site, this is revealed as a second binding site 2 Å deeper within the ABS than the crystallographic binding site (z = 0Å)(Figure 3-2 C). In all simulations, the translocation of the Na^+ between the ABS and TBS follows a highly similar pathway, in contrast to the exit to the extracellular space, where multiple pathways are sampled. The exit pathways seen throughout our simulations, follows that of previously published simulations using randomly accelerated MD (aMD) which was used force the exit of Na^+ without the application of V_m (172).

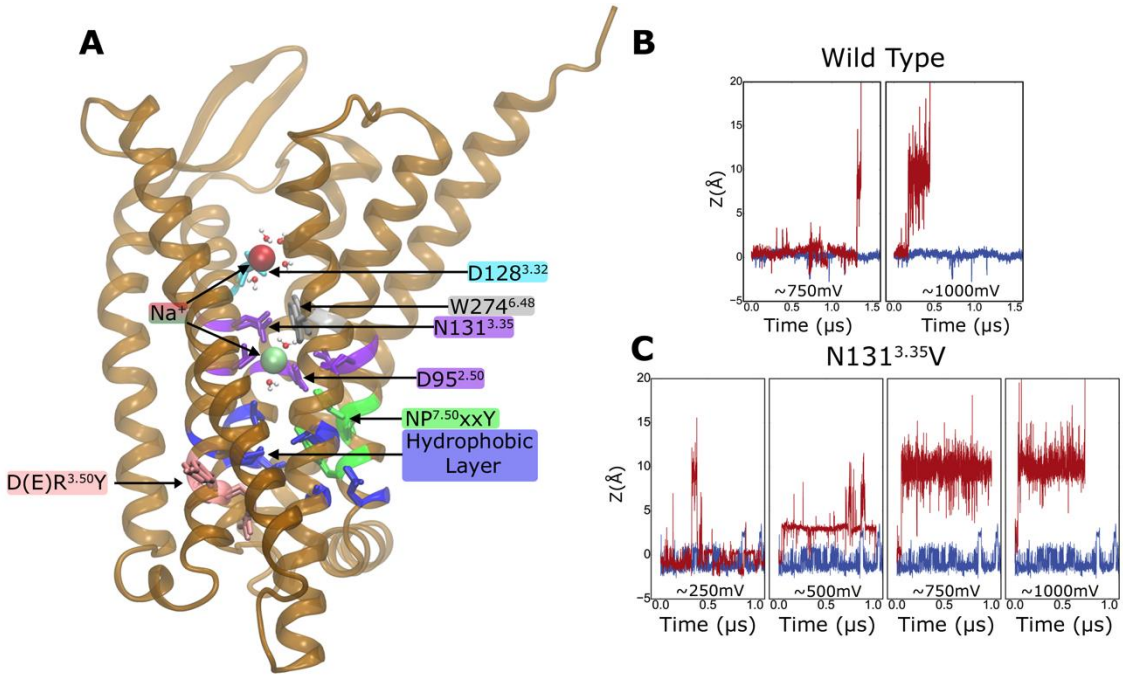

Figure 3-2: Effect of depolarized V_m on the position of the Na^+ ion in δ-OR

(A) Structure of the δ-OR depicting Na^+ bound in the allosteric (green) and orthosteric binding sites (red). The binding sites correspond to coordinates of z = 0 Å and z = ~9 Å in the graphs shown in **(B)** and **(C)**, respectively. **(B and C)** Z-coordinate of the internal Na+ ion in wt δ-OR **(B)** and in the N131$^{3.35}$V mutant **(C)** under depolarized V_m, displaying translocation of the Na^+ ion induced by V_m (depolarized V_m simulations, red trace; 0 mV control, blue trace). The approximate V_m at the time of the transitions is noted in the graphs. Key functionally important residues are shown as sticks and color-coded into the groups:

D(Glu)Arg$^{3.50}$Y motif (pink), hydrophobic layer (blue), NP$^{7.50}$xxY motif (green), allosteric Na^+ binding pocket (magenta), ‘‘toggle switch’’ residue Trp274$^{6.48}$ (silver), Na^+ binding site in the orthosteric pocket (cyan). Figure adapted from (70).

Throughout the simulations, the allosteric Na^+ ion remains bound within the ABS for the duration of the simulation under negative or no V_m. Upon the application of hyperpolarised potentials (-250 to -500 mV), the Na^+ ion is transiently attracted deeper into the hydrophilic pocket to the secondary binding site in the wt δ-OR (Figure 3-3 C), whilst the N131$^{3.35}$V becomes stabilised in the second binding site (Figure 3-3, Figure 3-2 D). Curiously, under a large hyperpolarised potential (-1000 mV), a second Na^+ ion is observed to enter the hydrophilic pocket, Figure 3-3 E-G shows the concurrent occupation of the two binding sites over substantial timespans within the wt δ-OR.

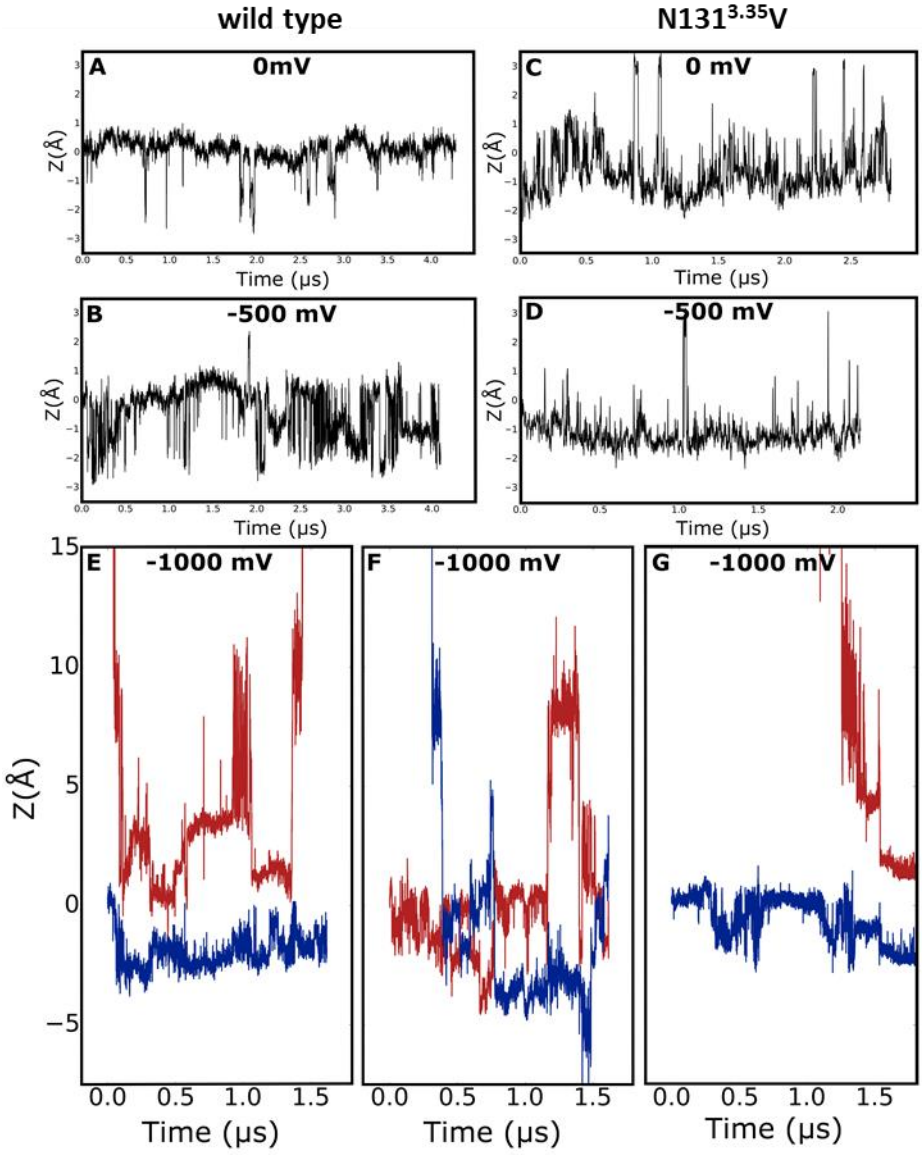

Figure 3-3: The binding of Na^+ ion at the ABS under neutral or negative transmembrane potentials

Z-coordinate of the allosteric Na^+ ion, in the wt δ-OR **(A)** and $N131^{3.35}V$ δ-OR **(C)** under no transmembrane voltage as a control. The wt δ-OR shows stable coordination of the Na^+ ion within the major allosteric Na^+ binding site, with minor transient fluctuations into the secondary allosteric Na^+ binding site. In the $N131^{3.35}V$ δ-OR mutant, the Na^+ ion primarily occupies the major energy minima shown in Figure 3-4B, with some minor fluctuations within the pocket. Under a hyperpolarised V_m of -500mV the allosteric Na^+ ion within the wt δ-OR **(B)** shows multiple transitions between the major binding site and the secondary allosteric Na^+ binding site. In the $N131^{3.35}V$ δ-OR **(D)** mutant the Na^+ ion primarily occupies the major energy minima shown in Figure 3-4, however is predominantly situated deeper within the hydrophilic pocket with minor upward fluctuations. **(E-G)** Shows 3 replicates of the wt δ-OR under strongly hyperpolarised V_m of -1000 mV, demonstrating that the inner hydrophilic pocket can bind two ions simultaneously. The original Na^+ ion predominantly resides within the secondary allosteric Na^+ binding site (blue trace) and is coordinated by the side chains of $N310^{7.45}$, $N314^{7.49}$ $D95^{2.50}$ and the $L91^{2.46}$ backbone. This provides enough space for the major binding site to be occupied by a second Na^+ ion (red trace), coordinated by the sidechains of $N131^{3.35}$, $S135^{3.39}$ and $D95^{2.50}$. The dual occupation with Na^+ persists for the majority of the simulation time. In these simulations, the second Na^+ ion can either exit the hydrophilic pocket to the extracellular side **(E)** or can switch positions with the original allosteric Na^+ ion **(F)**. Figure adapted from (70).

3.2.2 Energetics of Na^+ ion movement within the hydrophilic pocket

The initial simulations under supra-physiological levels of depolarisation consistently result in the expulsion of Na^+ ions from the hydrophilic pocket to the orthosteric site on a sub micro-second timescale, I next investigated whether physiological or experimental V_m is sufficient to drive Na^+ translocation. I therefore quantified the equilibrium free energy barrier for the transition of the by recording a potential of mean force (PMF) of Na^+ along the z-axis, using umbrella sampling in the absence of V_m.

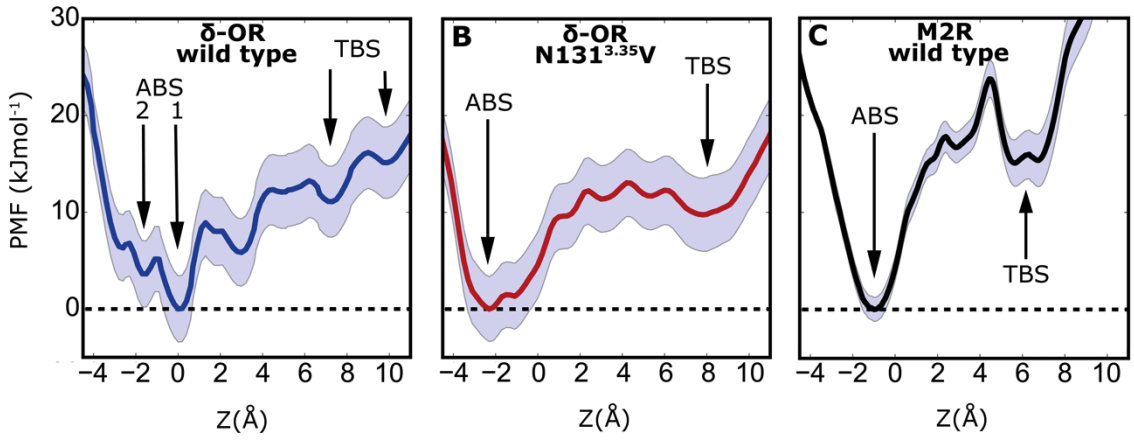

Figure 3-4: Potential-of-mean-force profiles of Na^+ translocation in the hydrophilic pocket of wt δ-OR, $N131^{3.35}V$ δ-OR, and wt M2R

(A–C) Equilibrium potential of mean force (PMF) of Na^+ translocation along the TM axis in wt δ-OR **(A)**, the $N131^{3.35}V$ mutant **(B)**, and the M2R **(C)**. Arrows highlight key binding sites; the SD obtained from bootstrap analysis is depicted as light-blue shading. The observed energy barriers for movement of a Na^+ ion within the hydrophilic pocket are low, and in the range of the energy provided by physiological and experimental membrane voltages. ABS, allosteric binding site; TBS, transient binding site. Figure adapted from (70).

The PMF for the wt δ-OR reveals a total free energy barrier of 13 ± 2.5 kJ mol^{-1} for the transition between ABS and TBS (Figure 3-4 A). The PMF also highlights 2 energy minima, the major of which corresponds to that of the Na^+ binding site defined by the δ-OR crystal structure (65), with the Na^+ ion coordinated predominantly by $N131^{3.35}$, $S135^{3.39}$ and $D95^{2.50}$ (z = 0 Å). The second energy minimum at the base of the pocket is located towards the intracellular side (z = ~-1.6 Å), where the ion is mainly coordinated by $N310^{7.45}$, $N314^{7.49}$, $D95^{2.50}$ and the $Leu91^{2.46}$ backbone (Figure 3-4 A). The energy barrier separating these two minima is 5.3 ± 2.5 $kJmol^{-1}$. The presence of the transient binding site shown in the previous simulations is reflected in local energy minima near z = 7 and 10 Å. The major energy barrier for the movement between the ABS and TBS arises form a constriction passage between the sidechains of $N131^{3.35}$ and $W274^{6.48}$. This is reflected in the energy barrier of ~9 ± 2.5 $kJmol^{-1}$ confining the Na^+ ion to the crystallographic binding site in the extracellular direction. This barrier corresponds to a rotation of the sidechain of $N131^{3.35}$ towards the orthosteric ligand-binding pocket, which is required for the efficient transfer of the Na^+ ion.

Curiously, the PMF of the $N131^{3.35}V$ mutant displays a similar free energy barrier for the passage of the Na^+ ion from the ABS to the TBS of 13 ± 2.5 $kJmol^{-1}$. In contrast to the wt δ-OR, the free energy barrier of the wider and smoother (Figure 3-4 B), reflecting the formation of a hydrophobic gate separating the ABS and TBS in the $N131^{3.35}V$ mutant. The PMF also shows a merging of the 2 energy minima shown in the wt δ-OR, with a rough outline of the 2 binding sites displayed in the PMF, and the most preferred binding site now located deeper within the hydrophilic pocket (z = ~-2.2 Å). The $N131^{3.35}V$ mutation increases the movement of the Na^+ within the hydrophilic pocket, leading to an increased fluctuation of the Na^+ ion under no V_m (Figure 3-3 C).

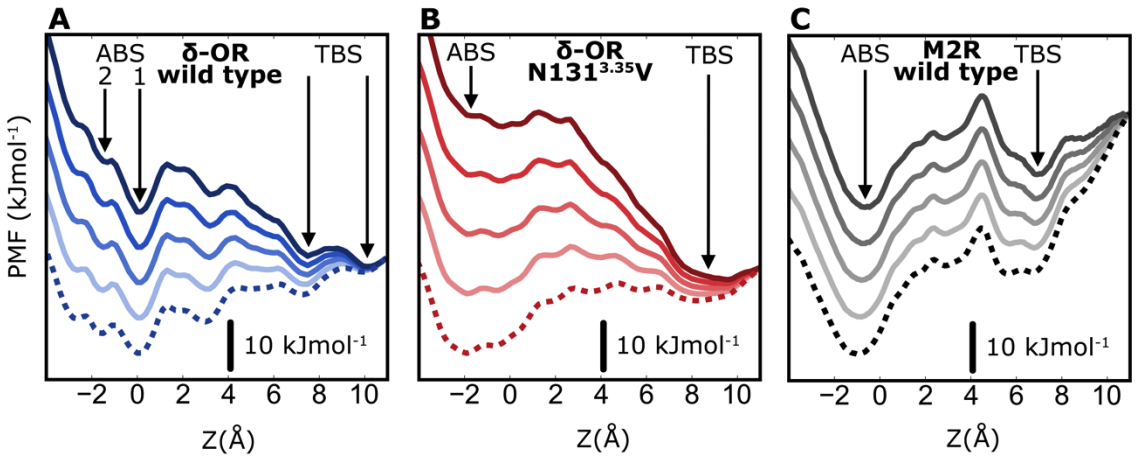

Figure 3-5: Non-equilibrium effect of V_m on the PMF profiles of Na^+ translocation within the internal pocket

(A–C) Voltage-induced tilt of the free energy surface of Na^+ in the non-equilibrium case in wt δ-OR **(A)**, the N131$^{3.35}$V mutant **(B)**, and the M2R **(C)**. Increments are from 250 mV (light) to 1,000 mV (dark); dotted line indicates 0 mV. The underlying voltage drop was mapped by using the gating charge calculations displayed in Figure 3-10. The energy supplied by the voltage drop is multiplied by the gating charge e, and overlaid over the equilibrium PMF (Figure 3-4). The removal of kinetic traps on the pathway of the ion in the N131$^{3.35}$V mutant becomes evident from the smoother surfaces in **(B)**. Note that the graphs display relative energy differences for each voltage regime rather than absolute energy values. The black bar therefore denotes an energy difference of 10 kJ mol^{-1} within each curve, and the offset between the curves has been arbitrarily selected. ABS, allosteric binding site; TBS, transient binding site. Figure adapted from (70).

The analysis of the δ-OR PMFs show that the binding of Na^+ to the TBS in the orthosteric binding site is only 11 kJmol^{-1} higher in energy than the binding within the ABS in the case of the wt, and ~ 10 kJmol^{-1} in the N131$^{3.35}$V mutant. Of particular importance, the movement of the Na^+ ion within the hydrophilic pocket (~6 Å) in both the wt and mutant δ-OR experiences energy barriers of <10 kJmol^{-1}, whilst the complete removal of the Na^+ ion from the hydrophilic pocket would require surmounting only a small additional activation barrier of ~3 kJmol^{-1}. For comparison, the potential energy of a monovalent cation in a voltage gradient of ~100 mV amounts to ~10 kJmol^{-1} (see section 2.2.6). This demonstrates that V_m within a physiological range can provide sufficient energy to alter the position of the Na^+ ion over substantial distances within the pocket, and to relocate the Na^+ between the ABS and TBS.

The N131$^{3.35}$V mutation removed the steep barriers within the free energy landscape, leading to gentler slopes, which kinetically facilitates the movement of the Na^+ ion. Similar to the effects reported for ion permeation through the Ca^{2+} release activated Ca^{2+} (CRAC) channel (173), the smoother energy landscape within the N131$^{3.35}$V mutant δ-OR arises from a increased hydration of the of the hydrophilic pocket of 13 to 18 waters molecules, this consequently raises the hydration level of the migrating Na^+ ion (Figure 3-6). The ruggedness of the free energy landscape has important consequences for the rate of transitions, in the case of non-equilibrium cases, such as the application of V_m. Both the roughness of the energy surface and steepness of the free energy barriers contribute to the formation of kinetic traps upon the tilting of the

energy surface, arising from the voltage drop across the membrane (174, 175). The effect of the voltage drop felt by the Na^+ ion along the z-axis of the hydrated pocket in a range of V_m between 250-1000 mV was applied to the equilibrium free energy landscape (Figure 3-5). The detailed shape of the voltage gradient inside the pocket was derived from the gating charge calculations of the Na^+ ion movement across the z-axis (see section: 3.2.3). The depolarisation of the membrane results in major changes in the free energy surface in the pocket, with the TBS becoming the global energy minima in all studied receptors. The findings also show that the N131$^{3.35}$V δ-OR mutation accelerates the outward migration of the Na^+ ion by the smoothing and removal of the kinetic traps present in the wt, despite the main equilibrium energy barrier being similar.

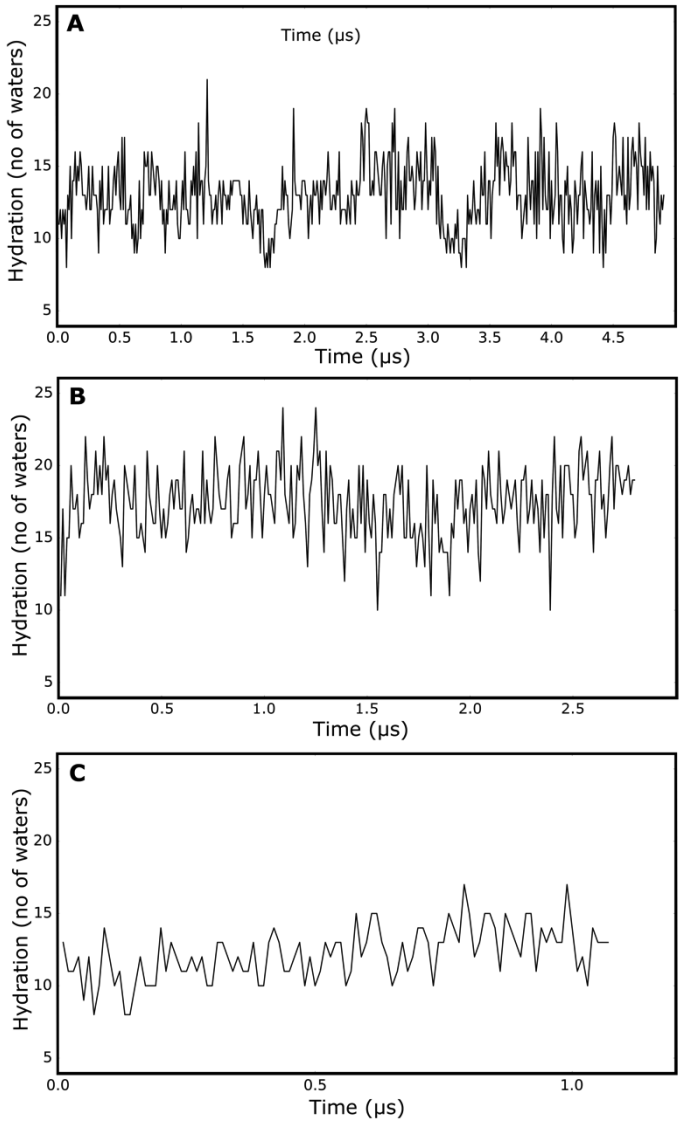

Figure 3-6: Hydration of the hydrophilic pocket

The number of water molecules within the hydrophilic pocket shows stable hydration levels over microsecond time-scale simulations. A similar mean hydration level is observed between wt δ-OR **(A)** and M2R **(C)** of 13.0 ± 2.2 and 12.2 ± 1.8 respectively. The N131$^{3.35}$V mutation leads to a slightly increased hydration level of 17.4 ± 2.4 water molecules in the pocket. The number of water molecules was determined

every 10ns from simulations at 0 mV between limits defined by the atoms $Y^{7.53}$-Cα and $D^{3.32}$-Cα (± sd). Figure adapted from (70).

Whilst most emphasis was put upon the internally bound Na^+ ion, it is important to note that throughout all of the simulation, I see continuous binding and dissociation events of the Na^+ ions to the TBS on the simulation timescale, regardless of V_m. However, the passage of these Na^+ ions occurs on a multitude of different pathways, precluding a single collective coordinate representation of the PMF, which was a suitable description for the transition pathway from the ABS to TBS, which displayed a single pathway along the Z-axis (Figure 3-7).
Whilst no experimental data is available for gating charges in the δ-OR, I therefore next focused on the M2R where evidence for the effects of V_m has been previously been studied and gating charges have been obtained by voltage clamp recording (Table 3-1).

In comparison to the δ-OR I used a subtly different protocol on the M2R due to the lower resolution of the crystal structure (3.0 Å), precluding the detection of Na^+ within the ABS. Despite the resolution deficiencies of the crystal structure, the presence of Na^+ has been inferred based on the conservation of the hydrophilic pocket and functional considerations (68). Additionally, Na^+ ions have been shown previously to bind spontaneously from the extracellular environment in MD simulations (176, 177). Also, the hydration level of the M2R in comparison to the δ-OR receptor is much lower, however additional water molecules are able to enter the hydrophilic pocket on a timescale of nanoseconds. I therefore initially simulated the M2R until the pocket was fully hydrated and attracted the Na^+ ion to the ABS by using a hyperpolarised potential. I then calculated the PMF for the observed pathway. As Figure 3-7 shows, the inward transition pathway is highly similar to the outward pathway of the Na^+ ion in the δ-OR.

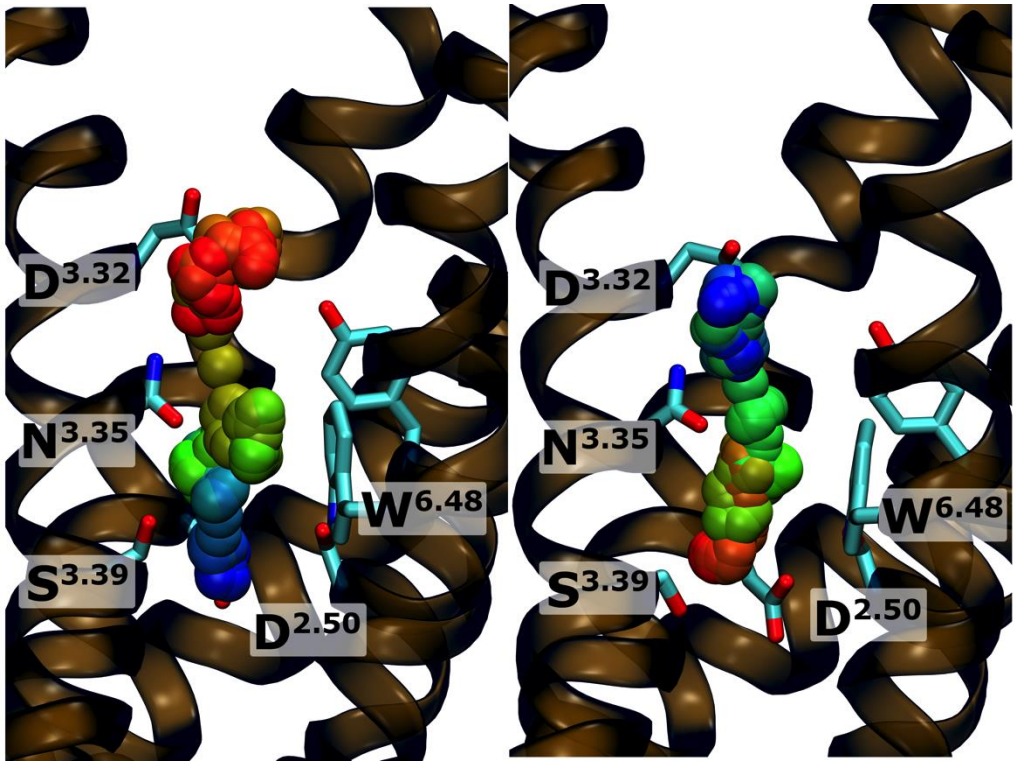

Figure 3-7: Comparison of inward and outward pathways of Na^+

Pathways taken by the Na^+ ion from the transient binding site to the allosteric binding site **(left)** or from the allosteric binding site to the transient binding site **(right)** in the wt δ-OR (color-coded according to simulation time proceeding from red to blue). In both directions, the Na^+ ion passes centrally between $N131^{3.35}$ and $Trp274^{6.48}$, where it is coordinated by the oxygen atom from the $N131^{3.35}$ sidechain and a cation-π interaction between the ion and the aromatic sidechain of $Trp274^{6.48}$. Figure adapted from (70).

The PMF of the Na^+ ion transition from the ABS to the TBS in the M2R shows a clearer distinction between binding sites. The free energy barrier between the ABS and TBS is present slightly higher in the receptor at the same height as $I72^{2.53}$ at ~26 ± 2.5 kJmol^{-1}. This higher free energy barrier was attributed to a tighter hydrophobic gate surrounding the transition pathway of the Na^+ ion by $I72^{2.53}$ ($A98^{2.53}$ in the δ-OR) approximately z = ~4.5 Å higher than $D69^{2.50}$. A minor energy well present at z = ~3 Å is due to the coordination with the stabilising residues: $S107^{3.36}$, $S433^{7.46}$ and $N432^{7.45}$.

Despite the higher free energy barrier of the M2R in comparison to the δ-OR, the energy difference between the ABS and TBS is comparable between the receptor subtypes (~15 kJmol^{-1}). Therefore, a comparable duality between the two ion binding sites of similar free energy exists for the M2R and δ-OR in the case of a depolarised V_m. The higher free energy barrier in the M2R would give rise to slightly higher activation energy under V_m for the transition between binding sites; however, despite this, the expected rates for overcoming a barrier of this size would still be rapid on a physiological timescale.

As previously mentioned, the caveats of using a lower resolution crystal structure of the M2R with respect to the δ-OR crystal structure, such as missing structural data (e.g. ICL3), might incur higher levels of inaccuracy in the M2R PMF. However, the PMF of the Na^+ ion in the M2R shows a remarkable similarity to the free energy profile of the $N131^{3.35}$V δ-OR mutant, with a mild deviation in shape at ~4.5 Å due to a greater constriction of the pathway. All three PMFs display similar energy minima at the binding sites

within the ABS between -2 and 0 Å, as well as at the TBS between 6 and 10 Å. These PMFs highlight the possibilities of similar free energy landscapes and binding sites being present in other *Rhodopsin* GPCR families.

3.2.3 Determination of gating charges

To further link the experimental and computational measurements, I characterised the movement of the Na^+ ion under the influence of V_m, by investigating the gating charges that arise from the movement of an ion between the base of the hydrophilic pocket to the top of the orthosteric binding site in the $N131^{3.35}V$, wt δ-OR, and M2R. I used a novel protocol to calculate gating charges in membrane proteins, which has been optimised and developed for use with CompEL double membrane simulations (151).

Briefly, the V_m obtained for a single insulated or double bilayer system under electrochemical gradient is a function of the charge imbalance in the bulk solutions on either side of the membrane (Δq_{bulk}) and charge imbalances within the membrane-immersed protein (Δq_{prot})(148). At a specific bulk charge imbalance, differences in V_m, averaged over time, therefore arise from a rearrangement of the charge distribution within the hydrophobic core of the membrane or protein embedded therein, corresponding to a measurable gating charge (Figure 3-8, see section 1.5.4)(148).

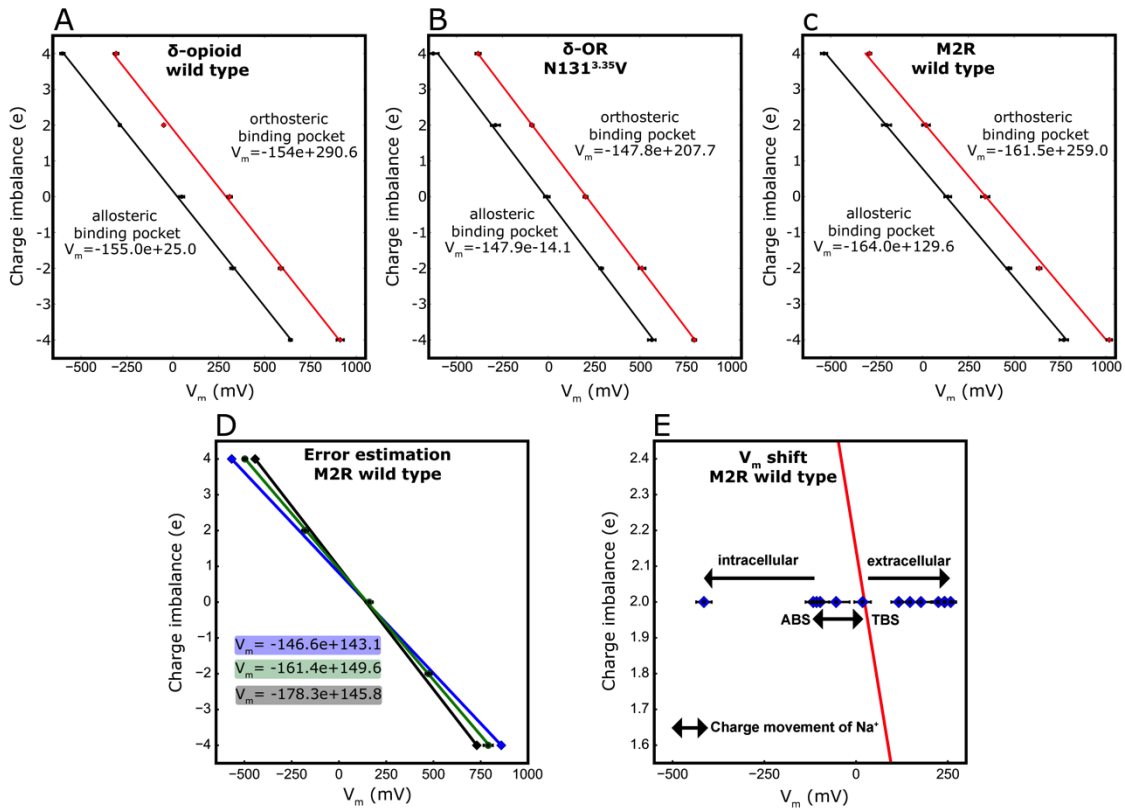

Figure 3-8: Relationship between transmembrane charge imbalance and V_m over a wide voltage range

The panels (**A-C**) shows membrane voltage plotted against charge imbalance, exhibiting a linear relationship. The slope of the curves denotes the capacitance, which is nearly identical in the two states of

the ion as can be seen. The voltage displays a right shift (black circles to red squares) due to the movement of the allosteric Na^+ ion from the hydrophilic pocket to the orthosteric ligand binding pocket and further into the extracellular space. The examples display the effect seen upon movement of a sodium ion from the allosteric site to the transient binding site in the orthosteric pocket. (**D**) Minimum and maximum capacitances, derived from the lowest and highest V_m and vice versa measured in the M2R. (**E**) V_m shift arising from the movement of Na^+ from the intracellular to extracellular solution. The movement is split into three major movements: Between the ABS and intracellular solution, the ABS and TBS and the TBS to the extracellular solution. The red line denotes the capacitance of the system with the Na^+ ion in the TBS as shown in panel **(C)**. The V_m fluctuations of the system were minimised by the application of position restraints in the x, y and z axes on the protein, and a position restraint of 200 kJ mol^{-1} nm^{-2} along the z-axis, on the bulk Na^+ to prevent ingress of an additional ion into the orthosteric ligand-binding pocket. In this way, the gating charge arising only from the movement of the allosteric Na^+ ion was recorded. The standard deviation of the variation of V_m falls between 8-30 mV using the above protocol for each data point on the graphs, as shown here by the horizontal error bars. Figure adapted from (70).

Figure 3-10 shows that the movement of the Na^+ ion from the ABS to the extracellular domain gives rise to a maximum gating charge of 0.42 ± 0.03 e, 0.63 ± 0.03 e and 0.53 ±0.02 e for the wt δ-OR, $N131^{3.35}V$ δ-OR and wt M2R respectively. It is worth noting, that in the wt δ-OR the residue $N131^{3.35}$ was unrestrained to prevent clashes with the Na^+ ion throughout the gating charge scan, upon the restraint of the side chain, a gating charge of ~0.6 was also calculated. For the transfer of the Na^+ between the ABS and TBS, my calculations predict gating charges of up to 0.3e, for all studied receptors. As shown in Table 3-1, the experimental gating charges of the M2R span between 0.5 to 0.85 e (118, 126), however, the majority of the experimental measurements on the wt and mutant M2R converge near ~0.5 e. For the α_{2A} adrenergic receptor, a gating charge of 0.5 e has also been reported (113). The gating charges measured in my simulations are therefore in excellent agreement with the gating charges measured in previously in the M2R and other GPCRs (112, 113, 126, 168).

The results demonstrate that the movement of a charge inside the GPCR must cover a substantial distance along the membrane normal to result in a gating charge near 0.5 e. More spatially restricted rearrangements of charged or polar groups are unlikely to explain such a large value for the gating charge. However, if many charged residues move simultaneously a larger gating charge could be recorded. Of note, even under a V_m of 1000 mV I did not observe extensive movement of any other charged or polar residues within the hydrophobic layer of the membrane.

To substantiate this notion, I then tested the maximum gating charge that would arise from the conformational change of inactive to active form, as this can be assumed to reflect the upper boundary of the conformational variability of the receptor (Figure 3-9). The M2R receptor has been crystallised in both the inactive and active conformations (131, 153). Despite the poor resolution of the structures and the use of a nanobody to stabilise the active state, the conformational change will encompass the pertinent movements. I used the same protocol as previously described, the transition from the inactive to active

conformations of the M2R leads to a gating charge of 0.13 ± 0.02 e (if the Na^+ movement is disregarded). This approach includes the entire protein in the transition, and therefore the conformational changes of the charged residues at the $DR^{3.50}Y$ motif, $E^{6.30}$ and $D^{3.32}$ are considered. The calculated gating charge for the inactive to active conformational change is thus too small to serve as an explanation for the experimentally observed values, unless the movement of the cation is included.

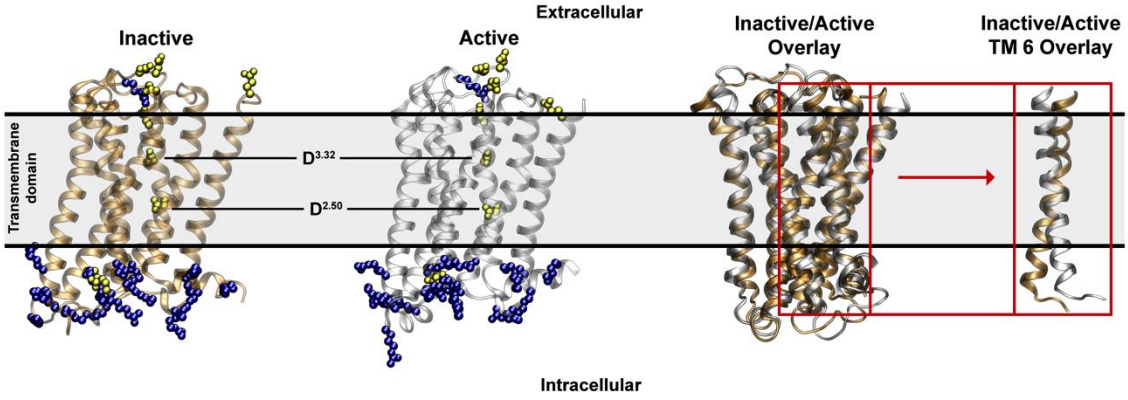

Figure 3-9: Maximal movement of charged protein residues upon the transition of M2R from the inactive to the activated conformation

(A) Conformational change of the M2R from the inactive state (left, brown) to the active state (right, silver), representing an upper limit to the known receptor conformational dynamics and the movement of charged residues. Charged residues are shown as spheres for clarity (positive, blue; negative, yellow). A small gating charge of only ~0.13e is linked to the activation transition of the receptor. (B) Comparison of the overall conformation of inactive (brown) and active M2R (silver; PDB: 3UON and 4MQT, respectively), TM 6 is shown separately for clarity.

Other charges, e.g. potassium and protons, however, can easily be imagined to undergo the same movements described for the crystallographic Na^+ ion, and would lead to an experimentally indistinguishable gating charge. I therefore tested the hypothesis that the movement of a proton along the same pathway through the hydrophilic pocket would give rise to the same gating charges. The ABS is formed by the ultra conserved $D^{2.50}$ located approximately within the center of transmembrane domain. The protonation state has been addressed in multiple studies, where its pK_a has been calculated to be ~7 (80, 178–180). The pK_a of ionisable groups within the hydrophobic layer of the membrane would be highly sensitive to changes in the V_m (181), thereby allowing changes in the V_m to modulate the protonation state of said residues. Unless a cation such as the Na^+ ion binds to $D^{2.50}$, it is easy to envisage this residue to become protonated, and due to its location within the membrane, to be highly sensitive to V_m. The orthosteric ligand-binding site contains a second ionisable side chain within the TBS ($D^{3.32}$). I calculated the gating charges arising from the transfer of a proton from $D^{2.50}$ via $D^{3.32}$ to the extracellular solution ($D173^{ECL2}$) in the M2R. The three aspartates were protonated and deprotonated in sequential order from $D^{2.50}$ to $D^{3.32}$ then $D173^{ECL2}$. As can be clearly seen, a voltage induced proton transfer from $D^{2.50}$ via $D^{3.32}$

to the extracellular space results in the recording of a gating charge, which is identical to that of a monovalent cation (Na^+) along the same distance. As shown in Figure 3-10, the gating charges are comparable with experimental values, as the movement of 1 Na^+ from the intracellular solution to the extracellular solution in the wt M2R gives rise to a gating charge of 1 e.

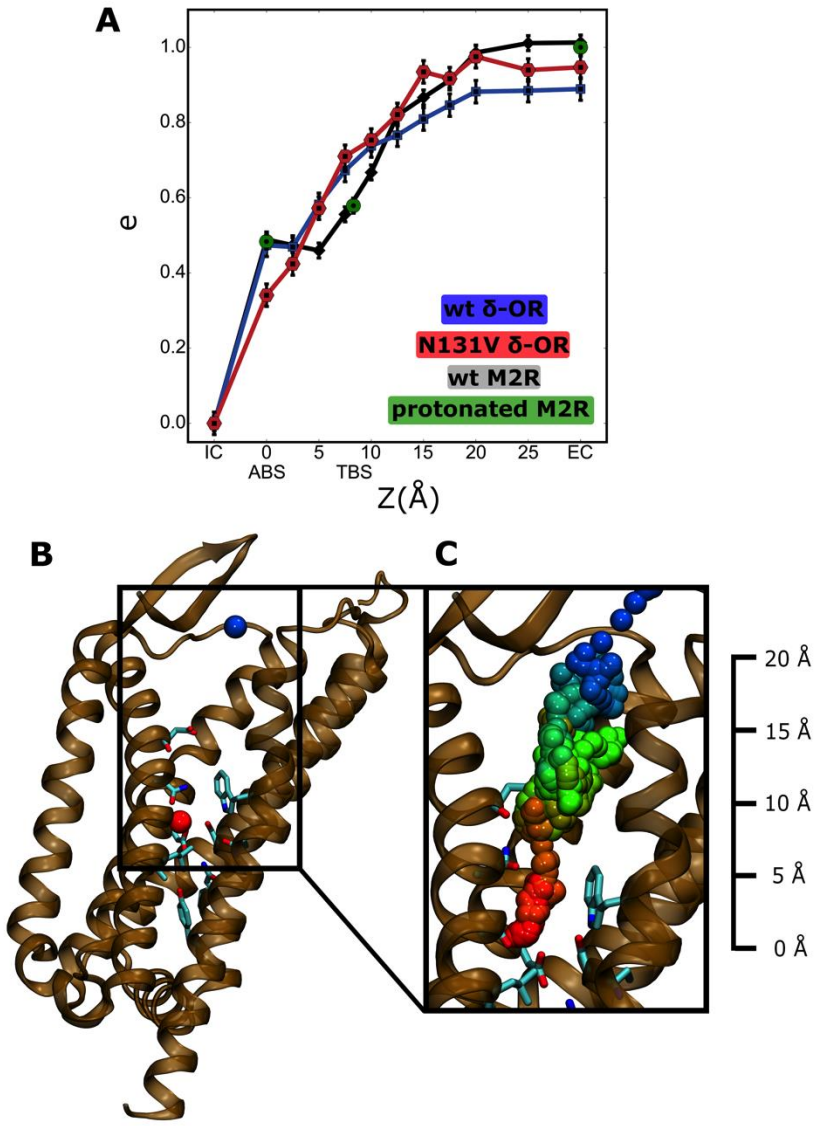

Figure 3-10: Gating charge resulting from the movement of a Na^+ ion or a proton

(A) Gating charge arising from the movement of Na^+ within the internal pocket of the M2R (black), wt δ-OR (blue), and the $N131^{3.35}V$ δ-OR (red), calculated with a step size of 2.5 Å. The maximal gating charges for the movement from the ABS to extracellular solution are 0.42e, 0.53e, and 0.63e for the wt δ-OR, wt M2R, and $N131^{3.35}V$ δ-OR, respectively. The green circles show the gating charge that would arise from a similar transfer of a proton from $D^{2.50}$ to the extracellular surface of the M2R via $D^{3.32}$ and D173 (~0.5e). **(B)** Na^+ positions corresponding to the allosteric binding site and the top of the orthosteric binding pocket (the Na^+ is colored red and blue respectively). **(C)** Pathway taken by the Na^+ ion from the hydrophilic pocket to the extra- cellular bulk solution in the δ-OR (color-coded according to simulation time proceeding

from red to blue); TM helix 5 has been omitted for clarity. The errors were estimated from the variation within the slopes of the charge- voltage relationships (see Figure 10D). Figure adapted from (70).

3.3 Discussion

The physiological importance of V_m in all cells is uncontested (122, 182), whilst the effect of V_m upon structure and function of the majority of integral membrane remains largely ignored. However in recent years, there has been increasing evidence supporting a direct influence of V_m upon the *Rhodopsin* family of GPCRs. For example, V_m has been demonstrated to modulate the agonist mediated activation of the α_{2A} adrenergic receptors (113), agonist binding and downstream signalling of the muscarinic receptors (112, 117, 183) and downstream signalling of the P_2Y_1 receptor purinergic receptor (116). The movement of gating charges has also been demonstrated in 2 distinct GPCR sub-families (α_{2A} adrenergic and muscarinic receptors) (112, 113, 118, 126). These receptors are expressed predominantly within excitable tissue, therefore it is conceivable that V_m could act as an important physiological control mechanism (114, 115). However, the precise mechanisms underpinning voltage sensitivity in the *Rhodopsin* family of GPCRs and the effects of V_m on the receptor conformation has so far remained elusive.

Our μs-timescale atomistic simulations of the δ-OR and M2R demonstrates that the allosteric Na^+ ion is the most highly mobile charge in the receptors TM domain. The protein does not undergo any significant conformational changes of other charged groups within the transmembrane domain, including $D^{3.32}$, $D^{2.50}$ and the $DR^{3.50}Y$ motif. The majority of the 16 hydrophilic pocket-lining residues are highly conserved in the *Rhodopsin* GPCR family, with the interesting exception of position 3.35, which can be occupied by polar groups e.g. asparagine in the δ-OR, or hydrophobic residues e.g. Valine in the M2R (Figure 1-13). My results therefore may be applicable to most of the *Rhodopsin* GPCR family, which contain the same internal structure.

3.3.1 Gating charges arising from the allosteric Na^+ ion

My computational studies show that a depolarised V_m of near physiological amplitude is capable to move the Na^+ ion from the ABS through the orthosteric site to the extracellular space, whilst demonstrating that this translocation can generate gating charges of between 0.42 and 0.63 e in the δ-OR and M2R. For the m1 and m2 muscarinic receptors, gating charges in the range of 0.55 – 0.85 e and 0.5 e for the α_{2A} adrenergic receptor were reported upon depolarisation (Table 3-1). The exceptional agreement between the experimental gating charges and the those caused by the movement of a cation (Na^+ or proton), which I observed, provides a plausible structural and mechanistic explanation for the experimentally measured gating charges. Of note, the only mutation that has successfully abolished gating charges is the mutation of $D^{2.50}$ to an alanine in the M2R (126). Although, expression of this mutation is particularly troublesome, as

noted by the authors, that the lack of gating charge could be attributed to low expression of the receptor or the $D^{2.50}$ could play a key role in the mechanism of voltage sensing. The lack of gating charge movements in the $D^{2.50}A$ mutant are in agreement with our results that the transfer of a cation from the ABS to the extracellular due to $D^{2.50}$ is the Na^+ ions counter ion, and forms a strong support for the latter explanation, i.e. the crucial role of the allosteric Na^+ binding pocket for the voltage regulation of GPCRs. In further agreement with our simulation, there is a parity of charged residues within the hydrophobic layer, which could provide an alternate explanation (Figure 3-11).

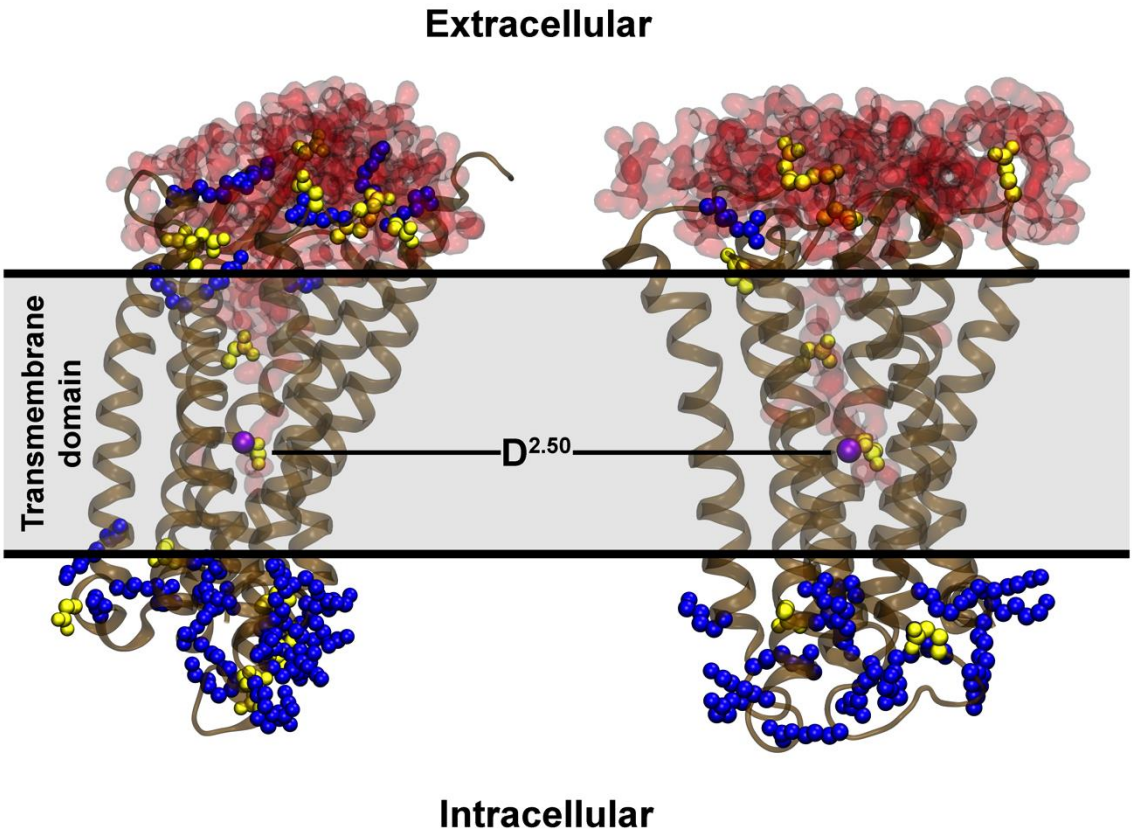

Figure 3-11: Charged amino acid distribution between the M2R and wt δ-OR

The figure shows the disparity of charged residues within the δ-OR **(left)** and M2R **(Right)**. In both receptors, only the charged residues $D^{2.50}$ and $D^{3.32}$ are within the transmembrane domain. Charged residues are shown as spheres for clarity (positive, blue; negative, yellow) and the Na^+ ion is shown as a purple sphere.

Moreover, the movement of the gating charge has been shown to affect ligand binding in the orthosteric ligand binding site (118, 126, 184), which is in agreement with our computational studies that a cation can move between the ABS, TBS and the extracellular space. Recent experiments have revealed that V_m modulates both G-protein dependent and G-protein independent signalling pathways in the muscarinic receptors, but the magnitude and direction of the allosteric modulation is highly dependent on the binding mode and precise chemical structure of the agonist (112). The voltage sensitive cation in my simulations can either relocate to or cross the orthosteric ligand-binding site, in a ligand dependent fashion (126).

The majority of the experimental measurements of GPCRs have been made in the presence of extracellular Na^+ (112, 113, 126), whilst other experiments were undertaken with no extracellular Na^+, however other cations were present, such as K^+, Ca^{2+} and the organic cation N-methyl-D-glucamine (NMDG) (118). It has been long known that other monovalent and divalent cations can interact with the hydrophilic pocket to a varying extent in previous experimental and computational studies (100, 106). Additionally, it has been shown that the commonly used organic cation amiloride is able to bind directly to the ABS and induce a similar allosteric effect as Na^+ (185, 186). Under physiological conditions, the most likely source of the gating charge is Na^+ due to its high extracellular concentration, and its clear detection in close proximity to the residue $D^{2.50}$ in the A_{2A} adenosine and δ-OR crystal structures (64, 65).

3.3.2 Gating charges arising from protons

It has previously been shown that the $D^{2.50}$ is likely to titrate near the pH 7 when the ion is not bound (180). I have therefore tested the likely possibility that a voltage induced deprotonation of the $D^{2.50}$ due to a pK_a shift and subsequent transfer of a proton to the extracellular space, could give rise to a similar gating charge. As expected, the migration of the proton gives an identical gating charge over the same distance to that of the monovalent cation Na^+. As previously mentioned, other cations and organic cations can bind to $D^{2.50}$, and theoretically undergo the same transition if their concentration is high enough or upon removal of Na^+ (185). I cannot exclude a more dynamic interplay between V_m, cations and the protonation state of the $D^{2.50}$, as throughout the simulations the protonation state of all titratable residues were fixed. The dynamic protonation of $D^{2.50}$ dependent on the position of Na^+, or upon the removal of the Na^+ the protonation of the $D^{2.50}$ could be modulated by the V_m, could play a role as a highly sensitive and robust voltage sensor or a subset of the sensor. Whilst some preliminary studies have been undertaken on the protonation state of key residues in the *Rhodopsin* GPCR family, very little is known on the interplay between Na^+ ion position and $D^{2.50}$ protonation state (96, 178, 180, 187).

The allosteric Na^+ binding site residing deep inside the hydrophilic pocket is conserved across the majority of *Rhodopsin* family GPCRs, with the exception of the visual rhodopsins, my results predict that the voltage sensitivity and gating charge movements could be a general feature of this class of membrane proteins. The receptors I studied in this chapter are all predominantly expressed in excitable cells, so it is tempting to speculate about the regulation of GPCRs by V_m and its physiological role.

It is interesting to consider the similarities and differences to the more canonical voltage-sensing domain (VSD), for example those commonly found in voltage gated K^+ and Na^+ channels (169). These channels contain a highly focused electric field through the VSD, which exist as an array, and acting together to allow for a greater displacement of a greater gating charge in total, ensuring excellent sensitivity to millivolt changes in the V_m. In contrast, the voltage sensing mechanism proposed here seems to be more highly adapted to large scale V_m changes in the order of ~200 mV (118, 126). Notably, the main voltage sensing mechanism I suggest for GPCRs lies outside the polypeptide chain and involves the movement of a

monovalent cation (Na^+) through the conserved hydrophilic pocket, or the modulation of the pK_a of the ultra conserved residue $D^{2.50}$, as opposed to the movement of a charged segment of the protein itself (Figure 3-12).

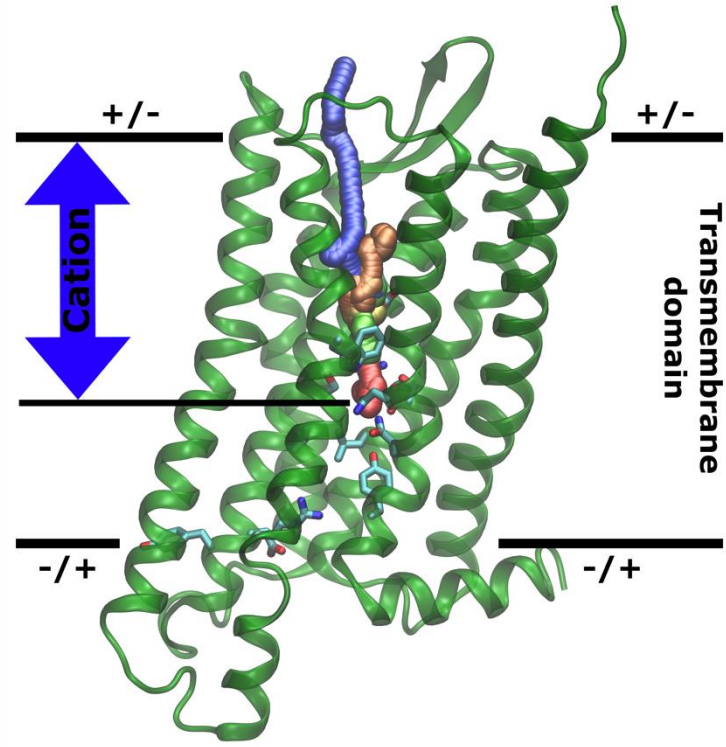

Figure 3-12: Graphical Representation of the Suggested Voltage- Sensing Mechanism in GPCRs
The hydrophilic pocket, accessible from the extracellular face only, connects the orthosteric ligand and the Na^+ binding sites in GPCRs. A Na^+ ion is bound to a conserved site near the ionisable residue $D^{2.50}$. The position of the ion within the pocket strongly responds to changes in membrane voltage. The movement of a cation along the TM axis in the water-filled pocket leads to a gating charge of ~0.5e when the ion travels from its allosteric binding site to the top of the ligand binding pocket. In Na^+-free conditions, a nearly identical gating charge can be elicited by a voltage-induced change in the protonation state of $D^{2.50}$ and movement of a proton. The side chain of $D^{2.50}$ is likely to be in a protonated state if no Na^+ ion is bound. In both cases, the voltage induced repositioning of cations involves a change in the ionic interactions within the allosteric binding site and the orthosteric ligand-binding site. Figure adapted from (125).

Previous experimental work has shown that mutation of the residues surrounding $D^{2.50}$ in the δ-OR receptor severely disrupts the signal bias between G-proteins and β-arrestin at a basal signalling level, as well as disrupting Na^+ binding to the receptor. The results presented in this chapter, show that V_m affects the occupation of the ABS with Na^+. Thereby indicating that V_m, and therefore the excitation state of the cells could have an impact on the signal bias between pathways in these studied receptors. The results presented here provide a rational for a new range of electrophysiology and receptor-functional experiments to tease apart the interplay between signal bias, V_m, Na^+ effect, pH and ligand specific allostery on GPCRs.

Chapter 4. Intracellular Permeation of Na^+ in an active state GPCR

4.1 Introduction

Since the first crystal structure of rhodopsin almost two decades ago (188), a number of structures have been solved, revealing conformational changes between the inactive and active state receptors, including common movements in the transmembrane helices and conserved residues termed "microswitches" (63, 189). However, despite a wealth of structural information, it is not understood how ligand binding leads to downstream activation of the intracellular effector proteins. There are major issues arising from crystal structures and wet lab experiments including: first, the x-ray structures represent static snapshots of highly dynamic receptors, crystallised under non-physiological conditions, which is likely to distort or mask crucial information, such as the internal hydration of the receptor. Second, wet lab experimentalists predominantly concentrate on specific signal pathways, either G-protein or β-arrestin, thereby potentially missing alterations in signal pattern.

4.1.1 The Na^+ effect

Interestingly, the active receptor conformations display a collapsed ion binding pocket around the $D^{2.50}$, which is unlikely to be able to bind cations (64, 74, 190). It was therefore proposed that the bound cation leaves the hydrophilic pocket during receptor activation by a ligand or upon formation of a receptor-G-protein complex. However, how this cation is displaced and which pathway it follows is currently unknown, though the forces felt by the ion such as the Na^+ ion concentration gradient as well as the presence of a hyperpolarised membrane potential, will drive the ion towards the cytoplasm.

Throughout this chapter, I therefore investigated the link between receptor activation, the fate of the bound Na^+ ion and its implications for signal transduction across the membrane. I used equilibrium and non-equilibrium atomistic simulations of the well-characterised m2 muscarinic receptor (M2R). The M2R is an excellent model for this study, due the availability of both inactive and active state crystal structures including a large array of experimental data (see Chapter 1 and 3). When addressing questions on ion binding, it is important to take into account the various physiologically relevant electrochemical conditions.

4.1.2 Interplay between GPCRs and the electrochemical gradient

As I showed in Chapter 3, depolarised potentials can expel the Na^+ ion via the orthosteric ligand binding site. However, in contrast to the excitable cells in which depolarised potentials exist, the majority of cell types exist in a hyperpolarised state. Therefore, the V_m and Na^+ concentration gradients are acting in synergistic manner, pushing the allosteric Na^+ ion through the receptor (Figure 4-1).

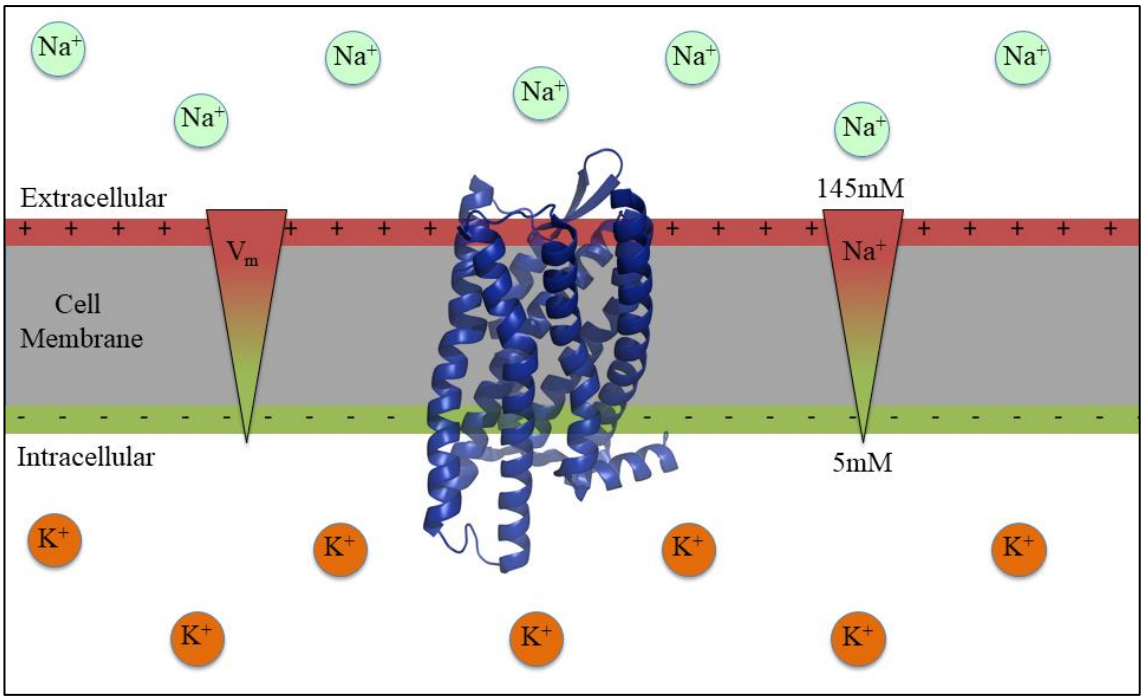

Figure 4-1: Ionic and voltage gradients across a cell membrane

The constituents in a simplified electrochemical gradient: electrical and Na^+ concentration gradient. **(Left)** Displays the electrical gradient from positively charged extracellular surface to the negatively charged intracellular surface of the membrane. The approximate strength of the electric field is 10^8 Vm^{-1}. **(Right)** Displays the concentration gradient of Na^+ from ~140mM in the extracellular to the low 5mM intracellular concentration. In this particular case both the Na^+ concentration gradient and the V_m act synergistically. However, they can oppose each other, as is the case of K^+ concentration gradient and V_m.

4.1.3 Chapter overview

Throughout the previous chapter, I observed that the movement of a cation from the hydrophilic pocket was possible under physiological conditions in the inactive receptor. However, here I focus on receptors present under a hyperpolarised potential and an ionic gradient. I observed that the Na^+ ion can readily transverse the hydrophobic layer of the active receptor migrating to the cytoplasm. This result implies that an exchange of Na^+ or other monovalent cations from the extracellular space to the cytoplasm is an important step in receptor activation. Furthermore, the movement of Na^+ within the receptor is tightly coupled to the protonation state of the $D^{2.50}$.

4.2 Results

4.2.1 GPCR activation opens a hydrated pathway through the receptor

As mentioned earlier the binding site for the Na^+ ion in the active crystal structures appears to adopt a collapsed conformation unable to accommodate the Na^+ ion. Therefore I was first interested whether the conformational change from the inactive to active receptor state renders the pocket sterically incapable of coordinating the Na^+ ion. I started from the inactive state structure of the M2R (PDB: 3UON) and using a targeted MD approach gently drove this conformation to the active state of the receptor (PDB: 4MQT)(Figure 4-2 A). My simulations indicate that the hydrophilic pocket within the active state of the M2R retains sufficient space for the ion. The ion is unlikely to move under these conditions, due to the electrostatic attraction between the ion and the negatively charged side chain of the $D69^{2.50}$. Ion binding is maintained throughout and after the transition from the inactive to active conformation induced by targeted MD (Figure 4-2 B).

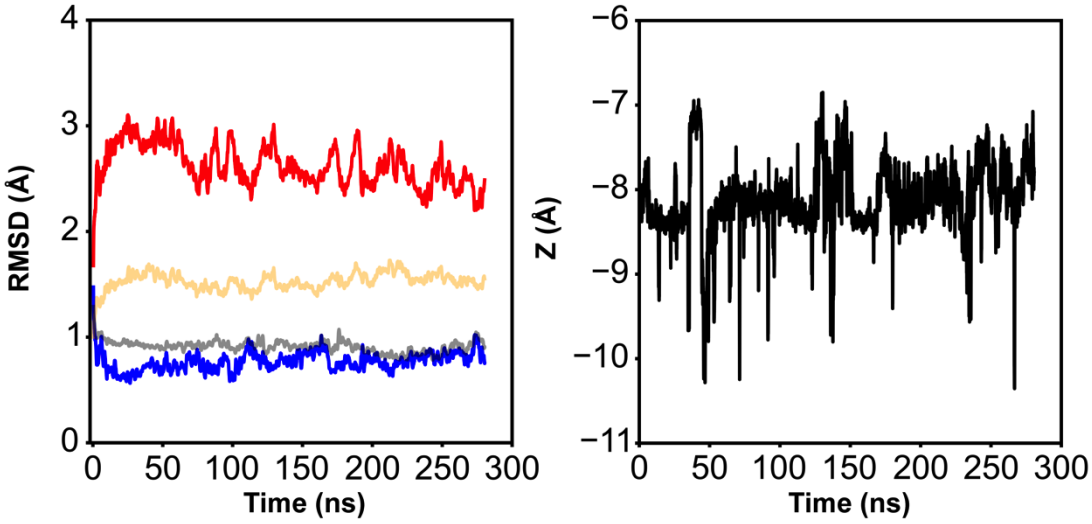

Figure 4-2: Observations during a targeted MD simulation from the inactive to the active state of M2R

(**A**) The red and blue lines correspond to the RMSD of TM6 relative to its inactive and active conformations (PDB: 3UON, 4MQT), respectively. The orange and grey lines correspond to the RMSD of all transmembrane helices relative to their inactive and active conformations, respectively. The RMSD of TM6 with respect to the active state structure remains below 1 Å following the transition (blue line: TM6 vs. active). The RMSDs of all seven TM helix residues were calculated using the backbone of residue numbers 25-46, 60-83, 96-123, 140-158, 189-210, 388-408, 422-443; those of TM6 from residues 388-408. (**B**) A stable position of the Na^+ ion is seen throughout the transition of the M2R from the inactive to active conformation. The Z coordinate is reported relative to the $D103^{3.32}$ Cα atom in the orthosteric ligand-binding pocket. Figure adapted from (156).

As expected, throughout the initial targeted MD simulation, I observed a widening of the intracellular portion of the transmembrane helices (TM 6 and TM 2) below the hydrophilic pocket during the conformational change. The widening allows the formation of a hydrated pathway connecting the orthosteric ligand binding site, the hydrophilic pocket and the G-protein binding site (Figure 4-2 B). Within the inactive structure a slim hydrophobic layer exists, delimiting the hydrophilic pocket and the G-protein binding site. Upon activation, the $NP^{7.50}xxY$ motif within this layer undergoes substantial conformational changes as evidenced by the $Y440^{7.53}$ sidechain. The formation of the hydrophilic channel, allows the sidechain of residue $Y440^{7.53}$ to occupy multiple conformation, consequentially modulating the shape of channel. The simulations show two major conformations of the sidechain of $Y440^{7.53}$ following the transition, a upward state, also observed in the inactive crystal structure (PDB: 3UON, Figure 4-3 D) and a downward state similar to that observed within the active crystal structure (PDB: 4MQT, Figure 4-3 E and Figure 4-4). The presence of a hydrated channel connecting the receptor ligand and effector binding sites has previously been reported in simulation studies of the $A_{2A}R$ and 5-HT_{1A} receptors, however the Na^+ ion was not taken into account in these simulations (69, 191).

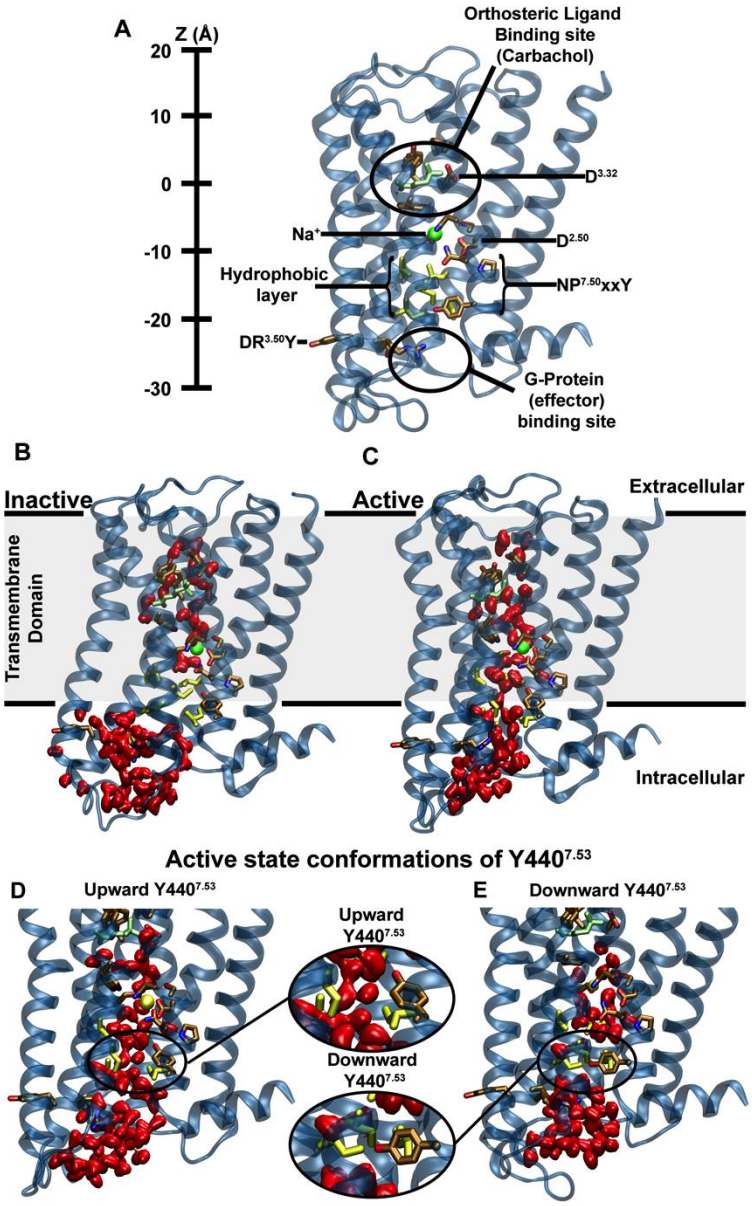

Figure 4-3: Major structural features and internal hydration of class A GPCRs in the inactive and active state as shown by the M2R

(A) The main structural features of class A GPCRs, as exemplified by the M2R, include seven TM helices (blue), an extracellular ligand binding site, the intracellular effector (G-protein) binding site as well as conserved and functionally important residues termed microswitches (selected ones are highlighted). The vertical axis (Z-coordinate) and all positions stated in the text use the Cα atom of D103$^{3.32}$ as reference. **(B)** Conformation of inactive M2R (PDB: 3UON) during the simulations showing the presence of the hydrophobic layer separating the hydrophilic pocket and effector binding site. **(C)** After transition to the active state (PDB: 4MQT), and further simulation, M2R displays a continuous water channel connecting the orthosteric ligand binding site, hydrophilic pocket and effector binding site. **(D-E)** Representative frames corresponding to the most populated sidechain states showing residue Y440$^{7.53}$ in an upward **(D)** and downward conformation **(E)**. Water molecules are shown in red (surface representation); the position of the allosteric Na^+ ion, as obtained from our initial simulations, is shown as a green sphere, and residues

forming the hydrophobic layer (yellow) as well as the bound ligand (carbachol, light green) are depicted in stick representation. Figure adapted from (156).

4.2.2 The position of the internal Na^+ ion is coupled to protonation of $D69^{2.50}$

I was next interested in the interplay between the Na^+ ion and the highly conserved titratable residue $D69^{2.50}$. Numerous computational studies have examined the protonation states of the residues $D69^{2.50}$, $D103^{3.32}$, the $D(E)R^{3.50}Y$ motif and Na^+ binding, and their functional implications on activation of several members of the *Rhodopsin* family of GPCRs (176, 180, 187). Here, I focused upon the interactions between the location of the Na^+ ion within the receptor and the protonation of $D69^{2.50}$. In collaboration with Catarina A. Carvalheda and Dr Andrei Pisliakov, we carried out pK_a calculations of the residue $D69^{2.50}$. Conformational snapshots were taken every 2 ns between 10 and 20 ns from my PMF window simulations (total > 800 snapshots). To separate the effects of the conformation of $Y440^{7.53}$ sidechain on the pK_a of $D69^{2.50}$, the pK_a calculations were run with the $Y440^{7.53}$ in an upward and downward conformation (Figure 4-3 D, E). The effects of the Na^+ ion position upon the pK_a of $D69^{2.50}$ were evaluated in 2 dimensions; the z-axis as described in the PMFs (Figure 4-11) as well as the distance of the ion to the titratable group.

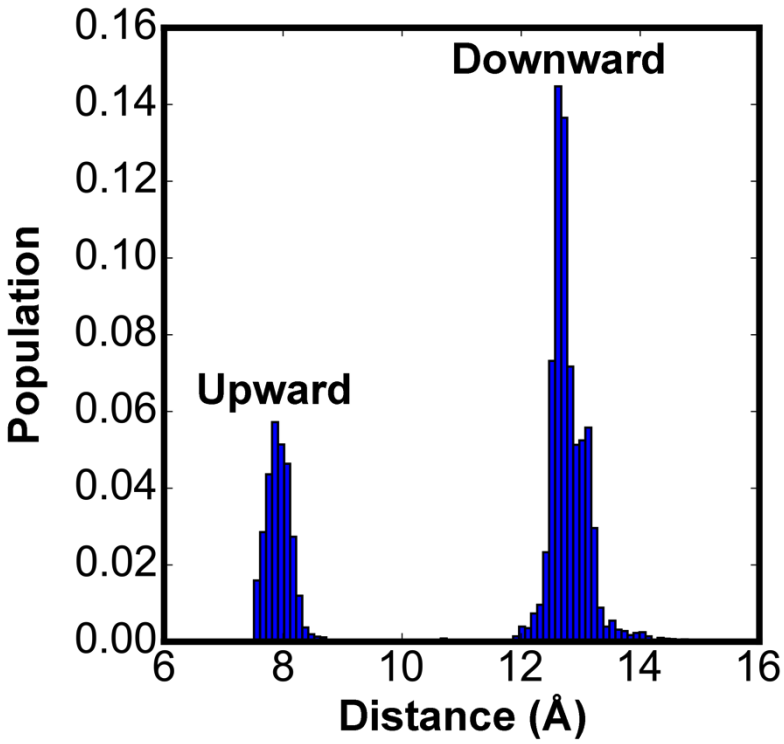

Figure 4-4: Distribution of distances between the $Y440^{7.53}$ (OH) and the $D69^{2.50}$ (Cα) atoms

Shown here is a representative distance distribution between the atoms $Y440^{7.53}$ (OH) and $D69^{2.50}$ (Cα) under a V_m of ~250 mV, with a protonated $D69^{2.50}$. The distributions display the two distinct conformational states of the residue $Y440^{7.53}$: an upward conformation clustered at ~8 Å and a downward conformation clustered around ~12.5 Å. Figure adapted from (156).

Figure 4-5 shows a clear shift in pK_a values resulting from the location of the Na^+ ion; therefore it is highly likely that the protonation state of $D69^{2.50}$ is modulated by the location of the cation. The pK_a calculations show that if the cation is within 3-5Å of $D69^{2.50}$ it leads to a pK_a of between ~3-4, thereby stabilising the negatively charged form of the aspartate. The pK_a of the Na^+ bound $D69^{2.50}$ displays a similar value to that of a solvent exposed aspartate (pK_a 4). In contrast, upon displacement of the cation to distances of >5Å, the pK_a increases substantially to values of ~10 and ~12 for the upward and downward conformations respectively. A substantial pK_a shift may be due to the location of $D69^{2.50}$ within the core of the membrane, surrounded by many non-polar residues and water molecules with low mobility. Interestingly, the sidechain conformation of $Y440^{7.53}$ does not have a substantial effect upon the final pK_a values, only accentuating the pK_a shift between 4 and 6 Å of Na^+-$D69^{2.50}$ distance. Transient fluctuations of the Na^+ from its binding site, which are facilitated by activation induced conformational changes within the hydrophilic pocket as well as V_m induced movements, can therefore be sufficient to lead to the protonation of $D69^{2.50}$.

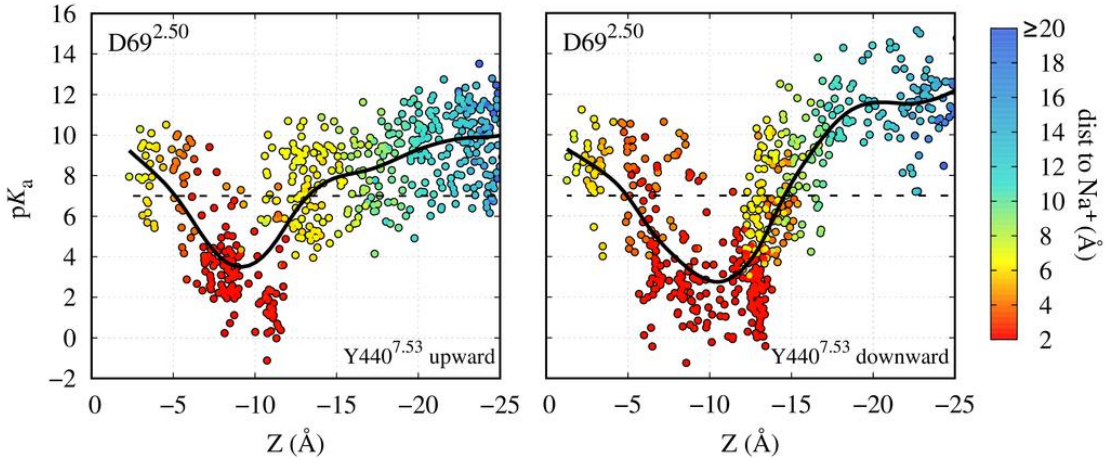

Figure 4-5: Proximity of the Na^+ ion modulates protonation of $D69^{2.50}$

Continuum electrostatics calculations of the pK_a of the $D69^{2.50}$ sidechain using a multitude of M2R conformations obtained from our atomistic simulations in the carbachol-bound active state, both for $Y440^{7.53}$ in the upward (left) and downward (right) conformations. The pK_a is shown as a function of Z, the separation between the Na^+ ion and the C_α atom of $D103^{3.32}$, which marks the orthosteric ligand binding pocket, along the TM axis (see Figure 4-3 A). The data points are, in addition, coloured according to their distance to the $D69^{2.50}$ sidechain. The black continuous line, a smoothed spline fit, indicates the approximate average pK_a for each separation for illustrative purposes, and the dashed black line shows a pK_a of 7. Figure adapted from (156).

For the protonation of $D69^{2.50}$ to occur, a proton has to reach the core of the receptor from the bulk solution. Here, I propose that the most likely proton entry route is from the extracellular solution, following the negative V_m gradient. In the case of the M2R and other *Rhodopsin* GPCRs, of which ~20% have a conserved $D^{3.32}$ within the orthosteric binding pocket, a proton could be transferred between the two sites via a short chain of water molecules (80). In the apo state (no ligand), the pK_a calculations of the M2R indicate that the $D^{3.32}$ is generally protonated (pK_a = 11.2±1.7), whilst upon ligand binding the pK_a is strongly

downshifted (pK_a = 7.6±1.9). The protonation shift of $D^{3.32}$ could therefore facilitate shuttling of protons to $D^{2.50}$; this could additionally be initiated by the coordination of a second cation within the orthosteric site (seen in the majority of simulations). Furthermore, as the sequence of activation is still in contention, if a G-protein-receptor complex is formed before agonist binding, the residue $D^{2.50}$ is easily accessible from the extracellular space via the deep water filled hydrophilic pocket. It has been previously hypothesized, that agonists and not antagonists, provide a hydrated pathway circumventing the ligand and thereby connecting Na^+ binding site and the extracellular space upon activation (191).

The protonation state of $D69^{2.50}$ demonstrates a large effect on the stability of the active structures throughout the simulations. Under both equilibrium and non-equilibrium conditions, the active state remains stable when the $D69^{2.50}$ is modelled as neutral (Figure 4-6, Figure 4-7), whilst when the $D69^{2.50}$ is charged the active receptors is more likely to revert back to the inactive state. This observation provides additional support for the importance of the Na^+ ion's location within the Na^+ binding pocket, which as shown in Figure 5 is linked to the protonation state of $D69^{2.50}$. The expulsion of the Na^+ ion and thereby the protonation of $D69^{2.50}$ is an important step in receptor activation.

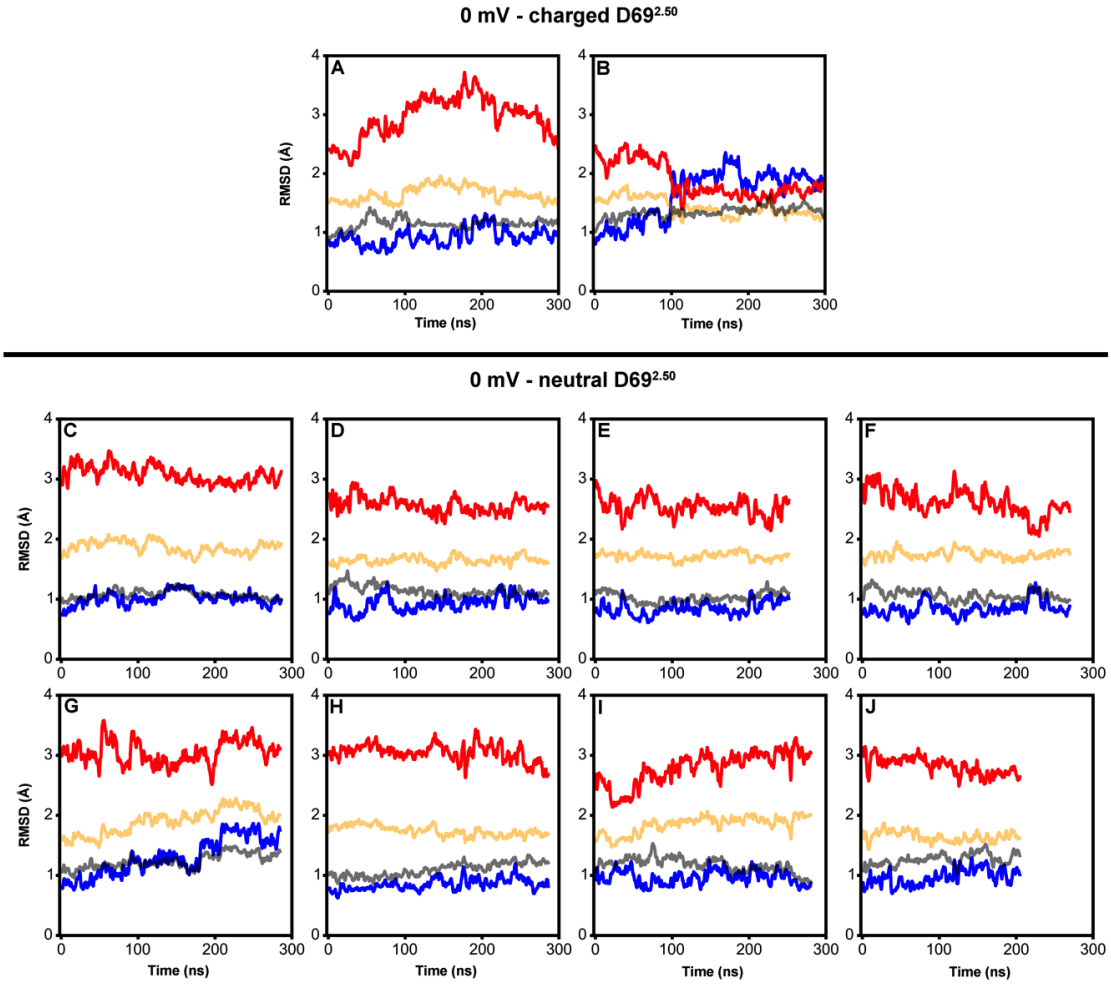

Figure 4-6: Backbone RMSD values during equilibrium MD simulations of the active state M2R
The red and blue lines show RMSD values with respect to the inactive and active conformations of TM6 (PDB: 3UON, 4MQT), respectively, while the grey and orange lines show the RMSD of all TM helices relative to their inactive and active conformations. D69$^{2.50}$ was either charged (A, B) or neutral (C-J). When the Na^+ ion is still bound to D69$^{2.50}$ in simulations with a charged D69$^{2.50}$, the receptor can switch back to the inactive conformation in some trajectories (see panel B; compare grey and orange lines). In contrast, all simulations with a neutral D69$^{2.50}$ remain stable in the active conformation. Figure adapted from (156).

4.2.3 Simulations under negative V_m show ion movement to the cytoplasm

In order to follow the trajectory of the Na^+ ion under more physiological conditions, I conducted atomistic simulations using the computational electrophysiology (CompEL) protocol (147) on the active conformation of the M2R. To apply conditions that represent the physio-chemical features of the cell-membrane, I used a physiological Na^+ ion gradient of 150:10mM across the membrane, from the extracellular to intracellular side. Additionally, I employed a small charge imbalance across the membrane evoking a hyperpolarised V_m of 250 and 500mV. Whilst the applied V_m is mildly supra-physiological, these voltages were chosen due to speed up any V_m related effects as well as optimizing the CompEL system efficiency. As discussed in the previous section, the wide range of pK_a values displayed by D69$^{2.50}$

precluded a single protonation state, therefore its sidechain was modeled in both the charged and neutral forms. Figures 4-6, 4-7 and 4-8 show the stability of the active conformation of the M2R under the four conditions simulated (four replicates in each condition). Interestingly in three out of eight simulations, in which D69$^{2.50}$ is charged and a Na^+ ion is still bound within the receptor, slide back into a inactive conformation. In contrast, simulations with a neutral D69$^{2.50}$ are never observed to drop back into the inactive state but occasionally adopt an intermediary conformation.

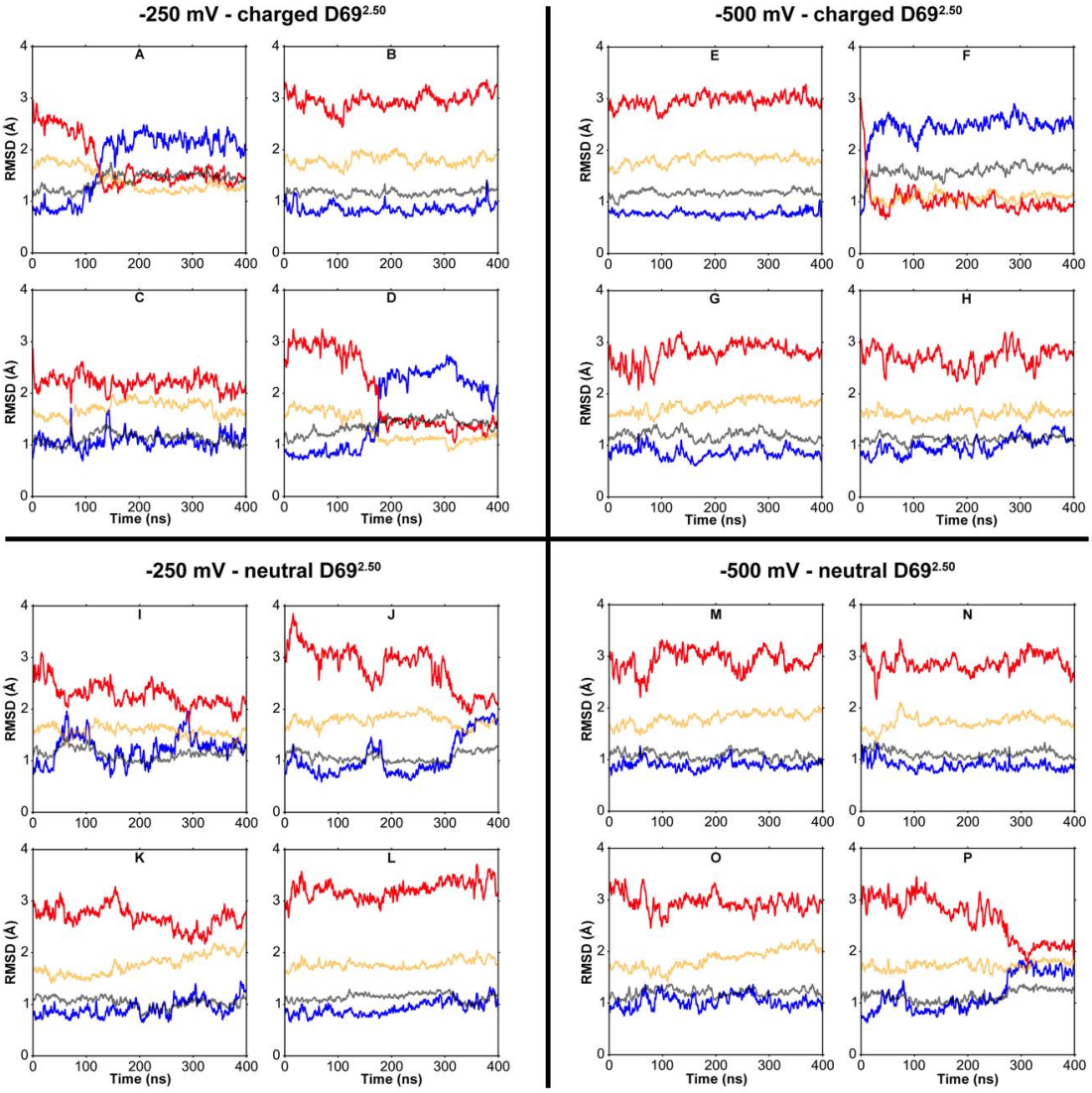

Figure 4-7: Backbone RMSD values during MD simulations of the active state M2R under V_m

The red and blue lines show RMSD values with respect to the inactive and active conformations of TM6 (PDB: 3UON, 4MQT), respectively, while the grey and orange lines show the RMSD of all TM helices relative to their inactive and active conformations. The active state simulations were carried out under a V_m of -250mV (A-D, I-L) or -500mV (E-H, M-P) and the protonation states of D69$^{2.50}$ were either charged (A-H) or neutral (I-P), as shown in the main text (Figs. 3, S8). When the Na^+ ion is still bound to D69$^{2.50}$ in simulations with a charged D69$^{2.50}$, the receptor can switch back to an inactive conformation (A, D and F; compare grey and orange lines). In contrast, simulations with a neutral D69$^{2.50}$ can show a change to an

intermediary conformation, but no drop back to an inactive-like state (grey and orange lines). Figure adapted from (156).

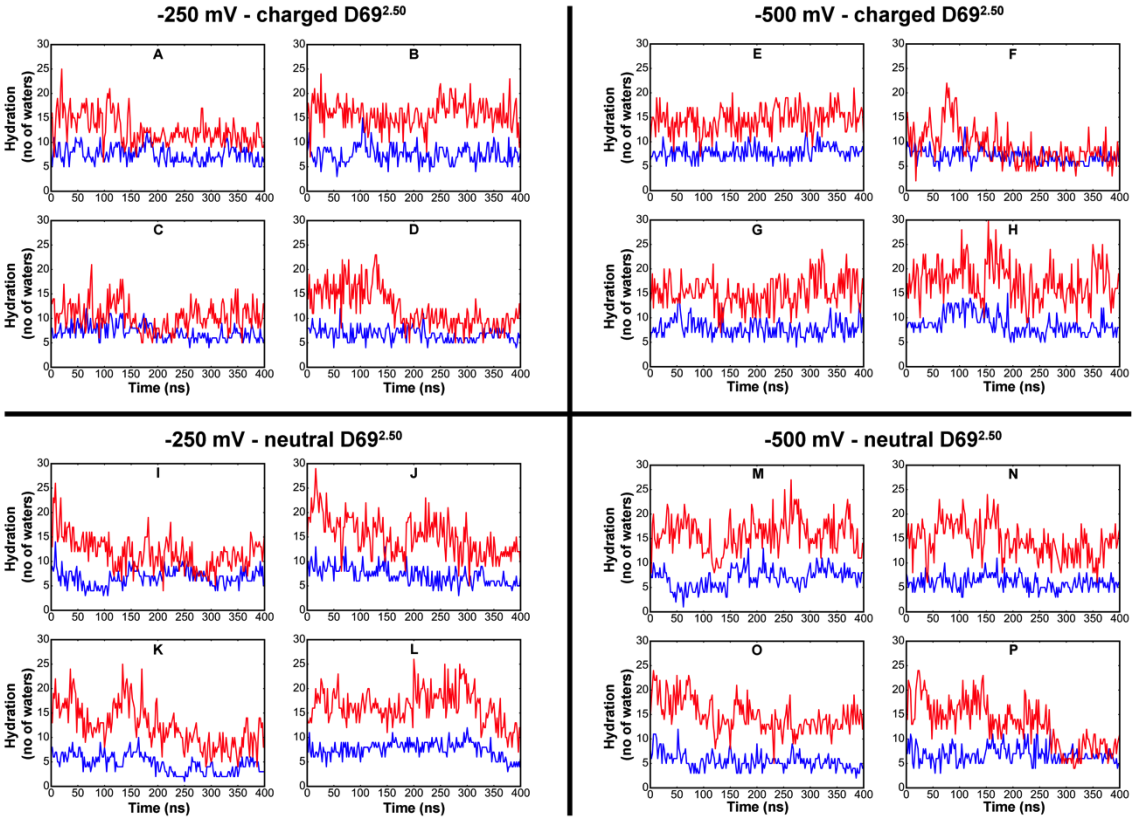

Figure 4-8: Hydration of the hydrophilic pocket and intracellular effector-binding site

The number of water molecules within the hydrophilic pocket shows a level hydration throughout the simulations, with a slight decrease in hydration with a neutral $D^{2.50}$ (Table 4-1). The number of water molecules within the intracellular effector-binding site is stable in the majority of simulations, with the decrease of water molecules correlated with the collapse of some systems to the inactive state (Fig S4, Table S1). The hydrophilic pocket was defined as z = ±4Å from the $D69^{2.50}$ Cα atom (blue lines) and the hydrated channel between the z = -4Å from the $D^{2.50}$ Cα atom and the z-coordinate of the $R^{3.50}$ Cα (red lines). The number of water molecules were recorded every 2ns throughout the simulations. Simulation conditions were as follows: (**A-D**) V_m: -250mV, $D^{2.50}$: charged (**E-H**) V_m: -500mV, $D^{2.50}$: charged (**I-L**) V_m: -250mV, $D^{2.50}$: neutral (**M-P**) V_m: -500mV, $D^{2.50}$: neutral. Figure adapted from (156).

In the simulations undertaken at -250 mV in the active state, the bound Na^+ ion displays a significant degree of mobility, regardless of the protonation state of $D69^{2.50}$ (Figure 4-10 A, B). The Na^+ ion is predominantly coordinated within the Na^+ binding pocket by the residues $D69^{2.50}$, $S110^{3.39}$, $N435^{7.45}$ and $S433^{7.46}$. Even whilst under a small V_m, a distribution of distances between the Na^+ ion and the Cγ of the residue $D69^{2.50}$ is seen, in which distances of >4.5 Å are not uncommon (Figure 4-9). As displayed by the pK_a calculations, only small excursions of the ion from its binding site on this scale are sufficient to have a significant impact

upon the pK_a and therefore the protonation state of the D69$^{2.50}$ side chain (Figure 4-5). I consequently investigated the effects of a protonation state change of the D69$^{2.50}$ residue in the active conformation.

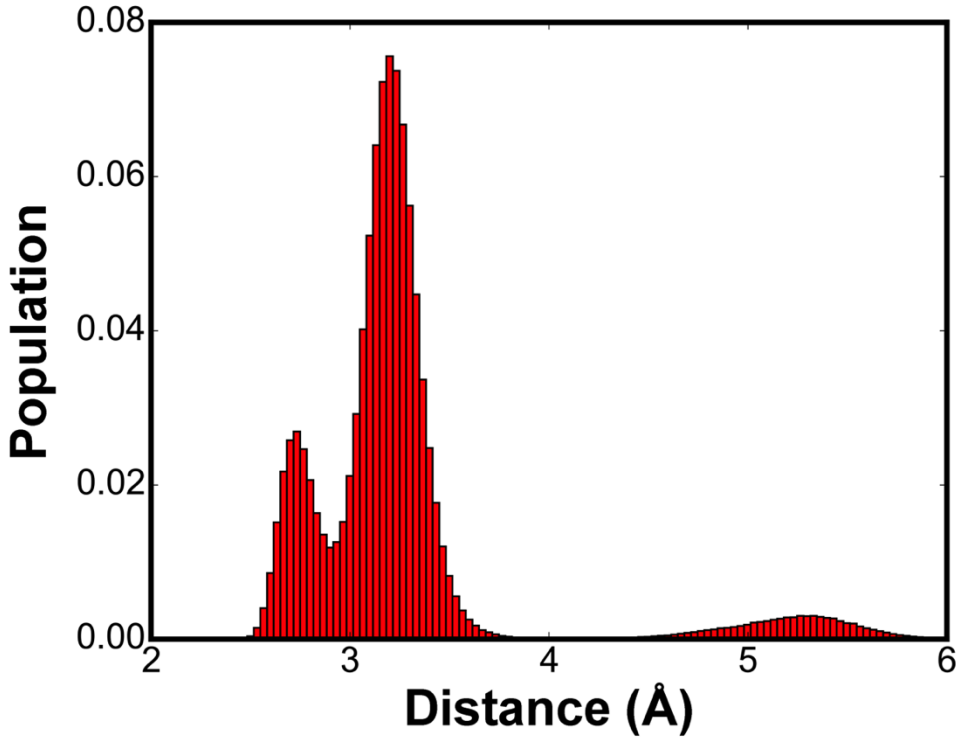

Figure 4-9: Distances between the Na^+ ion and D69$^{2.50}$

Distance distribution between Na^+ and D69$^{2.50}$ (C_γ) in the active state of M2R under -250 mV and charged D69$^{2.50}$. Figure adapted from (156).

The simulations reveal that, following the protonation of the key residue D69$^{2.50}$, the Na^+ ion can readily pass through the hydrated channel present within the active conformation of the M2R. Upon the neutralisation of D69$^{2.50}$, the Na^+ ion is expelled to the cytoplasm in three out of four simulations under a mild hyperpolarised V_m (-250 mV) (Figure 4-10 A, C). At -500 mV, the effect is expectably more pronounced and expulsion of the ion to the cytoplasm is seen within all simulations (Figure 4-10 B, C). In contrast, in simulations with a negatively charged D69$^{2.50}$, the transition to the cytoplasm was observed in only one out of eight simulations at the raised V_m of -500 mV (Figure 4-10 B). Interestingly, the trajectory of the Na^+ ion to the cytoplasm follows a highly similar route in each case, which is irrespective of the side chain conformation of Y440$^{7.53}$ (Figure 4-10 C).

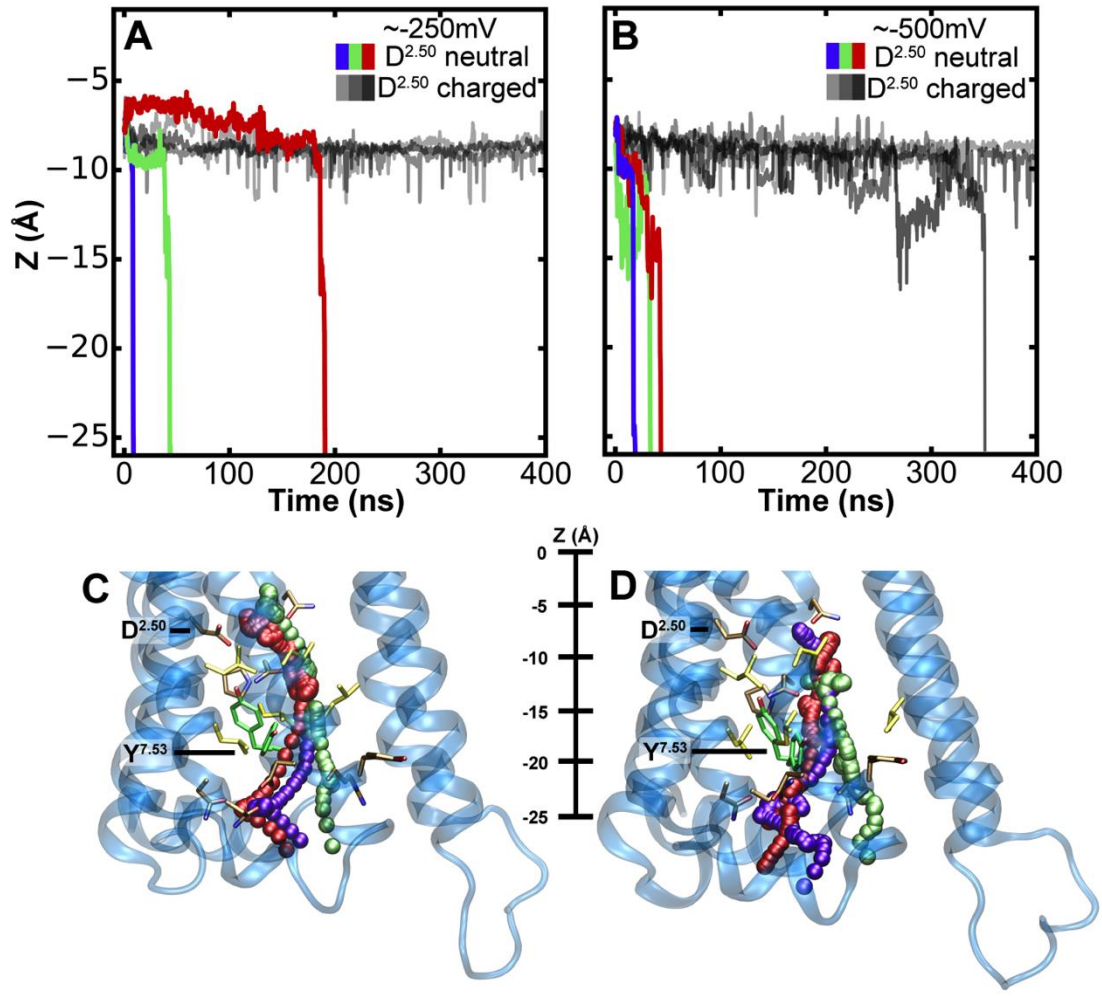

Figure 4-10: Migration of the Na^+ ion across the receptor to the intracellular side

Z-coordinate of the Na^+ ion in the M2R under a hyperpolarised V_m of -250 mV **(A)** and -500 mV **(B)**. Black/grey lines denote simulations with a charged $D69^{2.50}$; purple, green and red lines display simulations with neutral $D69^{2.50}$. Trajectories of the Na^+ ion moving from the hydrophilic pocket, accessible from the extracellular space, into the intracellular bulk solution at **(C)** -250 mV and **(D)** -500 mV (example trajectories are shown for each condition, please see Table 4-1 for a complete list). The color used to display the Na^+ ion corresponds to the trajectories shown in panels A and B, respectively. The $Y440^{7.53}$ upward and downward conformations are shown in green. The pathways of the ion towards the intracellular side are almost indistinguishable from each other until the ion passes $Y440^{7.53}$. Thereafter, the pathways diverge to some degree due to the widened exit region to the cytoplasm. Figure adapted from (156).

4.2.4 Energetics of Na^+ ion movement to the cytoplasm

To accelerate the V_m related movements, the initial simulations were undertaken at slightly supra-physiological levels of V_m. Therefore, to ascertain the physiological relevance of the previously observed ion transitions, I next evaluated the detailed equilibrium energetics of the Na^+ ion movements along the exit pathway (Figure 4-10 C) without any applied gradients. I calculated a Potential-of-mean-force (PMF) for the translocation of the cation in the four conditions described previously in the section 4.2.1. In addition

to quantifying the influence of the D69$^{2.50}$ protonation state, I also examined the role of the conformation of the residue Y440$^{7.53}$, which significantly modulates the width, shape and hydration level of the channel into the cytoplasm (Figure 4-11).

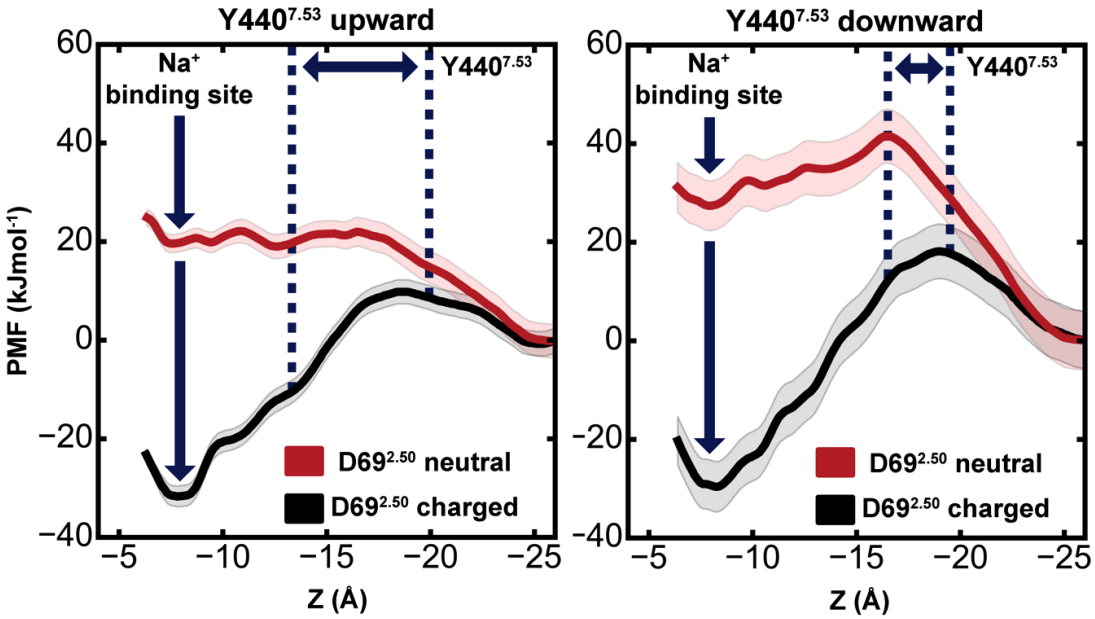

Figure 4-11: Energetics of Na$^+$ translocation from the hydrophilic pocket to the intracellular side
Equilibrium potential of mean force (PMF) profiles of the energetics of Na$^+$ translocation along the Z-axis in M2R without any applied voltage or concentration gradients. Four relevant states were considered: **(Left)** negatively charged D69$^{2.50}$ (black) or neutral D69$^{2.50}$ (red) with the Y440$^{7.53}$ sidechain in an upward conformation; **(Right)** negatively charged D69$^{2.50}$ (black) or neutral D69$^{2.50}$ (red) with a downward-oriented Y440$^{7.53}$ sidechain. The standard deviation of the PMF, obtained from Bayesian bootstrap analysis, is depicted as shaded area. For each PMF, the intracellular bulk solution was used as a reference, and the range of positions adopted by the Y440$^{7.53}$ sidechain is denoted by blue dotted lines.

Regardless of Y440$^{7.53}$ conformation when the D69$^{2.50}$ is negatively charged, the free energy difference between the Na$^+$ binding pocket and the cytoplasmic bulk solution is in the order of ~30 kJ mol^{-1}. Accordingly, as long as the key Na$^+$ binding residue D69$^{2.50}$ remains negatively charged, the active conformation of the M2R retains the Na$^+$ ion with relatively high affinity. As expected, the major energy barrier to the migration of the Na$^+$ ion into the cytoplasm is situated near the sidechain of the residue Y440$^{7.53}$. When it is in the upward conformation, the free energy barrier amounts to ~41 kJ mol^{-1}, whilst in the downward conformation, the barrier increases by ~8 kJ mol^{-1} to 48 kJ mol^{-1} (Figure 4-11).

The pK_a calculations of D69$^{2.50}$ show a clear dependence on the position of the Na$^+$ ion. Even a moderate displacement of the Na$^+$ ion from the key binding residue D69$^{2.50}$ is likely to lead to a protonation state change of the aspartate. In accordance to this, I also calculated the PMFs along a similar trajectory through the hydrated pathway with a neutral D69$^{2.50}$ (Figure 4-11; red lines). In contrast to the charged D69$^{2.50}$, the neutral state shows no affinity to the Na$^+$ ion, and therefore the trajectory of the Na$^+$ ion through the receptor

to the cytoplasm is not obstructed by any significant energy barrier larger than the thermal energy of the system ($kT.N_A$ = 2.57 kJ mol^{-1}, k: boltzmann constant, T: temperature (Kelvin), N_A: avogadro's constant) in the upward oriented $Y440^{7.53}$. However, when the $Y440^{7.53}$ is in the downward conformation, there is a slight but readily surmountable energy barrier (on physiological timescales) in the order of ~14 kJ mol^{-1}. Interestingly, the downward conformation of the $Y440^{7.53}$ sidechain in conjunction with the neutral state of $D69^{2.50}$ affects the shape and configuration of the hydrophilic pocket. The shape of the pocket under these conditions collapses slightly, shifting closer towards the structure seen within the active crystal structure, the resulting constriction of the Na^+ ion within the pocket leads to a decrease in hydrogen bonds formed between the protein, water and the Na^+ ion (Figure 4-12), which raises the free energy of binding at the hydrophilic pocket by a further ~7.5 kJ mol^{-1} (Figure 4-11 A, B red lines).

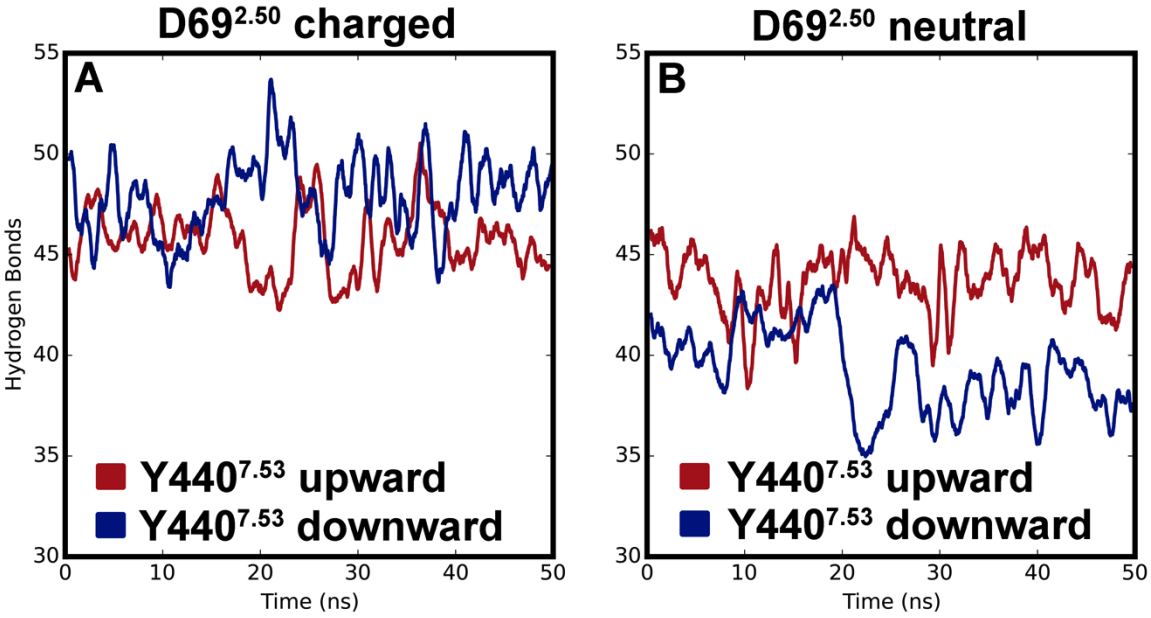

Figure 4-12: Number of hydrogen bonds surrounding the Na^+ binding site

The conformation of the $Y440^{7.53}$ sidechain and the $D^{2.50}$ protonation state affect the number of hydrogen bonds within a 10 Å diameter sphere of the Cγ atom of $D69^{2.50}$, defining the binding region for Na^+ and surrounding area. **(A)** With a charged $D69^{2.50}$ sidechain, a similar number of hydrogen bonds exist, irrespective of the conformation of $Y440^{7.53}$. **(B)** In the case of neutral $D^{2.50}$, the downward conformation of $Y262^{7.53}$ leads to a decrease in the number of hydrogen bonds within the hydrophilic binding pocket. The number of hydrogen bonds was derived from the umbrella sampling window trajectories. Figure adapted from (156).

To characterise the influence of the memebrane voltage, upon the free energy profile of the Na^+ ion translocating from the hydrophilic pocket to the cytoplasm, I first calculated the gating charge arising from the movement, in 2.5 Å increments between the position of $D103^{3.32}$ Cα and the cytoplasm. The movment of the Na^+ ion from the Na^+ binding site to the cytoplasm gives rise to a gating charge of ~0.45 e, in conjunction wth the conformational changes of the receptor. This is in excellent agreement with the inverse of this movement recorded in Chapter 3 (0.53 e). In a non-equilibrium case, such as a physiological V_m, the

energy will be raised in regard to the cytoplasm by ~4.4 kJ mol^{-1} per -100 mV (Figure 4-13). The PMFs show that regardless of the conditions tested with a neutral D69$^{2.50}$, the Na^+ ion can readily transverse the hydrophilic channel in the receptor and permeate to the cytoplasmic side under physiological transmembrane voltages. However, when the Y440$^{7.53}$ sidechain is in a downward conformation small activation barrier of ~7 kJ mol^{-1} will remain, but is surmountable in the physiological timescale.

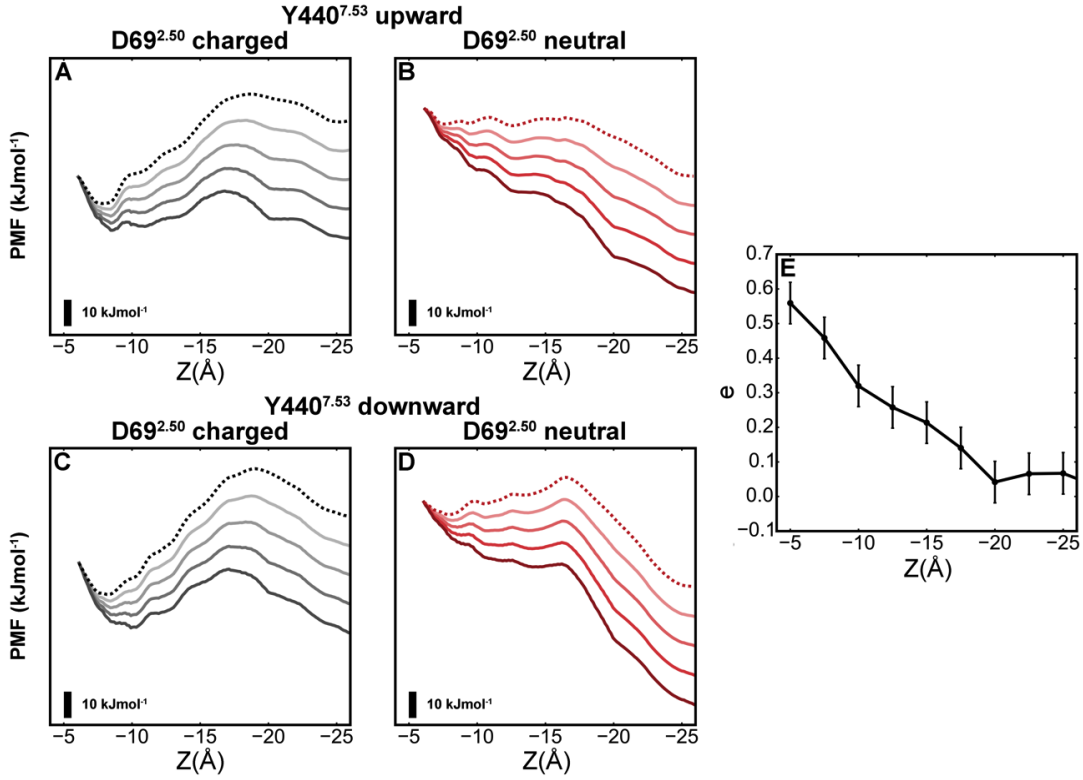

Figure 4-13: Non-equilibrium effect of Vm upon the PMF profiles of Na+ translocation to the cytoplasm

V_m induced tilt of the free energy surface (Figure 4-11) of Na^+ in a non-equilibrium case in the M2R under four different conditions: (**A**) Y440$^{7.53}$ upward, D69$^{2.50}$ charged (**B**) Y440$^{7.53}$ upward, D69$^{2.50}$ neutral (**C**) Y440$^{7.53}$ downward, D69$^{2.50}$ charged (**D**) Y440$^{7.53}$ downward, D69$^{2.50}$ neutral. Increments are from -250 mV (light) to -1000 mV (dark); dotted line indicates 0mV. The underlying voltage drop was mapped using the gating charge calculations (**E**) derived from the M2R receptor with Y440$^{7.53}$ upward and D69$^{2.50}$ charged. The panels display the relative free energy differences for each voltage regime; the black bar denotes an energy difference of 10 kJ mol^{-1} within each panel. Figure adapted from (156).

4.3 Conclusion

The primary role of GPCRs is to transmit extracellular information across the membrane into the cytoplasm, activating a range of intracellular effectors (34, 57, 192). The activation process is known to involve conformation changes within the receptor, including the so-called “microswitches” as well as the large-scale movement of the transmembrane helices 5, 6, and 7 on the intracellular side ultimately leading to the activation of the intracellular effectors proteins (130, 193–195). An interesting level of cooperativity exists

between the effector site and orthosteric ligand binding site, as it has long been recognised that effector binding and thereby the stabilisation of the active conformation, increases the affinity of agonists in the extracellular portion of the receptor (83, 196).

Monovalent cations, in particular Na^+, bind to a hydrophilic pocket deep inside the receptor, situated between the orthosteric ligand binding site and the intracellular effector binding site, and are known to be one of the strongest allosteric modulators in the *Rhodopsin* GPCR family (68, 107). Interestingly Na^+ was found to negatively modulate the affinity of agonists, to their respective GPCRs, whilst having no effect on antagonists. The Na^+ ion was proposed to stabilise the inactive conformation of the receptor (66, 68, 103). In support of this notion, x-ray structures of the inactive receptors crystallised at high resolution display a bound Na^+ ion within the hydrophilic pocket bound to $D^{2.50}$, while in the active crystals this pocket is collapsed, and no ions and very few waters molecules are observed (68, 130). The functionality of the *Rhodopsin* family of GPCRs are extremely sensitive to mutations surrounding the Na^+ binding site, which have a major impact on the signalling of the receptor (197). They either abolish G-protein activation, result in extreme pathway biased signalling, or in constitutive ligand-independent signalling (65, 185, 197).

My work throughout this chapter shows that the Na^+ ion binding pocket situated at the base of hydrated pocket, can only be accessed from the extracellular solution in the inactive conformation (70, 177). By contrast, it is extended through the receptor forming a fully permeable and hydrated channel in the active form of the M2R. The channel connects the three core binding sites within *Rhodopsin* GPCRs: The orthosteric ligand binding site, the Na^+ ion binding site and the intracellular effector binding site. Whilst the formation of a hydrated channel in the A_{2A} and 5-HT_{1A} receptors has been previously observed in simulations, change of protonation states and presence of the Na^+ ion were not taken into account in those studies (69, 191). I show here that the shift of the receptor conformation from the inactive to the active, permits the Na^+ ion to transverse the hydrated channel without experiencing any major energy barriers along its trajectory. The relatively high hydration level of this channel should be noted as an important factor in facilitating ion movement to the cytoplasm (Figure 4-8). The correlation between hydration and ion movement has previously been demonstrated in ion channels (173, 198, 199). This stands in stark contrast to simulations of the inactive state, where the application of far greater forces is necessary to achieve the translocation of Na^+ towards the cytoplasm, due to the lack of a continuous hydrated channel, and therefore the need to break the hydrophobic layer (200).

The translocation of Na^+ to the cytoplasm is highly likely to be facilitated by a protonation state change of the $D69^{2.50}$ from the negatively charged deprotonated form to the neutral protonated form, which occurs upon small displacements of the ion from its preferential binding position. The neutralisation of $D69^{2.50}$ significantly reduces the affinity of the Na^+ binding pocket to Na^+, increasing the likelihood of the ion migration to the cytoplasm. In physiological conditions the migration is predominantly driven by negative V_m and by a >10 fold Na^+ gradient across the plasma membrane. These both propel the ion through to the cytoplasm in a synergistic manner, permitting permeation at lower driving forces. In corroboration, I

observed that mild hyperpolarised potentials are sufficient to allow for fast translocation of the Na^+ ion to the Na^+ binding site to the cytoplasm in the nanosecond timescale of our simulations (Table 4-1).

$D^{2.50}$ charge state	Transmembrane potential (mV)	Replicate	Na^+ permeation	Hydrophilic pocket hydration	Effector pocket hydration
Negatively charged (deprotonated)	-250	1	No	7.6±1.6	12.6±3.1
		2	No	7.5±1.6	15.8±2.7
		3	No	7.2±1.6	10.4±2.9
		4	No	6.7±1.3	12.1±4.1
Negatively charged (deprotonated)	-500	1	No	7.9±1.4	14.6±2.6
		2	No	7.0±1.4	9.1±3.7
		3	**Yes**	7.9±1.8	15.2±3.1
		4	No	8.7±2.1	17.5±4.0
Neutral (protonated)	-250	1	**Yes**	6.7±1.7	11.8±3.4
		2	**Yes**	7.2±1.8	15.1±4.0
		3	**Yes**	4.7±1.9	12.2±4.3
		4	No	7.6±1.6	16.4±3.5
Neutral (protonated)	-500	1	**Yes**	6.9±2.0	15.9±3.5
		2	**Yes**	6.0±1.5	14.5±3.5
		3	**Yes**	5.5±1.7	14.8±3.3
		4	**Yes**	6.8±1.7	13.0±4.7

Table 4-1: Permeation of Na^+ into the cytoplasm and receptor hydration
A complete list of simulations displaying the individual conditions: TM potential, the charge state of $D^{2.50}$, observation of Na^+ permeation to the intracellular side and the hydration of the receptor: the hydrophilic pocket, z = ±4Å from the $D69^{2.50}$ Cα atom and the hydrated channel between the z = -4Å from the $D^{2.50}$ Cα atom and the z-coordinate of the $R^{3.50}$ Cα. The number of water molecules were recorded every 2ns throughout the simulations. Table adapted from (156).

In a brief summation of my results, the conformational changes arising from agonist binding from the extracellular solution and intracellular effector binding from the cytoplasmic side shifting the receptor to its active state, which modulates the shape of the Na^+ binding pocket and thereby the interplay between the Na^+ ion and $D69^{2.50}$. Subsequently, this leads to a shift in the pK_a of $D69^{2.50}$ and therefore a protonation state change of the residue, facilitating the egress of the Na^+ ion via the hydrated channel to the cytoplasm.

4.3.1 GPCR activation

I propose that the translocation of Na^+ to the cytoplasm, facilitated by the hyperpolarised V_m and ionic gradients, is a crucial step in the receptor activation process. Once the Na^+ has been expelled, the receptor may be locked in an active conformation, by the protonation of $D^{2.50}$. It has been shown by several groups

that GPCRs, once activated, remain in a prolonged active state, capable of signalling from intracellular organelles after internalisation from the cell membrane (41, 201). The key role of Na^+ is reflected in the nearly complete conservation of the Na^+ binding pocket across the entire *Rhodopsin* family. The mechanism suggested here is consistent with ligand-independent signalling (termed basal signalling) of GPCRs (202), explaining this phenomenon as spontaneous protonation of $D69^{2.50}$ and egress of the Na^+ to the cytoplasm, leading to receptor activation (Figure 4-14). Throughout the ions transition to the cytoplasmic side, it is conceivable that the ion will interact with other key residues in the GPCR-cytoplasmic interface, and if the G-protein if bound, induce further conformational changes there. The interface includes a number of charged and polar residues (Figure 3-11), including a polar network which extends across all G-proteins, similar to the polar network observed within GPCRs, which helps enable ion movements (80, 203).

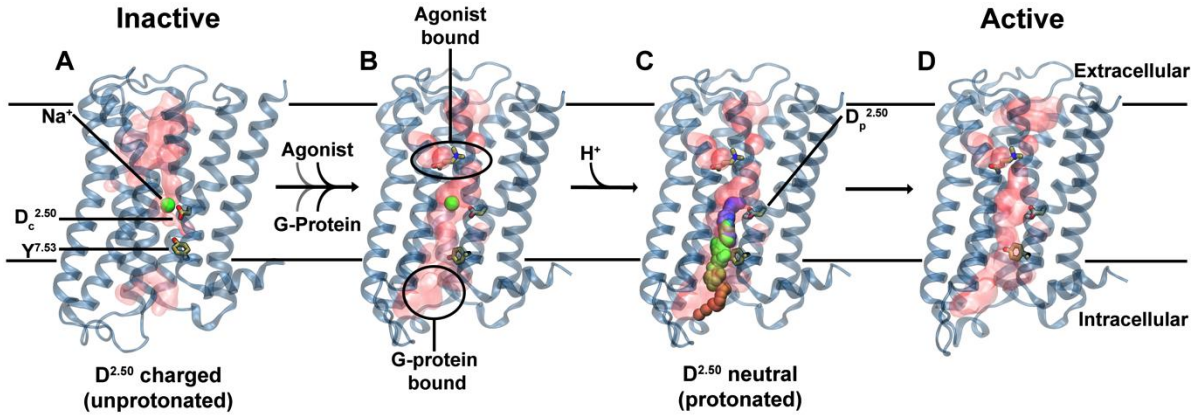

Figure 4-14: Proposed role of Na+ translocation in GPCR activation

Key checkpoints during the transition from the inactive (A) to active (D) state of the receptor. **(A)** The initial, inactive receptor conformation shows no bound agonist or G-protein, and displays a Na^+ ion bound in a pocket which is sealed towards the cytosol by a hydrophobic layer around $Y^{7.53}$. **(B)** G-protein and agonist bind to the receptor (in undetermined order), leading to the formation of a continuous water channel across the GPCR. The increased mobility of the Na^+ ion results in a pK_a shift and subsequent protonation of $D^{2.50}$. **(C)** Neutralization of $D^{2.50}$ and the presence of the hydrated pathway facilitate transfer of Na^+ to the intracellular side, driven by the transmembrane Na^+ gradient and the negative cytoplasmic membrane voltage. **(D)** The expulsion of Na^+ towards the cytosol results in a prolonged active state of the receptor. Figure adapted from (156).

As proposed by our simulations and pK_a calculations, the movement of charges within the transmembrane domain such as the transfer of Na^+ and protons, should be strongly influenced by the transmembrane voltage. As shown in the Chapter 3, as well as experimentally by other groups, it has been demonstrated that GPCR signalling is allosterically modulated by V_m (70, 112, 115, 116, 125, 168, 204). The expulsion of the Na^+ ion in Chapter 3 by a depolarised V_m would consequently allow for the protonation of $D^{2.50}$. The voltage sensitivity applies to the conformation of the receptor as well as the actual activation mechanism of the receptors downstream effectors. My results are consistent with the electrophysiological experiments described previously, as they imply that a movement of ions in the receptor are intimately linked to the activation process.

The allosteric regulation of GPCRs by V_m is potentially of high relevance to receptors expressed in electrically excitable cells (123, 205, 206). In these cells types, the V_m undergoes large oscillations between -90 and 50 mV during action potentials (120). The receptor can therefore regulate its downstream signal depending on the specific cell type and its excitation status (125). However, as described in Chapter 1 section 1.5 the receptors signalling process can be modulated to an exquisite level by the surrounding environment such as membrane composition, pH, ionic composition and V_m. Thereby the receptor activation can be tuned to a far greater degree than individual cell types, but down to the spatial location within the cell and individual organelles (123, 207, 208).

These results suggest a model for the activation of the *Rhodopsin* GPCR family, in which the conformational changes induced by either the binding of the intracellular effector and/or agonist are intertwined with the transfer of Na^+ to the cytoplasm and protonation changes. Of importance, these conformational changes include the rearrangement of the motif $NP^{7.50}xxY$, which when in an upward conformation permits a near barrier free permeation of Na^+ to the cytoplasm. The residue $Y^{7.53}$ is the first polar contact of the Na^+ ion on the intracellular pathway, forming a functional link between the important motif and the Na^+ binding site. Na^+ free receptors are likely to be shifted to the active conformation, which could potentially explain the prolonged mechanisms of signalling observed in many GPCRs. Here, my results provide evidence linking signal transduction and the allosteric modulation by V_m, pH and Na^+ concentration.

Chapter 5. The interplay between protonation and activation of the δ-OR

5.1 Introduction

As discussed within the previous chapters, GPCRs form the largest group of integral membrane proteins in the human genome (4). In the last few decades, GPCRs have been shown to signal via multiple pathways such as the classical G-protein, β-arrestin and kinase pathways (12). The δ-OR crystal structure (PDB: 4N6H) was the second receptor in which the allosteric Na^+ ion was seen, where it is coordinated by the conserved $D^{2.50}$ (Figure 1-14)(65, 209). The Na^+ binding site is part of a conserved hydrophilic pocket, of which only position 3.35 is the least conserved, with a balanced distribution of hydrophobic and hydrophilic residues (Chapter 1 section 1.4.2)(210). Interestingly, Fenalti et al. also mutated position 3.35 from asparagine in the wt δ-OR to either an alanine or valine. In both cases this resulted in a β-arrestin constitutively active receptor (65).

Although the common mechanism of GPCR activation has yet to be identified, the activation mechanism in many GPCRs encompasses several features including TM domain movement, side chain movement, rearrangement of solvent clusters and hydrogen bond networks. Interestingly, the basal activity of GPCRs suggests that the activation energy of the receptor is low and not that much higher than thermal fluctuations ($kT.N_A$ = 2.57 kJ mol^{-1}, k: boltzmann constant, T: temperature (Kelvin), N_A: avogadro's constant). If the activation energy were prohibitively higher than the thermal fluctuations then the receptor would be unable to activate in the absence of agonist binding (178).

5.1.1 Allosteric modulation of the Rhodopsin GPCR family by pH

An interesting feature which was alluded to in Chapter 4 is the effect of the protonation states of the three key titratable residues within the *Rhodopsin* GPCR family, $D^{3.32}$, $D^{2.50}$ and $D/E^{3.49}$. A body of evidence exists, showing the effects of pH upon GPCR activation (96, 97, 178–180, 211). Predating any structural information, Ghanouni et al were able to demonstrate the effects of pH upon ligand binding and basal signalling. Upon lowering the pH they demonstrated that the basal signalling of the receptor increased whilst ligand binding decreased (96). Since then, computational studies on the protonation state of $D^{2.50}$ have reached a consensus: The sidechain of $D^{2.50}$ is likely to be charged upon binding Na^+ and neutral upon the removal of Na^+ (176, 180, 212). Recently, effects of protonation upon the receptor were further demonstrated by the use of accelerated MD (aMD) to force the receptor into new conformations (176). However this study did not look at the key role of waters as well as the hydrogen bond network throughout the Na^+ binding receptor.

Throughout the previous two chapters, I showed that the movement of a cation from the hydrophilic pocket is possible under physiological conditions. The binding of a Na^+ ion to the Na^+ binding pocket has been

shown to drastically reduce the flexibility of the receptors, likely to confine them to more inactive conformations. In contrast, the absence of the Na^+ ion increases receptor flexibility and allows it to sample more active conformations (176, 177). These previous results demonstrate a key role of the Na^+ ion and its location within the *Rhodopsin* family of GPCRs. However, under experimental conditions it has been shown that the members of the *Rhodopsin* family are able to activate their cognate effectors under a wide range of voltages and ionic conditions. Therefore, whilst it conceivable that other mono- and divalent cations are able to bind, it is possible for these receptors to function in their absence (100, 212).

5.1.2 Chapter overview

Throughout this chapter, I will investigate the link between receptor activation and the protonation states of $D^{2.50}$ and $D^{3.49}$ using the δ-OR as a model system, including the previously described constitutive mutants, $N131^{3.35}A$ and $N131^{3.35}V$ (Figure 5-1). As I am looking exclusively at the effects of the protonation states and concurrently the effects of the single mutants. As I described in the previous chapters, the effects of V_m upon the receptor is conferred by the movement of the Na^+ ion or proton within the Na^+ ion binding pocket. In classical MD simulations the number of atoms and bonds remain constant, therefore the effect of V_m is applied artificially to the receptor. This approach allows the use of single bilayer simulations which allows for longer timescale simulations as well as a greater number of replicates due to the reduced number of atoms.

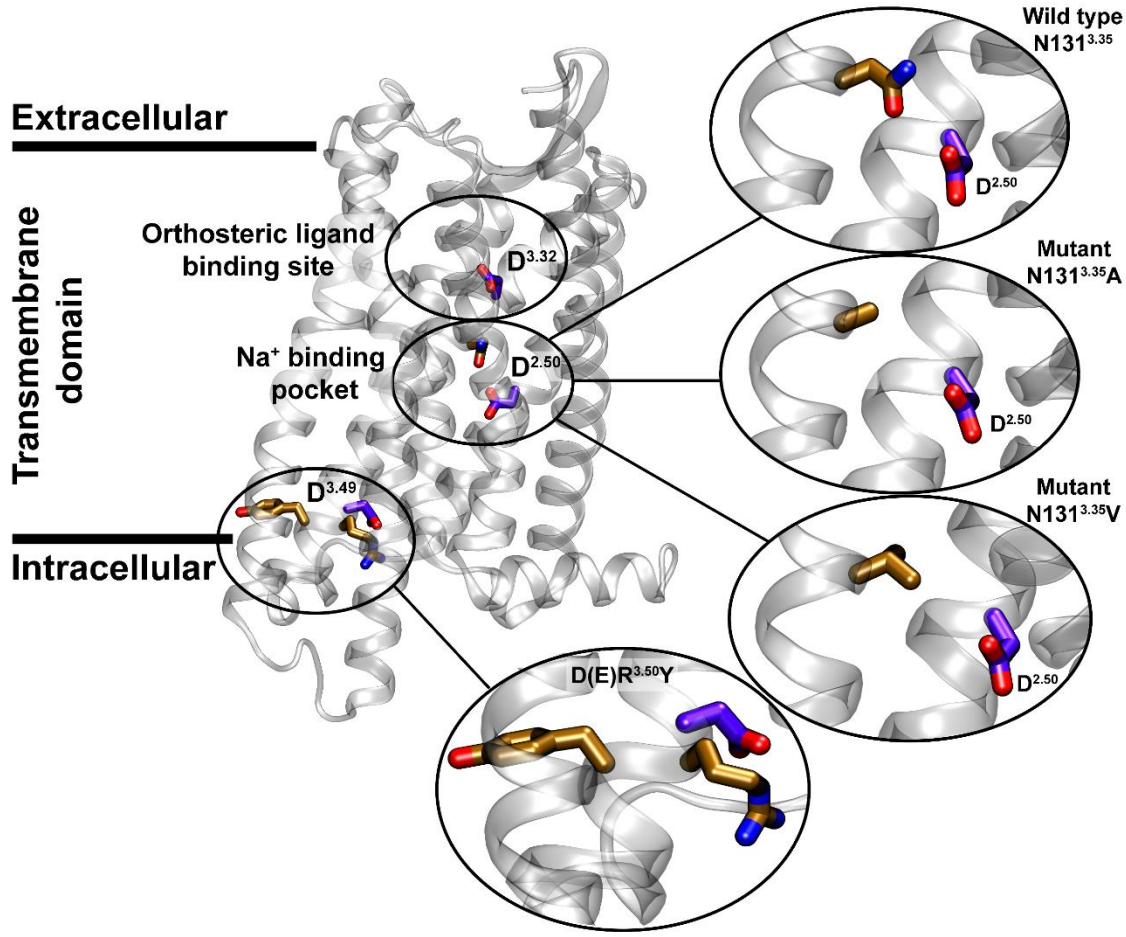

Figure 5-1: The δ-OR mutations and protonatable residues

Depicted here is the δ-OR, highlighting the three protonatable aspartate residues-within the orthosteric ligand binding site ($D^{3.32}$), the Na^+ binding site ($D^{2.50}$) and the D(E)$R^{3.50}$Y ($D^{3.49}$) motif are shown in purple. On the right hand side, the wt $N131^{3.35}$ and the two mutated residues $N131^{3.35}$A and $N131^{3.35}$V are shown.

5.2 Results

More than 110 μs of atomistic simulations were conducted on the wt and mutant δ-OR with varying protonation states. For the wt δ-OR and the mutants $N131^{3.35}$A and $N131^{3.35}$V, three different protonation state configurations of the key titratable residues $D95^{2.50}$ and $D145^{3.49}$ were simulated (Figure 5-1, Table 5-1). The two titratable aspartates ($D95^{2.50}$ and $D145^{3.49}$) were initially modelled in a negatively charged state due to their location where they interact with the counter charges of Na^+ and $R^{3.50}$ respectively.

Receptor	Protonation State		Total Simulation Time (µs)	Number of Replicates
	$D^{2.50}$	$D^{3.49}$		
wt	Charged	Charged	16.62	4
wt	Neutral	Charged	12.39	4
wt	Neutral	Neutral	11.7	4
$N131^{3.35}A$	Charged	Charged	17.18	4
$N131^{3.35}A$	Neutral	Charged	12.28	4
$N131^{3.35}A$	Neutral	Neutral	11.21	4
$N131^{3.35}V$	Charged	Charged	2.80	1
$N131^{3.35}V$	Neutral	Charged	12.26	4
$N131^{3.35}V$	Neutral	Neutral	11.35	4

Table 5-1: Simulation conditions specifying the protonation states of $D95^{2.50}$ and $D145^{3.49}$.
A complete list of simulations displaying the individual conditions: the mutation of $N131^{3.35}$, the protonation state of $D95^{2.50}$ and $D145^{3.49}$.

5.2.1 Receptor stabilisation by the negatively charged $D95^{2.50}$ and $D145^{3.49}$

As previously described in Chapter 3, the Na^+ ion remains bound to the negatively charged $D95^{2.50}$, with increasing fluctuations in the mutant receptors compared to the wt δ-OR (Figure 5-2). As no V_m is applied to these systems, the Na^+ ion does not leave the Na^+ binding pocket. However, the Na^+ ion undergoes brief excursions to the orthosteric ligand-binding site coordinated by the sidechain of $D128^{3.32}$ in the $N131^{3.35}A$ mutant (Figure 5-2 B). The free energy profiles shown in Chapter 3 (Figure 3-4) show the Na^+ ion in the wt receptor is predominantly coordinated in ABS-1 with brief fluctuations to ABS-2. This is supported by observations in Figure 5-2 A, by contrast, the PMF for the $N131^{3.35}V$ mutant displays a broader energy minimum around the Na^+ binding pocket (Figure 3-4 B), which is reflected by the fluctuations in Figure 5-2 C. As the modulation of Na^+ binding by the δ-OR mutants are well described within Chapter 3, I focused upon the effects of the δ-OR mutants and varying protonation state upon three key domains and microswitches within the receptor: the Na^+ binding pocket, $NP^{7.50}xxY$ and the $D(E)R^{3.50}Y$ motifs (see section 1.4).

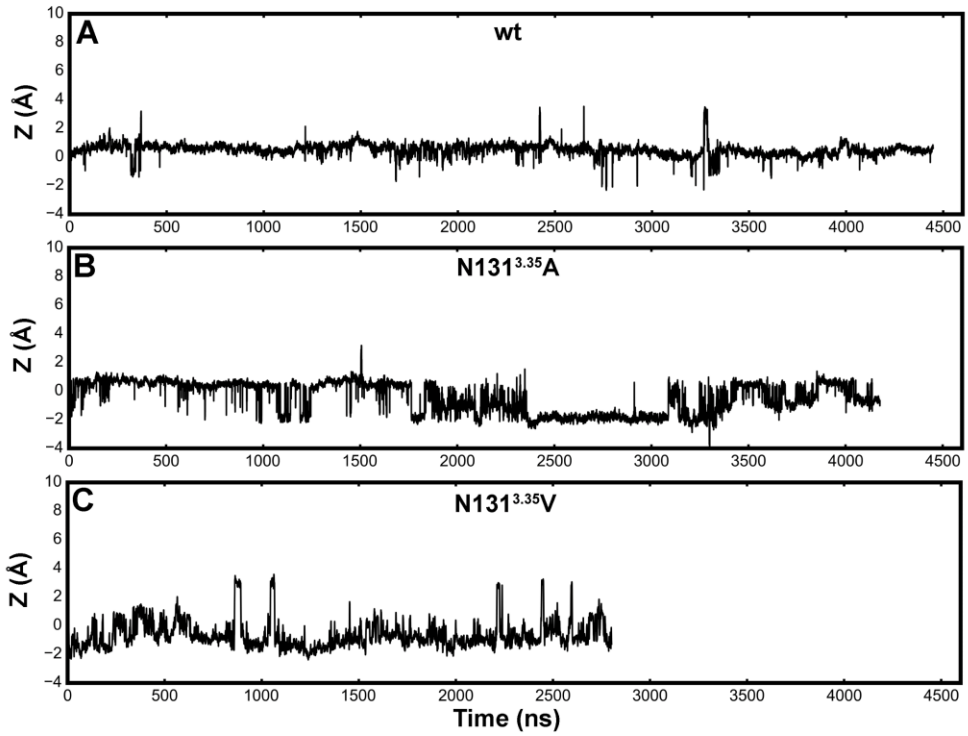

Figure 5-2: Effect of the N131$^{3.35}$ mutation upon Na^+ binding

Z-coordinate of the allosteric Na^+ ion bound within the Na^+ binding pocket in the wt δ-OR **(A)**, N131$^{3.35}$A δ-OR mutant **(B)** and the N131$^{3.35}$V δ-OR mutant **(C)**. This figure shows the increasing destabilisation of the Na^+ ion within the N131$^{3.35}$ mutant receptors. For all trajectories see Appendix Figure 8-1.

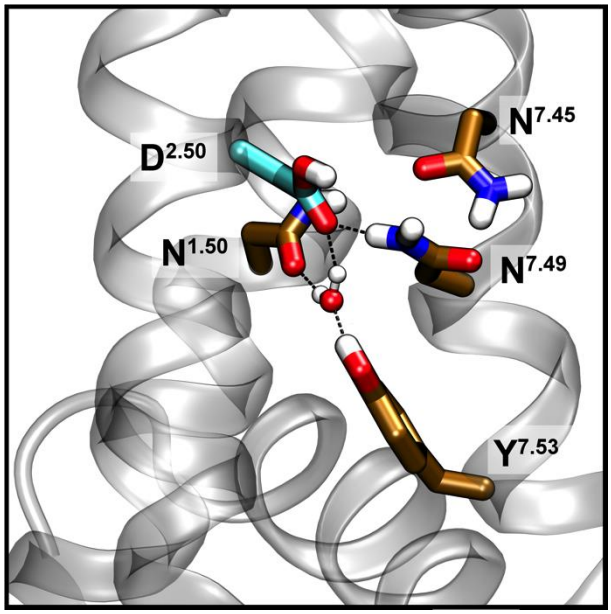

Figure 5-3: Key Na^+ binding site residues in the δ-OR

The inactive δ-OR, displays a stable interaction pattern within the Na^+ binding site. Depicted here are the initial orientations of N310$^{7.45}$ and N314$^{7.49}$ in which the carboxyl and amide groups face D95$^{2.50}$, respectively. Shown here is the ultra conserved water molecule mediating the hydrogen bond network between N67$^{1.50}$, D95$^{2.50}$ and Y318$^{7.53}$. Hydrogen bonds are shown as dashed black lines.

The initial inactive conformation δ-OR displays a highly stable Na^+ binding pocket. The Na^+ binding site contains two core components. First, the conserved water molecule mediating the hydrogen bond network between $N67^{1.50}$, $D95^{2.50}$ and $Y318^{7.53}$. Secondly, the conformations of $N310^{7.45}$ and $N314^{7.49}$, in the inactive conformation they are oriented so that their carboxyl and amide groups face the residue $D95^{2.50}$, respectively (Figure 5-3).

The side chains of $N310^{7.45}$ and $N314^{7.49}$ within the Na^+ binding pocket undergo no significant movements from the initial inactive conformation in the wt δ-OR. The side chains of residues $N310^{7.45}$ and $N314^{7.49}$ display exceptional stability in the inactive conformation (Figure 5-3 and Figure 5-4). In the δ-OR mutants $N131^{3.35}$A and $N131^{3.35}$V, the greater fluctuation of the ion within the Na^+ binding pocket destabilises the sidechains of $N314^{7.49}$. In these simulations the carboxyl group of $N314^{7.49}$ reorients to coordinate the Na^+ ion when it moves deeper within the pocket (Figure 5-4 B and C). This effect is seen to a greater extent in the $N131^{3.35}$V δ-OR mutant due to the Na^+ ion being situated lower in the pocket (Figure 5-2 and Figure 5-4 C).

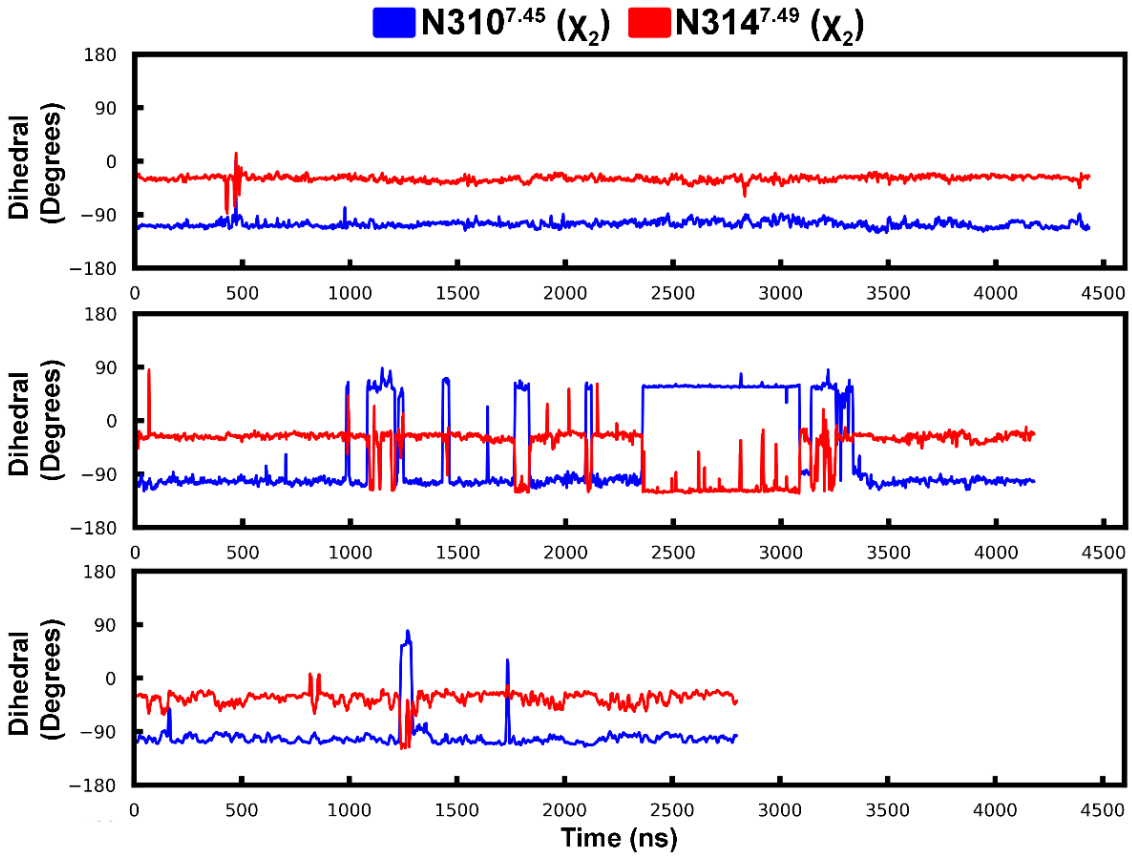

Figure 5-4: Effects of a charged $D95^{2.50}$ and $D145^{3.49}$ upon the Na^+ binding pocket

The dihedral angle χ_2 of the $N310^{7.45}$ (blue) and the $N314^{7.49}$ (red) sidechains. Shown here is the slight destabilisation of the Na^+ binding pocket upon mutation of $N131^{3.35}$, in contrast to the wt receptor. For all trajectories see Appendix Figure 8-2.

To monitor the conformational shift from the inactive receptor to the active state, I will use three distance measurements as activation criteria. To date, there is no active state crystal structure of the δ-OR and therefore I will use the active μ-OR crystal structure (PDB ID: 5C1M) as a guide, describing the activated receptor conformation (Figure 5-5, (190)). So far, all active state structures show similar conformational features (for review see reference 215).

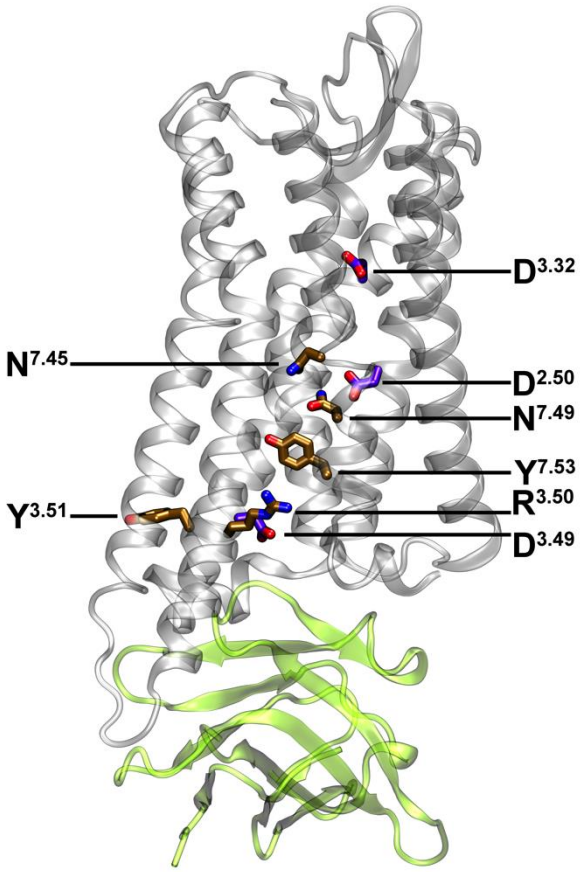

Figure 5-5: Crystal structure of the active state μ-OR

Depicted here is the μ-OR (silver), highlighting residues involved in the activation of the receptor. The three protonatable aspartate residues within the orthosteric ligand binding site ($D^{3.32}$), the Na^+ binding site ($D^{2.50}$) and the D(E)$R^{3.50}$Y ($D^{3.49}$) motif are shown in purple. The sidechain of $Y^{7.53}$ is shown here in the horizontal conformation, and the $R^{3.50}$ is shown in the extended state pointing towards the Cα of $Y^{7.53}$. A bound nanobody to the G-protein binding site stabilising the active state is shown in green. (PDB ID: 5C1M).

As demonstrated in Chapter 4, the activation of the receptor induces the movement of TM 5 and 6 away from the core of the receptor. Therefore, here I use a measure of the distance between the intracellular domain of TM 6 and TM 2 ($T84^{2.39}$-Cα: $I259^{6.33}$-Cα distance, μ-OR guide cut-off: 15 Å). Furthermore, in active GPCRs the sidechain of $Y^{7.53}$ is oriented in a horizontal conformation facing across the intracellular effector-binding site. Therefore, the second activation criterion employed is the sidechain conformation of the residue $Y318^{7.53}$ in the $NP^{7.50}$xxY motif as captured by the distance between $Y318^{7.53}$-OH: $D95^{2.50}$-Cα (μ-OR guide cut-off: 12 Å). In active state GPCRs, the sidechain of $R^{3.50}$ is released from its compact

inactive state to extend into the intracellular effector-binding site. The third activation criterion I monitored is the sidechain of R146$^{3.50}$ in the D(E)R$^{3.50}$Y motif (R146$^{3.50}$-CZ: Y318$^{7.53}$-Cα distance, μ-OR guide cut-off: 8 Å). In order for the receptor to be classified as an active state and not an intermediate state, all three of the above criteria must be met.

Within the wt and N131$^{3.35}$V δ-OR mutant, the receptor displays no significant movement towards the active state in this protonation regime. The microswitches within the D(E)R$^{3.50}$Y and NP$^{7.50}$xxY motifs stably remain in the inactive conformation (Figure 5-6).

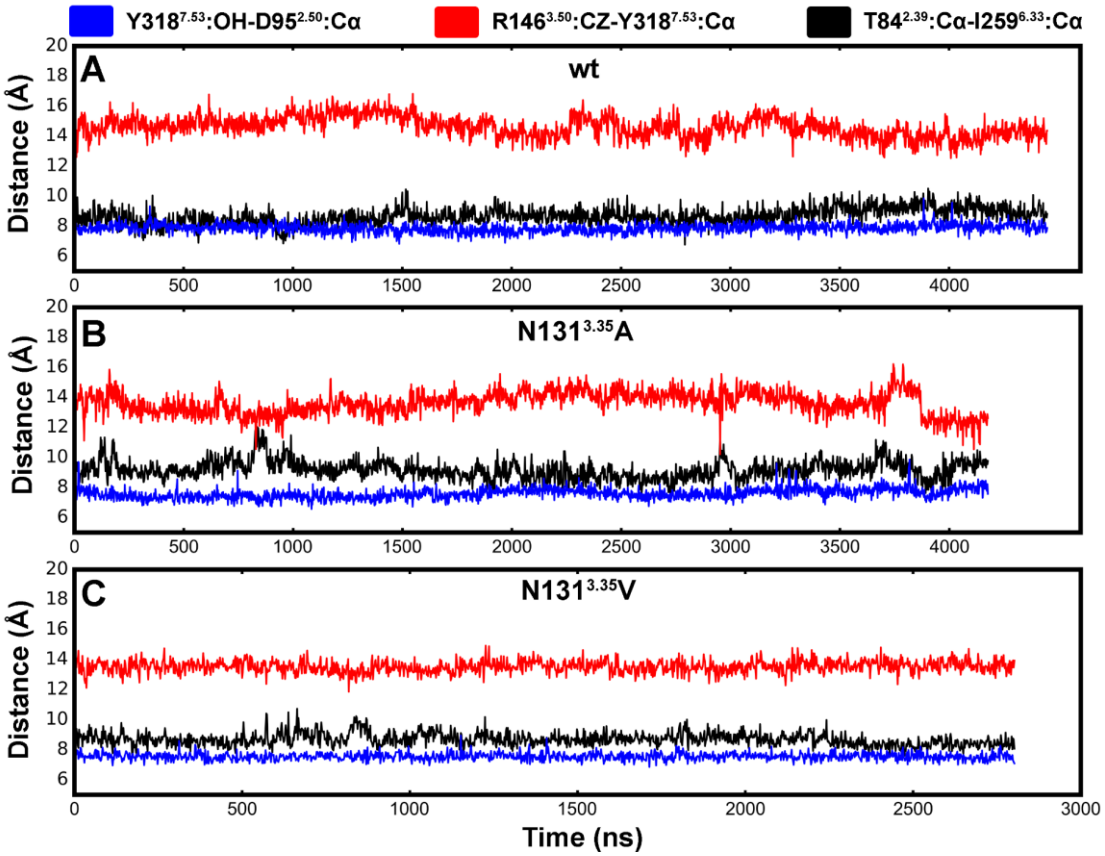

Figure 5-6: Effects of a charged D95$^{2.50}$ and D145$^{3.49}$ upon the activation of the δ-OR

The criteria for the activation of the δ-OR receptor. With a negatively charged D95$^{2.50}$ and D145$^{3.49}$, both the wt and two δ-OR mutants (A-C) do not deviate from their inactive state. Shown is the distance between Y318$^{7.53}$-OH and D95$^{2.50}$-Cα (blue), R146$^{3.50}$-CZ and Y318$^{7.53}$-Cα (red), and T84-Cα and I259-Cα (black). For all trajectories see Appendix Figure 8-3.

5.2.2 Receptor destabilisation by the protonation of D95$^{2.50}$

The initial simulations within section 5.2.1 provide a base line against which the effects of varying protonation states can be compared. The Na^+ ion and therefore a putatively charged D$^{2.50}$ have been proposed to stabilise the inactive conformation of the receptor, this was seen within Chapter 4 and has been

demonstrated in refs (66, 68, 103). As described in Chapter 4, the active receptor displays a collapsed Na^+ binding pocket, which is unlikely to be favourable for cation binding (64, 74, 190). Therefore, based upon the pK_a calculations reported in the previous Chapters which showed that $D^{2.50}$ is likely to be protonated without its counter ion (Na^+), I removed the bound Na^+ ion from the Na^+ binding pocket and simulated the three previously described δ-Opioid receptor variants with a protonated $D95^{2.50}$.

Interestingly, protonation of the residue $D95^{2.50}$ destabilises the positions of two asparagine residues within the Na^+ binding pocket, causing the orientation of $N310^{7.45}$ to reverse (Figure 5-7). Within the wt and the mutant δ-ORs, the interactions between the $N310^{7.45}$ sidechain and $D95^{2.50}$ are disrupted, allowing the sidechain move away from $D95^{2.50}$ by ~1-2 Å (Figure 5-13 B). The strong hydrogen bond network between sidechains of $D95^{2.50}$, $N310^{7.45}$ and $N314^{7.49}$ is also disrupted, increasing the flexibility of the $N314^{7.49}$ sidechain. In contrast to the sidechain of $N310^{7.45}$, $N314^{7.49}$ displays far greater flexibility. The head group of residue $N314^{7.49}$ can rotate by approximately 90°, allowing either the amide or carbonyl group of $N314^{7.49}$ to displace the hydrogen bond between $Y318^{7.53}$-OH and the highly conserved water molecule (Figure 5-3 and Figure 5-13, B).

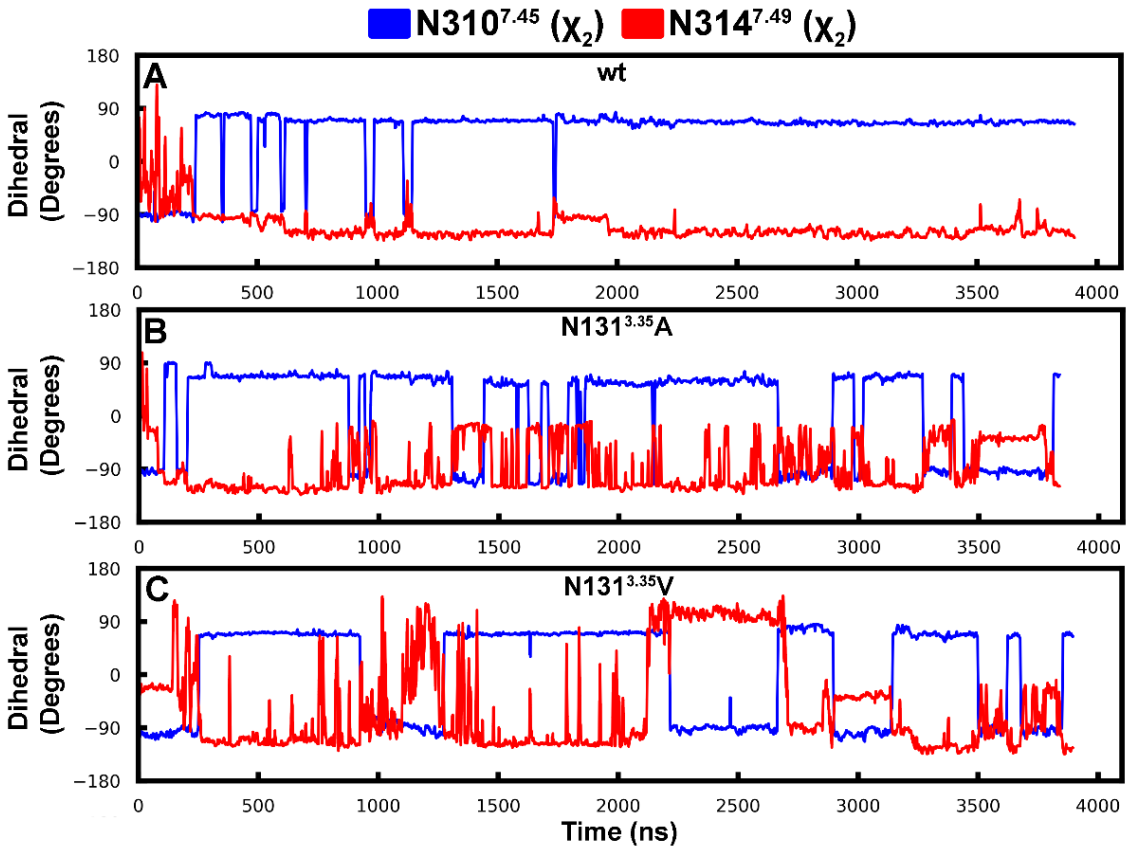

Figure 5-7: Effects of a neutral $D95^{2.50}$ and charged $D145^{3.49}$ upon the Na^+ binding pocket

The dihedral angle χ_2 of the $N310^{7.45}$ (blue) and the $N314^{7.49}$ (red) sidechains. Destabilisation of the Na^+ binding pocket upon the protonation of $D95^{2.50}$. For all trajectories see Appendix Figure 8-4.

Despite the rearrangement of the Na^+ binding pocket, these changes are not propagated into a fully activated conformation of the receptor. Interestingly, due to the increased flexibility of N314$^{7.49}$ the sidechain of Y318$^{7.53}$ displays an increased conformational variability (Figure 5-8). Throughout the simulations in which D95$^{2.50}$ is protonated, the sidechain of Y318$^{7.53}$ can occupy four main conformations: The inactive conformation in which the Y318$^{7.53}$ is locked in an upright conformation via a three way hydrogen bond between N67$^{1.50}$, D95$^{2.50}$ and Y318$^{7.53}$ mediated by a highly conserved water molecule (corresponding distance: ~8 Å, Figure 5-13, A). Upon N314$^{7.49}$ disrupting the previously described hydrogen bond network, an intermediary conformation is seen (corresponding to a distance of ~10 Å, Figure 5-13, B). Thirdly, a downward conformation is observed in which the sidechain faces towards the intracellular binding site. This conformation is stabilised by the Y318$^{7.53}$-OH group forming a hydrogen bond with the carboxyl group of N85$^{2.40}$, this conformation has also been reported for the intermediate active state of the A_{2A} receptor (PDB ID: 2YDV, (72))(corresponding distance: 16 Å, Figure 5-13, C). Fourthly, a horizontal conformation is observed, in which the sidechain of Y318$^{7.53}$ faces across the core of the receptor towards TM 3, similar to that reported in Chapter 4 and in the active crystal structure of the μ-OR (corresponding to a distance of 14 Å, Figure 5-13, D). Interestingly, the D(E)R$^{3.50}$Y motif displays fluctuations to the active state to a slightly greater degree within the N131$^{3.35}$ mutants. However, no movement to the fully activated conformation is seen.

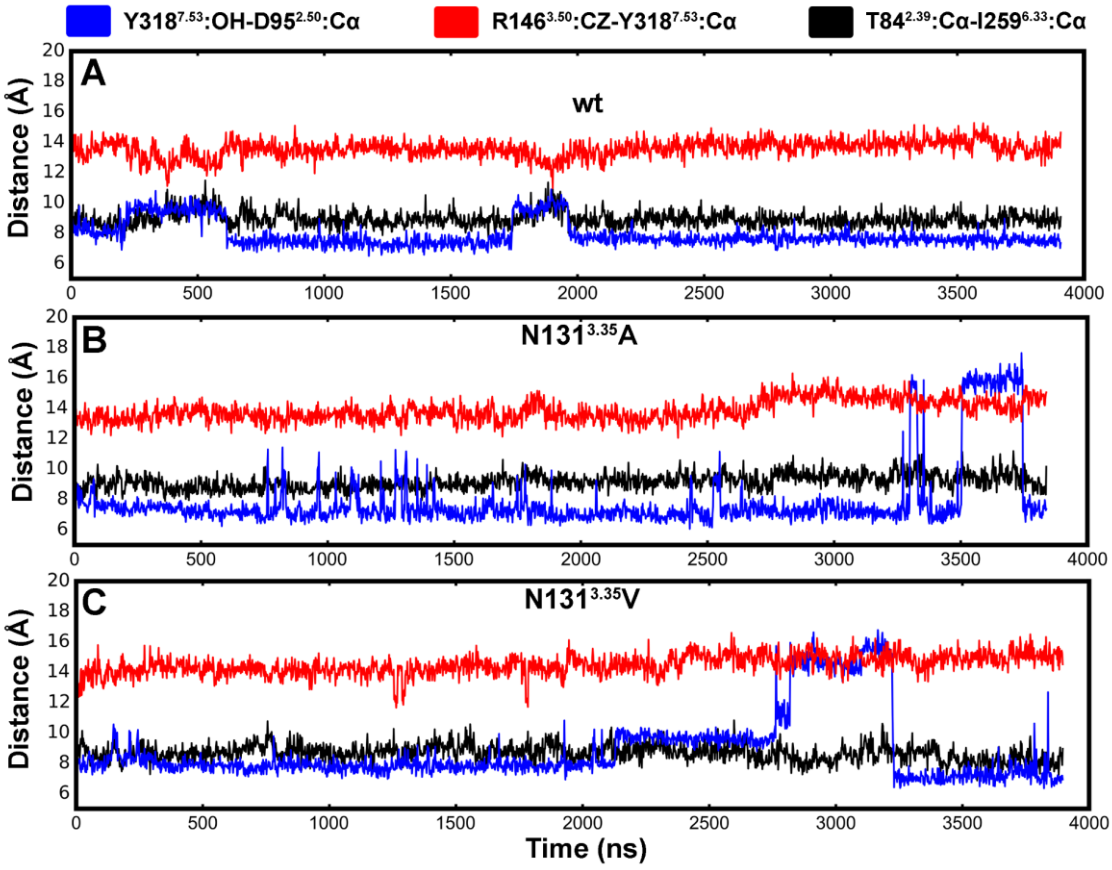

Figure 5-8: Activation criteria for the δ-OR with a neutral D95$^{2.50}$ and charged D145$^{3.49}$

The criteria for the activation of the δ-OR receptor. With a neutral D95$^{2.50}$, both the wt and two δ-OR mutants **(A-C)** do not fulfil the criteria for the active conformation. The protonation of D95$^{2.50}$ however

increases the conformational flexibility of Y318$^{7.53}$, in which the inactive, intermediate and downward conformation is observed. Shown is the distance between Y318$^{7.53}$-OH and D95$^{2.50}$-Cα (blue), R146$^{3.50}$-CZ and Y318$^{7.53}$-Cα (red), and T84-Cα and I259-Cα (black). For all trajectories see Appendix Figure 8-5.

5.2.3 Activation of δ-OR by the protonation of D95$^{2.50}$ and D145$^{3.49}$

The third ionisable residue within the δ-OR is part of the highly conserved D(E)R$^{3.50}$Y motif. The aspartate residue (D145$^{3.49}$) within this motif has been proposed to be responsible for pH-dependent activation (214, 215). Therefore, D145$^{3.49}$ in conjunction with D95$^{2.50}$ was modelled in a neutral state. Similar, to the previous section, I observed a destabilisation of the Na^+ binding site (Figure 5-9). Both, N310$^{7.45}$ and N314$^{7.49}$ display a greatly increased conformational freedom in comparison to the charged D95$^{2.50}$ simulations. In the majority of simulations, the sidechain of N310$^{7.45}$ exists in two predominant orientations as previously described, whilst the sidechain of N314$^{7.49}$ displays the same conformational variation as described in the previous section.

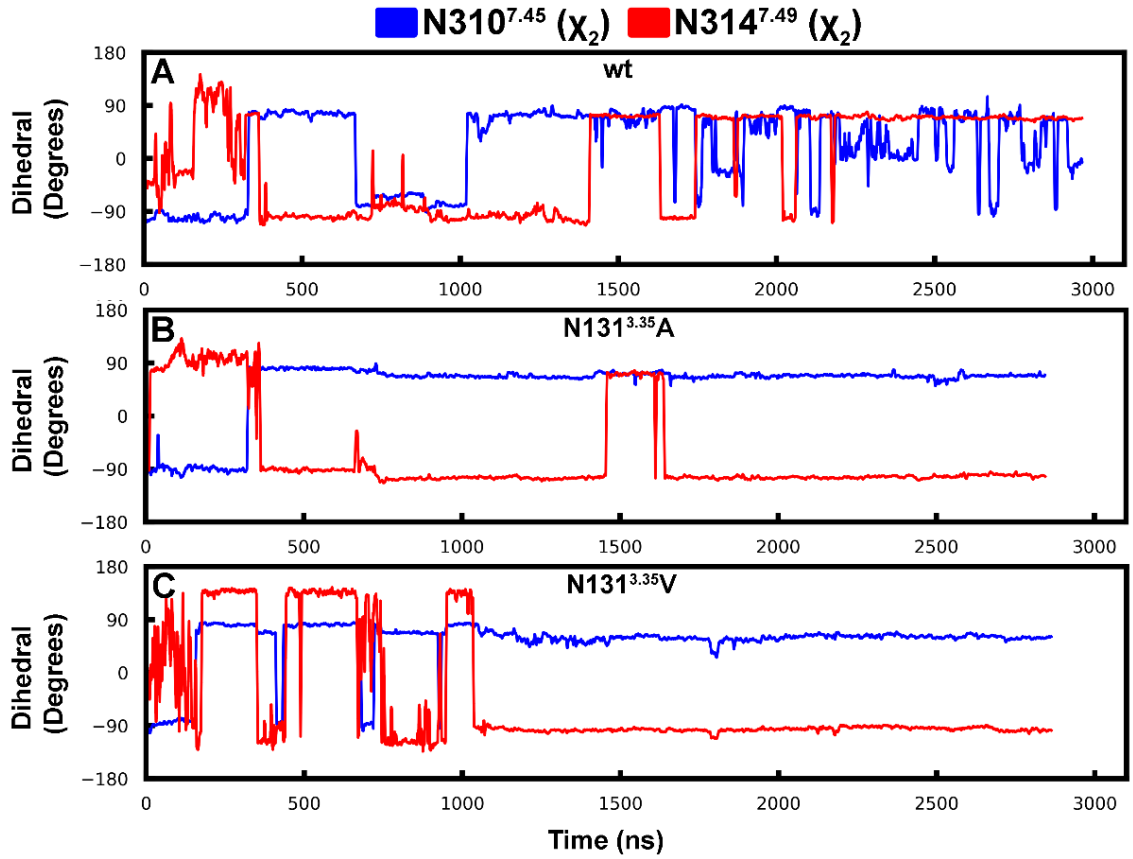

Figure 5-9: Effects of a neutral D95$^{2.50}$ and D145$^{3.49}$ upon the Na^+ binding pocket

The dihedral angle χ_2 of the N310$^{7.45}$ (blue) and the N314$^{7.49}$ (red) sidechains. Destabilisation of the Na^+ binding pocket upon the protonation of D95$^{2.50}$ and D145$^{3.49}$. For all trajectories see Appendix Figure 8-6.

In contrast to the previous sections, in the protonated state there are large-scale rearrangements of the receptors corresponding to activation. The movement towards the activated conformation occurs regardless to the mutation state of N131$^{3.35}$, with both the wt δ-OR and N131$^{3.35}$A mutant undergoing the full transition between states. The analysis of the doubly protonated receptor simulations display the fulfillment of all three activation criteria. The R146$^{3.50}$ sidechain displays an increased propensity to extend into the intracellular effector-binding site. The distance between the head group of R146$^{3.50}$ and Y318$^{7.53}$-Cα decreases from 14 Å to 8-10 Å (Figure 5-10). Interestingly, the movement of the D(E)R$^{3.50}$Y and NP$^{7.50}$xxY motif moving to the active conformation results in an increase in distance between TM 2 and 6. The distance between helices increases from ~8 Å to up to ~16 Å (Figure 5-10 A, B, Figure 5-11 D).

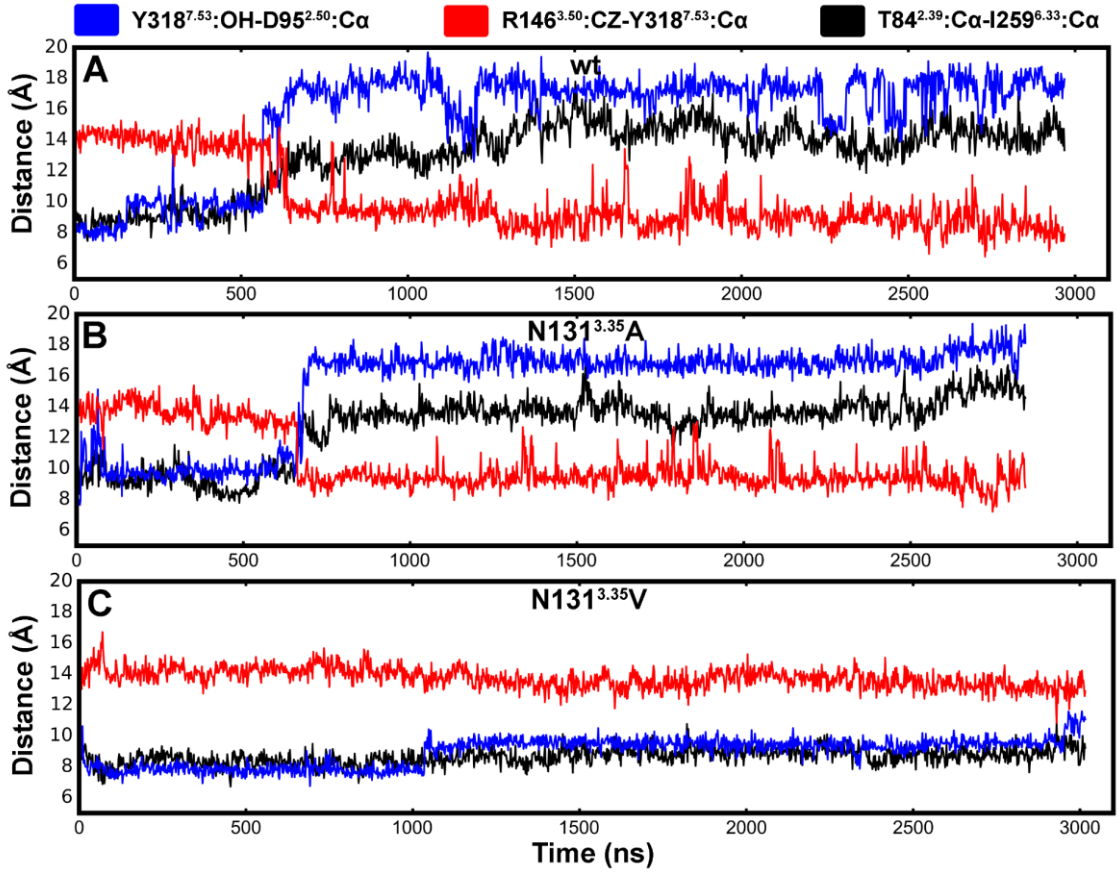

Figure 5-10: Activation criteria for the δ-OR with a neutral D95$^{2.50}$ and D145$^{3.49}$

The criteria for the activation of the δ-OR receptor. With a neutral D95$^{2.50}$ and D145$^{3.49}$, both the wt and N131$^{3.35}$A δ-OR mutant **(A-B)** fulfil the criteria for the active conformation. The protonation of D95$^{2.50}$ increases the conformational flexibility of Y318$^{7.53}$, in which all four conformations are observed. The R146$^{3.50}$ sidechain extends into the G-protein binding pocket, and a corresponding increase in distance between TM 2 and 6 is seen. Shown is the distance between Y318$^{7.53}$-OH and D95$^{2.50}$-Cα (blue), R146$^{3.50}$-CZ and Y318$^{7.53}$-Cα (red), and T84-Cα and I259-Cα (black). For all trajectories see Appendix Figure 8-7.

As previously described in Chapter 4 and ref. (69), the activation of the receptor leads to the formation of a hydrated channel connecting the Na^+ binding site to the intracellular bulk solution. The neutralisation of both D95$^{2.50}$ and D145$^{3.49}$ results in the widening of TM 2-6, breaking the hydrophobic layer and thus

allowing the ingress of water from the extracellular and intracellular solutions. The number of water molecules within the water channel increases from an average of 1.5 in the inactive states, in which the water molecules are stably bound. Whilst in the active receptor the number of water molecules increases to an average of 6.5 ± 2.5 and 6.4 ± 2.9 in the wt and N131$^{3.35}$A δ-OR active receptor, respectively (Figure 5-11)

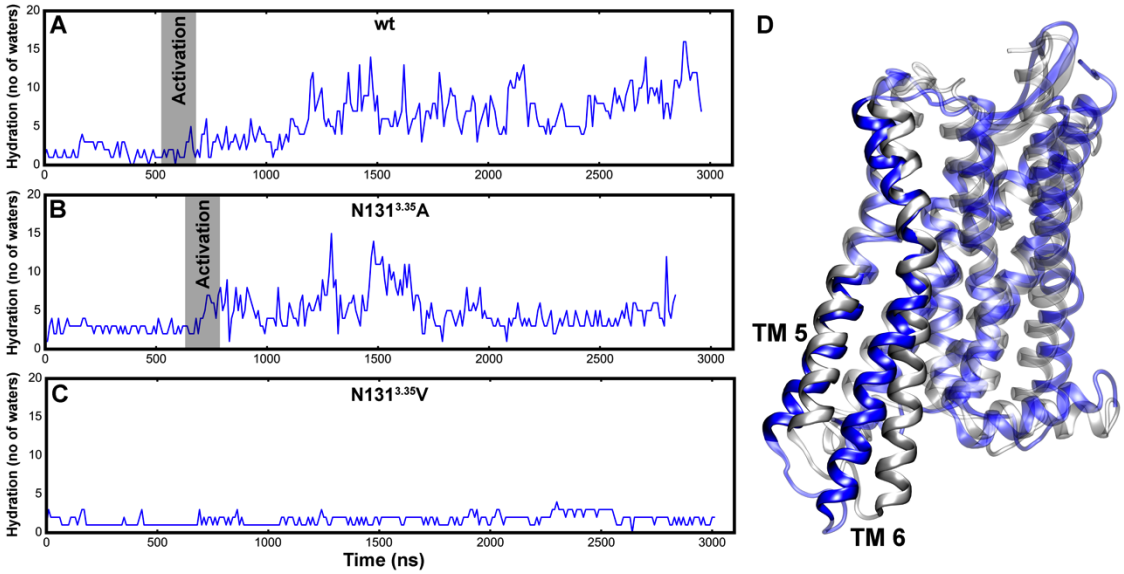

Figure 5-11: Hydration of the intracellular channel

The hydration of the hydrophobic layer upon δ-OR activation. **(A, B)** depict the increased hydration upon the activation of the receptor. The increased hydration level is linked to the conformational changes of the NP$^{7.50}$xxY and D(E)R$^{3.50}$Y motifs (Figure 5-10 A, B). **(C)** None of the N131$^{3.35}$V mutants moved to the active state, therefore depicted here is an example of the normal hydration of the non channel forming hydrophobic layer (~1.5 water molecules). The water molecules were counted every 10 ns, between a distance of Δz = -4Å from the D95$^{2.50}$ Cα atom and towards the intracellular with the z-coordinate of the R146$^{3.50}$ Cα. **(D)** Shown here is a comparison of the inactive (silver) and active (blue) conformations arising from the protonation of D95$^{2.50}$ and D145$^{3.49}$. The movements of TM 5 and 6 are highlighted here. For all trajectories see Appendix Figure 8-8.

5.3 Conclusion

The principal role of GPCRs is the transmission of extracellular information through the receptor to the cytoplasm, and the subsequent activation of intracellular effectors (34, 57, 192). The activation process of the receptor is known to involve a range of conformational changes, from large scale movements such as the rearrangement of TM 5, 6, and 7 on the intracellular side to small sidechain rearrangements in the microswitches (130, 193–195). It has long been known that the *Rhodopsin* GPCR family is sensitive to a range of environmental factors, including V_m, pH, Na^+ ions (see section 1.5). The effects of pH upon the upon basal signalling and agonist induced activation in the β_2AR and rhodopsin have been well described (96, 215). However, whilst the majority of ionisable residues in the *Rhodopsin* GPCR family are solvent

exposed and are therefore likely to have a pK_a far away 7. In contrast, residues buried within the TM section have an up shifted pK_a and can therefore titrate upon smaller deviations from pH 7. The *Rhodopsin* GPCR family contains three acidic residues within the transmembrane domain: $D^{2.50}$, $D^{3.32}$ and $D^{3.49}$. Of these three, only the protonation of $D^{2.50}$ and $D^{3.49}$ has been studied (96, 216, 217). However, mutation of these residues severely disrupts the signalling of GPCRs, making experimental results difficult to interpret (see section 1.4).

In Chapter 3, I demonstrated that the experimentally measured gating charge is likely to arise from the transfer of either a proton or the allosteric Na^+ ion to or from the receptor. In Chapter 4, I showed that the protonation state of $D^{2.50}$ is strongly modulated by the location of the Na^+ ion. The µs timescale atomistic simulations of the wt δ-OR as well as the two δ-OR mutants $N131^{3.35}A$ and $N131^{3.35}V$ demonstrate the key role of $D^{2.50}$ and $D^{3.49}$ protonation states in the activation of the δ-OR. The results demonstrated here showing the conformational shift of the receptor to the active state upon the protonation of key residues (Figure 5-12), is in excellent agreement with experiments where the basal signalling is increased upon lowering the pH (96, 214). Due to the conservation of the residue $D^{2.50}$ in the Na^+ binding pocket, and of an acidic residue within the $D(E)R^{3.50}Y$ motif, the proposed protonation pattern is highly likely to be applicable to the rest of the *Rhodopsin* GPCR family.

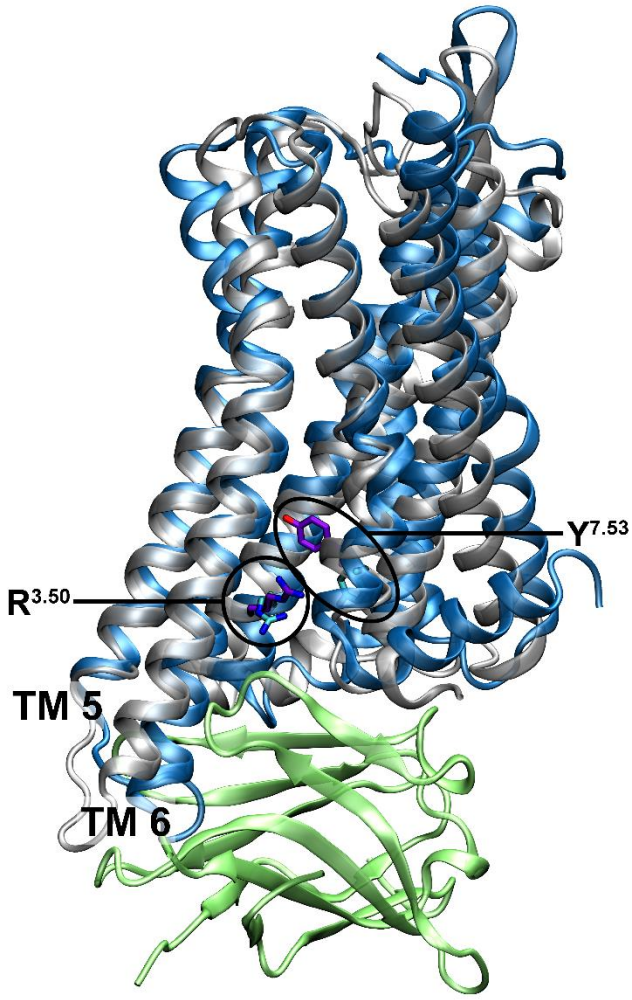

Figure 5-12: Comparison of the μ-Opioid crystal structure and the active MD δ-Opioid receptors
Shown here is a comparison of the active crystal of the μ-OR (silver) with a nanobody bound (green) and active δ-OR (blue) conformations arising from the protonation of $D95^{2.50}$ and $D145^{3.49}$. The sidechains $R^{3.50}$ and $Y^{7.53}$ are depicted in both the μ-OR (violet) and δ-OR (cyan).

Interestingly, I did not see any significant difference between the wt δ-OR and the $N131^{3.35}A$ and $N131^{3.35}V$ δ-OR mutants. With the exception of the Na^+ bound receptors, in which the Na^+ binding pocket displayed increasing destabilisation upon the mutation of $N131^{3.35}$. Though the mutant δ-ORs did display some increased mobility within the $D(E)R^{3.50}Y$ motif regardless of the protonation states when compared to the wt receptor, all motions were below the threshold for activation (Fig 11-15). The changes to the receptor may be too subtle for the simulations to detect, however these simulation can be mined for more detailed differences. For a continuation of this work, it would be interesting to test the sole protonation of $D145^{3.49}$ as well as any changes in the TM 3 in which the mutant is situated. To this end, the conclusions presented here are a common mechanism across all three δ-OR systems.

5.3.1 Signal propagation from Na^+ binding site to the G-protein binding site

The sequential protonation of $D95^{2.50}$ within the Na^+ binding site and $D145^{3.49}$ in the D(E)$R^{3.50}$Y motif demonstrates how small changes in the receptor can propagate into large scale conformational changes (Figure 5-13). The initial protonation of $D95^{2.50}$ modulates the shape of the Na^+ binding pocket, in particular the tight interaction of $D95^{2.50}$ and $N314^{7.49}$ (Figure 5-13 A). The breaking of the hydrogen bond between $D95^{2.50}$ and $N314^{7.49}$, consequently allows for the disruption of the three-way hydrogen bond between $N67^{1.50}$, $D95^{2.50}$ and $Y318^{7.53}$ (Figure 5-13 B), which is mediated by a highly conserved water molecule (Figure 5-3). The importance of this water molecule is reflected in its presence in nearly all crystal structures of the *Rhodopsin* GPCR family irrespective of their activation state (68). The disruption of the water-mediated hydrogen bond within the Na^+ binding pocket allows two possible active sidechain conformations of $Y318^{7.53}$. The first is the rotation into a downward conformation interacting with the intracellular end of TM 2 ($N85^{2.40}$). This downward conformation is likely seen only in the absence of the intracellular binding partner. The second is the formation of a horizontal conformation facing TM 5 (Figure 5-13 D). This conformation is highly similar to that reported in the active μ-OR crystal structure (PDB ID: 5C1M, (190)). The sidechain of $Y233^{5.58}$ was proposed to stabilise the active conformation by facing the core of the receptor and coordinating with the horizontal conformation of $Y318^{7.53}$ (see section 1.4.3). However, throughout all simulations regardless of the protonation states and mutations, the sidechain of $Y233^{5.58}$ adopts two predominant conformations an inward pose facing the core of the receptor and an outward facing conformation.

The protonation of $D145^{3.49}$ in conjunction with the protonation of $D95^{2.50}$ results in the activation of the D(E)$R^{3.50}$Y motif. The extension of the $R146^{3.50}$ towards TM 7, aids in the hydration of the hydrophobic layer and the formation of the water channel seen within Chapter 4. This subsequently results in the outward conformational shift of TM 5 and 6 seen within all active crystal structures.

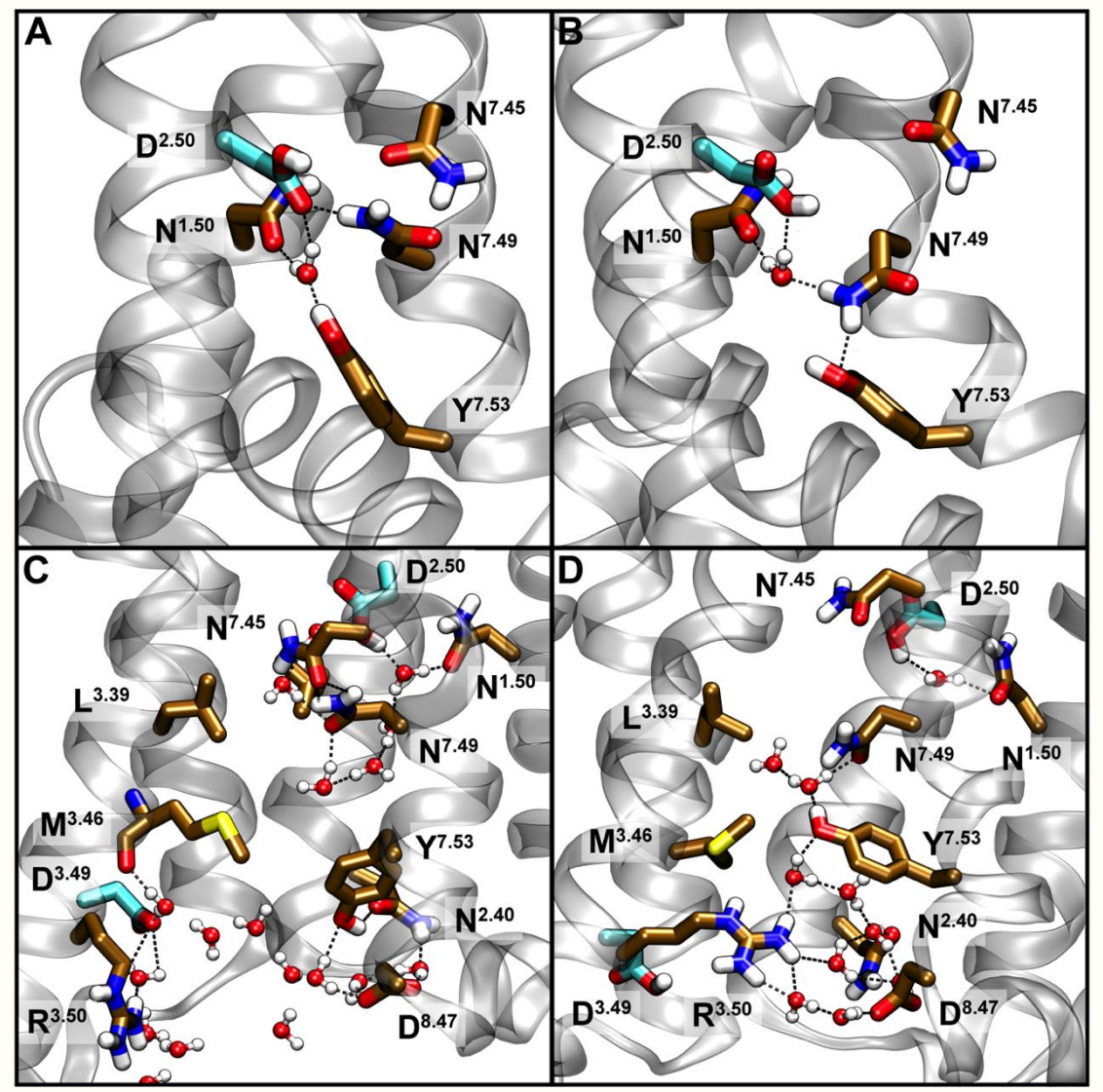

Figure 5-13: Propagation of activation arising from protonation changes

The sequential activation of the δ-OR by the protonation of D95$^{2.50}$ and D145$^{3.49}$. **(A)** Displays the initial conformation of the Na^+ binding pocket and Y318$^{7.53}$ in the inactive form. **(B)** The intermediary conformation of the Y318$^{7.53}$, in which the N314$^{7.49}$ has displaced the hydrogen bond between Y318$^{7.53}$ and the conserved water. **(C)** The Y318$^{7.53}$ in a downward conformation coordinated with N85$^{2.40}$. **(D)** The horizontal conformation of Y318$^{7.53}$ sidechain, demonstrated here is the increased hydration of the hydrophobic layer. It should be noted that in **A** and **B** the side chain of N310$^{7.45}$ is in the initial orientation (distance = 2 Å), in panel **C** and **D** in the orientation is now inverted (distance = -2 Å). The sidechains of the protonatable residues D95$^{2.50}$ and D145$^{3.49}$ are depicted in cyan. All pertinent hydrogen bonds are depicted by dashed black lines.

These simulations demonstrate the importance of the internal hydration and hydrogen-bonding pattern within the receptor (80). The results suggest a mechanism for the Na^+ free activation of the δ-OR, in which the protonation of D95$^{2.50}$ and D145$^{3.49}$ play an intrinsic role. Protonation induced conformational changes are also in agreement with the V_m induced changes seen by experimental studies (184). The pK_a of D$^{2.50}$

and $D^{3.32}$ was shown to ~10-11 under equilibrium conditions (Chapter 4). As both of these residues are located in the transmembrane domain, their pK_a is highly likely to be strongly modulated by changes in the V_m (181). These acidic residues within the transmembrane domain are likely to be protonated in a hyperpolarised potential, however, upon depolarisation of the membrane the pK_a of these residues is likely to be downshifted enough to become deprotonated. As I have previously described, this is sufficient to cause the receptor to undergo significant conformational changes within the highly conserved motifs and large-scale movement of TM 5 and 6.

Chapter 6. Closing remarks

6.1 Thesis summary

The overall aim of this thesis was to study the allosteric effects of the internally bound Na^+ ion, protonation ($D^{3.32}$, $D^{2.50}$ and $D^{3.49}$) and V_m upon the *Rhodopsin* GPCR family. This thesis is separated into three main results; the first describes the movement of either a Na^+ ion or proton from the Na^+ binding site to the extracellular solution. The movement of the cation was demonstrated to be possible under physiological depolarised V_m conditions. The gating charge arising from this movement is in excellent agreement with previous experimentally recorded gating charges (Chapter 3). Therefore, my findings offer mechanistic insight into GPCR voltage dependence.

The active crystal structures of the *Rhodopsin* GPCR family display a collapsed Na^+ ion binding site. The resulting conformation of the pocket is thought to preclude the binding of the Na^+ ion. Here, I demonstrate that it is possible for the Na^+ ion to pass through the hydrophobic layer to the cytoplasm. I show by Potential of Mean Force calculations that the synergistic physiological driving force of the Na^+ concentration gradient and hyperpolarised V_m is sufficient to drive ion permeation. The Na^+ ion was found to be strongly coupled to the protonation state of the key Na^+ binding residue $D^{2.50}$. Small movements of the Na^+ ion resulted in a pK_a shift of ~6 units. Following the protonation of $D^{2.50}$, the passage of the Na^+ to the cytoplasm was shown to be near barrier free (Chapter 4).

Point mutations within the Na^+ binding site have been demonstrated to drastically alter the receptors signalling pattern. In the δ-OR, I studied the effects of the constitutively active mutants $N131^{3.35}A$ and $N131^{3.35}V$ upon the receptor conformation. Concurrently, I sequentially changed the protonation states of the $D95^{2.50}$ and $D145^{3.49}$ in the Na^+ binding site and $D(E)R^{3.50}Y$, respectively. The neutralisation of $D95^{2.50}$ resulted in the increased flexibility of the $NP^{7.50}xxY$ motif, and the subsequent neutralisation of $D145^{3.49}$ leads to the large-scale conformational change of the receptor from the inactive to active state. Here, I proposed a mechanism in which the protonation of $D95^{2.50}$ is propagated into the activation of the receptor (Chapter 5).

6.2 Revised concepts

The original interpretation of each Chapter's results has evolved with additional information. Within Chapter 3, I demonstrated that the movement of a cation from the Na^+ binding site to the extracellular solution gives rise to a gating charge (0.53 e) in excellent agreement to the previous experimentally measured the gating charges (0.55 - 0.85 e)(125). In Chapter 3, I originally considered that the gating charge arose from the translocation of the Na^+ ion due to the concentration of Na^+ within the extracellular solution. However, the inclusion of the pK_a calculations done in Chapter 4, demonstrating that V_m induced protonation and deprotonation of $D^{2.50}$ is highly likely. The probability of the gating charge arising from a protonation change of $D^{2.50}$ is increased by the use of monovalent cation free solutions in the experiments.

The mutation of $D^{2.50}$ abolishes the gating charge in the *Rhodopsin* GPCR family. This is in agreement with our simulations that the movement of a Na^+ ion or proton from the Na^+ binding site gives rise to the gating charge.

Although the mutation of $D^{2.50}$ to an asparagine abolishes the gating current in the m1 muscarinic receptor (M1R), its ligand binding affinity is still modulated by voltage (218). In Chapter 4, the pK_a calculation of the aspartate that is required for binding of the muscarinic ligands ($D^{3.32}$), reveals that in the apo form this residue is in a protonated state, whilst upon ligand binding the pK_a is lowered to ~7. The aspartate is within the transmembrane electric field, and therefore it is possible for the pK_a of $D^{3.32}$ to be modulated by V_m. This modulation could give rise to the ligand dependent voltage effects seen. The sensitivity of $D^{3.32}$ to the physiological environment demonstrated by its sensitivity to extracellular pH. In the β_2AR, the basal signalling of the receptor increases, whilst the agonist binding affinity decreases upon the lowering of the extracellular pH from 8 to 6.5 (96). This is likely due to the protonation of $D^{3.32}$ preventing the negative charge of the aspartate from stabilising the positively charged ligand, whilst simultaneously, increasing the likelihood of the protonation of $D^{2.50}$ and thereby stabilising the active state of the receptor. In Chapter 5, I demonstrate that the receptor can shift to the active state upon the protonation of $D^{2.50}$ and $D^{3.49}$. This also is in excellent agreement with the pH sensitivity of β_2AR (96). The protonation-induced conformational change similarly is in agreement with the V_m induced conformation change of the receptor.

6.3 Future directions

The current simulations provide a potential explanation for the regulation of GPCRs by pH, V_m and Na^+ ions. However, the continuation of this work can be undertaken on a two-pronged approach, a computational and experimental.

To be able to include the V_m into the pK_a calculations would enable a clearer insight into the role of $D^{3.32}$ in ligand dependent voltage sensitivity. This would also be of benefit to studying the protonation states of $D^{2.50}$ and $D^{3.49}$. The inclusion of quantum mechanical/molecular mechanics (QM/MM) simulations would allow for a more in depth study of the role of proton transfer within *Rhodopsin* GPCRs. Whilst the work presented within this thesis is focused predominantly on the Na^+ and protonation states of key acidic residues, a comprehensive study on the Na^+ binding site would be enlightening, in particular; A comparison of the hydrogen bond network between the inactive and active structures. The interaction pattern between water molecules and key amino acids could be elucidated by further mutational studies on the residues of the Na^+ binding pocket, in particular positions 2.50, 3.35, 7.45 and 7.49.

There are multiple experiments, which can be undertaken to study the V_m related allosteric effects arising from changes in protonation state. The majority of voltage allostery studies have been performed in receptors containing an aspartate at position 3.32. Therefore, to test the role of a protonatable residue on the ligand dependent voltage effects, experiments should to be undertaken using receptors without an aspartate at position 3.32 or the use of ligands, which are not dependent on this residue for binding. The

characteristics of the gating charges in GPCRs should be modulated by changes in the extracellular pH, and therefore it would be interesting to see the gating charges arising from an altered pH and the receptor mutants previously described.

Chapter 7. Bibliography

1. Kolakowski LFJ (1994) GCRDb: a G-protein-coupled receptor database. *Receptors Channels* 2(1):1–7.
2. Fredriksson R, Lagerström MC, Lundin L-G, Schiöth HB (2003) The G-protein-coupled receptors in the human genome form five main families. Phylogenetic analysis, paralogon groups, and fingerprints. *Mol Pharmacol* 63(6):1256–72.
3. Gloriam DE, Fredriksson R, Schiöth HB (2007) The G protein-coupled receptor subset of the rat genome. *BMC Genomics* 8(1):338.
4. Lagerstrom MC, Schioth HB (2008) Structural diversity of G protein-coupled receptors and significance for drug discovery. *Nat Rev Drug Discov* 7(April):339–357.
5. Grauschopf U, et al. (2000) The N-terminal fragment of human parathyroid hormone receptor 1 constitutes a hormone binding domain and reveals a distinct disulfide pattern. *Biochemistry* 39(30):8878–8887.
6. Hollenstein K, et al. (2014) Insights into the structure of class B GPCRs. *Trends Pharmacol Sci* 35(1):12–22.
7. Bjarnadóttir TK, et al. (2004) The human and mouse repertoire of the adhesion family of G-protein-coupled receptors. *Genomics* 84(1):23–33.
8. Hamann J, et al. (2015) International Union of Basic and Clinical Pharmacology. XCIV. Adhesion G Protein-Coupled Receptors. *Pharmacol Rev* 67(2):338–367.
9. Chun L, Zhang W, Liu J (2012) Structure and ligand recognition of class C GPCRs. *Acta Pharmacol Sin* 33(3):312–323.
10. Huang H-C, Klein PS (2004) The Frizzled family: receptors for multiple signal transduction pathways. *Genome Biol* 5(7):234.
11. Salinas PC (2012) Wnt signaling in the vertebrate central nervous system: From axon guidance to synaptic function. *Cold Spring Harb Perspect Biol* 4(2). doi:10.1101/cshperspect.a008003.
12. Ranjan R, Dwivedi H, Baidya M, Kumar M, Shukla AK (2017) Novel Structural Insights into GPCR-β-Arrestin Interaction and Signaling. *Trends Cell Biol* xx:1–12.
13. Luttrell LM (2014) Minireview: more than just a hammer: ligand “bias” and pharmaceutical discovery. *Mol Endocrinol* 28(3):281–94.
14. Isberg V, et al. (2015) Generic GPCR residue numbers – aligning topology maps while minding the gaps. *Trends Pharmacol Sci* 36(1):22–31.
15. Simon MI, Strathmann MP, Gautam N (1991) Diversity of G proteins in signal transduction. *Science* 252(5007):802–8.
16. Lambright DG, et al. (1994) Structural determinants for activation of the α-subunit of a heterotrimeric G protein. *Nature* 369(6482):621–628.
17. Mixon MB, et al. (1995) Tertiary and Quaternary Structural Changes in Gialpha Induced by GTP Hydrolysis. *Science (80-)* 270(5238):954–960.
18. Coleman DE, et al. (1994) Structures of active conformations of Gia1 and the mechanism of GTP hydrolysis. *Science (80-)* 265(5177):1405–1412.

19. Neer EJ (1995) Heterotrimeric G proteins: Organizers of transmembrane signals. *Cell* 80(2):249–257.
20. Carpenter B, Nehmé R, Warne T, Leslie AGW, Tate CG (2016) Structure of the adenosine A2A receptor bound to an engineered G protein. *Nature*:1–15.
21. Moreira IS (2014) Structural features of the G-protein/GPCR interactions. *Biochim Biophys Acta - Gen Subj* 1840(1):16–33.
22. Lin Y, Smrcka A V (2011) Understanding Molecular Recognition by G protein beta gamma Subunits on the Path to Pharmacological Targeting. *Mol Pharmacol* 80(4):551–557.
23. Higgins JB, Casey PJ (1996) The role of prenylation in G-protein assembly and function. *Cell Signal* 8(6):433–437.
24. Neer EJ (1995) Heterotrimeric G proteins: Organizers of transmembrane signals. *Cell* 80(2):249–257.
25. Khan SM, et al. (2013) The expanding roles of Gβγ subunits in G protein-coupled receptor signaling and drug action. *Pharmacol Rev* 65(2):545–577.
26. Tolkovsky a M, Levitzki a (1978) Mode of coupling between the beta-adrenergic receptor and adenylate cyclase in turkey erythrocytes. *Biochemistry* 17(18):3795.
27. Neubig RR, Gantzos RD, Thomsen WJ (1988) Mechanism of agonist and antagonist binding to alpha 2 adrenergic receptors: evidence for a precoupled receptor-guanine nucleotide protein complex. *Biochemistry* 27(7):2374–84.
28. Sungkaworn T, et al. (2017) Single-molecule imaging reveals receptor–G protein interactions at cell surface hot spots. *Nature*. doi:10.1038/nature24264.
29. Lohse MJ, Hoffmann C (2014) Arrestin Interactions with G Protein-Coupled Receptors, pp 15–56.
30. Benovic J (1996) Beta-arrestin acts as a clathrin adaptor in endocytosis of the beta2-adrenergic receptor. *Nature*:447–450.
31. Ferguson SSG, et al. (1996) Role of beta-Arrestin in Mediating Agonist-Promoted G Protein-Coupled Receptor Internalization. *Science (80-)* 271(5247):363–366.
32. Shenoy SK, Lefkowitz RJ (2011) β-arrestin-mediated receptor trafficking and signal transduction. *Trends Pharmacol Sci* 32(9):521–533.
33. Han M, Gurevich V V, Vishnivetskiy SA, Sigler PB, Schubert C (2001) Crystal structure of beta-arrestin at 1.9 A: possible mechanism of receptor binding and membrane Translocation. *Structure* 9(9):869–880.
34. Skieterska K, Rondou P, Van Craenenbroeck K (2017) Regulation of G Protein-Coupled Receptors by Ubiquitination. *Int J Mol Sci* 18(5):923.
35. Kopecky SL (2006) Effect of Beta Blockers, Particularly Carvedilol, on Reducing the Risk of Events After Acute Myocardial Infarction. *Am J Cardiol* 98(8):1115–1119.
36. Poole-Wilson PA, et al. (2003) Comparison of carvedilol and metoprolol on clinical outcomes in patients with chronic heart failure in the Carvedilol Or Metoprolol European Trial (COMET): randomised controlled trial. *Lancet* 362(9377):7–13.
37. Alonso N, et al. (2015) Physiological implications of biased signaling at histamine H2 receptors.

Front Pharmacol 6(MAR):1–9.

38. Calebiro D, et al. (2009) Persistent cAMP-signals triggered by internalized G-protein-coupled receptors. *PLoS Biol* 7(8). doi:10.1371/journal.pbio.1000172.
39. Ferrandon S, et al. (2009) Sustained cyclic AMP production by parathyroid hormone receptor endocytosis. *Nat Chem Biol* 5(10):734–742.
40. Feinstein TN, et al. (2013) Noncanonical control of vasopressin receptor type 2 signaling by retromer and arrestin. *J Biol Chem* 288(39):27849–27860.
41. Irannejad R, et al. (2013) Conformational biosensors reveal GPCR signalling from endosomes. *Nature* 495(7442):534–538.
42. Kotowski SJ, Hopf FW, Seif T, Bonci A, von Zastrow M (2011) Endocytosis Promotes Rapid Dopaminergic Signaling. *Neuron* 71(2):278–290.
43. Vilardaga J-P, Jean-Alphonse FG, Gardella TJ (2014) Endosomal generation of cAMP in GPCR signaling. *Nat Chem Biol* 10(9):700–706.
44. Staus DP, et al. (2016) Allosteric nanobodies reveal the dynamic range and diverse mechanisms of G-protein-coupled receptor activation. *Nature* 535(7612):448–452.
45. Thompson GL, et al. (2016) Systematic analysis of factors influencing observations of biased agonism at the mu-opioid receptor. *Biochem Pharmacol* 113:70–87.
46. Benredjem B, Dallaire P, Pineyro G (2017) Analyzing biased responses of GPCR ligands. *Curr Opin Pharmacol* 32:71–76.
47. Pupo AS, et al. (2016) Recent updates on GPCR biased agonism. *Pharmacol Res* 112:49–57.
48. Chen X, et al. (2013) Structure–Activity Relationships and Discovery of a G Protein Biased μ Opioid Receptor Ligand, [(3-Methoxythiophen-2-yl)methyl]({2-[(9 R)-9-(pyridin-2-yl)-6-oxaspiro-[4.5]decan-9-yl]ethyl})amine (TRV130), for the Treatment of Acute Severe Pain. *J Med Chem* 56(20):8019–8031.
49. Dror RO, et al. (2011) Pathway and mechanism of drug binding to G-protein-coupled receptors. *Proc Natl Acad Sci* 108(32):13118–13123.
50. Woolley MJ, Conner AC (2016) Understanding the common themes and diverse roles of the second extracellular loop (ECL2) of the GPCR super-family. *Mol Cell Endocrinol* 449:3–11.
51. Ballesteros JA, Weinstein H (1995) Integrated methods for the construction of three-dimensional models and computational probing of structure-function relations in G protein-coupled receptors. *Methods Neurosci* 25(C):366–428.
52. Venkatakrishnan a J, et al. (2013) Molecular signatures of G-protein-coupled receptors. *Nature* 494(7436):185–94.
53. Suku E, Giorgetti A (2017) Common evolutionary binding mode of rhodopsin-like GPCRs: Insights from structural bioinformatics. *AIMS Biophys* 4(4):543–556.
54. Masuho I, et al. (2015) Distinct profiles of functional discrimination among G proteins determine the actions of G protein-coupled receptors. *Sci Signal* 8(405):ra123-ra123.
55. Flock T, et al. (2017) Selectivity determinants of GPCR–G-protein binding. *Nature* 545(7654):317–322.
56. Schwartz TW, Rosenkilde MM (1996) Is there a “lock” for all agonist “keys” in 7TM receptors?

Trends Pharmacol Sci 17(6):213–216.

57. Pierce KL, Premont RT, Lefkowitz RJ (2002) Seven-transmembrane receptors. *Nat Rev Mol Cell Biol* 3(September):639–650.
58. Schwartz TW, Frimurer TM, Holst B, Rosenkilde MM, Elling CE (2006) Molecular Mechanism of 7Tm Receptor Activation—a Global Toggle Switch Model. *Annu Rev Pharmacol Toxicol* 46(1):481–519.
59. Crocker E, et al. (2006) Location of Trp265 in metarhodopsin II: implications for the activation mechanism of the visual receptor rhodopsin. *J Mol Biol* 357(1):163–172.
60. Shi L, et al. (2002) β2 adrenergic receptor activation: Modulation of the proline kink in transmembrane 6 by a rotamer toggle switch. *J Biol Chem* 277(43):40989–40996.
61. Stoddart LA, Kellam B, Briddon SJ, Hill SJ (2014) Effect of a toggle switch mutation in TM6 of the human adenosine A 3 receptor on Gi protein-dependent signalling and Gi-independent receptor internalization. *Br J Pharmacol* 171(16):3827–3844.
62. Scheerer P, et al. (2008) Crystal structure of opsin in its G-protein-interacting conformation. *Nature* 455(7212):497–502.
63. Katritch V, Cherezov V, Stevens RC (2013) Structure-function of the G protein-coupled receptor superfamily. *Annu Rev Pharmacol Toxicol* 53:531–56.
64. Liu W, et al. (2012) Structural basis for allosteric regulation of GPCRs by sodium ions. *Science* 337(6091):232–6.
65. Fenalti G, et al. (2014) Molecular control of δ-opioid receptor signalling. *Nature* 506(7487):191–196.
66. Miller-Gallacher JL, et al. (2014) The 2.1 Å Resolution Structure of Cyanopindolol-Bound β1-Adrenoceptor Identifies an Intramembrane Na^+ Ion that Stabilises the Ligand-Free Receptor. *PLoS One* 9(3):e92727.
67. Zhang C, et al. (2012) High-resolution crystal structure of human protease-activated receptor 1. *Nature* 492(7429):387–92.
68. Katritch V, et al. (2014) Allosteric sodium in class A GPCR signaling. *Trends Biochem Sci* 39(5):233–244.
69. Yuan S, Filipek S, Palczewski K, Vogel H (2014) Activation of G-protein-coupled receptors correlates with the formation of a continuous internal water pathway. *Nat Commun* 5(May):4733.
70. Vickery ON, Machtens J-P, Tamburrino G, Seeliger D, Zachariae U (2016) Structural Mechanisms of Voltage Sensing in G Protein-Coupled Receptors. *Structure* 24(6):997–1007.
71. Heitman LH, Ye K, Oosterom J, Ijzerman AP (2008) Amiloride derivatives and a nonpeptidic antagonist bind at two distinct allosteric sites in the human gonadotropin-releasing hormone receptor. *Mol Pharmacol* 73(6):1808–1815.
72. Lebon G, et al. (2011) Agonist-bound adenosine A2A receptor structures reveal common features of GPCR activation. *Nature* 474(7352):521–525.
73. Rosenbaum DM, et al. (2011) Structure and function of an irreversible agonist-β(2) adrenoceptor complex. *Nature* 469(7329):236–40.
74. Rasmussen SGF, et al. (2011) Structure of a nanobody-stabilized active state of the β(2)

adrenoceptor. *Nature* 469(7329):175–180.

75. Li B, et al. (2005) Random mutagenesis of the M3 muscarinic acetylcholine receptor expressed in yeast: Identification of second-site mutations that restore function to a coupling-deficient mutant M3 receptor. *J Biol Chem* 280(7):5664–5675.
76. Warne T, Serrano-Vega MJ, Tate CG, Schertler GFX (2009) Development and crystallization of a minimal thermostabilised G protein-coupled receptor. *Protein Expr Purif* 65(2):204–213.
77. Rasmussen SGF, et al. (2007) Crystal structure of the human β2 adrenergic G-protein-coupled receptor. *Nature* 450(7168):383–387.
78. Rosenbaum DM, et al. (2007) GPCR Engineering Yields High-Resolution Structural Insights into 2-Adrenergic Receptor Function. *Science (80-)* 318(5854):1266–1273.
79. Warne T, et al. (2008) Structure of a β1-adrenergic G-protein-coupled receptor. *Nature* 454(7203):486–491.
80. Isom DG, Dohlman HG (2015) Buried ionizable networks are an ancient hallmark of G protein-coupled receptor activation. *Proc Natl Acad Sci* 2015:201417888.
81. Proulx CD, et al. (2008) Mutational Analysis of the Conserved Asp 2 . 50 and ERY Motif Reveals Signaling Bias of the Urotensin II Receptor. *Mol Pharmacol* 74(3):552–561.
82. Changeux J-P (2012) Allostery and the Monod-Wyman-Changeux Model After 50 Years. *Annu Rev Biophys* 41(1):103–133.
83. DeVree BT, et al. (2016) Allosteric coupling from G protein to the agonist-binding pocket in GPCRs. *Nature* 535(7610):182–6.
84. Lodish H, Berk A, Zipursky L, Baltimore D (2000) Molecular Cell Biology (4th edition) New York, NY, 2000, ISBN 0-7167-3136-3. *Biochem Mol Biol Educ* 29:Section 1.2The Molecules of Life.
85. Lombard J (2014) Once upon a time the cell membranes: 175 years of cell boundary research. *Biol Direct* 9(1):32.
86. Stansfeld PJ, Sansom MSP (2011) Molecular Simulation Approaches to Membrane Proteins. *Struct Des* 19(11):1562–1572.
87. Hedger G, Sansom MSP (2017) Lipid Interaction Sites on Channels, Transporters and Receptors: Recent Insights from Molecular Dynamics Simulations. 1858(10):2390–2400.
88. Fahy E, et al. (2009) Update of the LIPID MAPS comprehensive classification system for lipids. *J Lipid Res* 50(Supplement):S9–S14.
89. van Meer G, Voelker DR, Feigenson GW (2008) Membrane lipids: where they are and how they behave. *Nat Rev Mol Cell Biol* 9(2):112–124.
90. Hanson MA, et al. (2008) A Specific Cholesterol Binding Site Is Established by the 2.8 ?? Structure of the Human ??2-Adrenergic Receptor. *Structure* 16(6):897–905.
91. Oates J, Watts A (2011) Uncovering the intimate relationship between lipids, cholesterol and GPCR activation. *Curr Opin Struct Biol* 21(6):802–807.
92. Paila YD, Chattopadhyay A (2010) Membrane cholesterol in the function and organization of g-protein coupled receptors. *Subcell Biochem* 51:439–466.
93. Dawaliby R, et al. (2015) Allosteric regulation of G protein–coupled receptor activity by

phospholipids. *Nat Chem Biol* 12(1):35–39.

94. Spahn V, et al. (2017) A nontoxic pain killer designed by modeling of pathological receptor conformations. *Science (80-)* 355(6328):966–969.
95. Ye L, Van Eps N, Zimmer M, Ernst OP, Scott Prosser R (2016) Activation of the A2A adenosine G-protein-coupled receptor by conformational selection. *Nature* 533(7602):265–268.
96. Ghanouni P, et al. (2000) The effect of pH on beta(2) adrenoceptor function. Evidence for protonation-dependent activation. *J Biol Chem* 275(5):3121–7.
97. Neve K a (1991) Regulation of dopamine D2 receptors by sodium and pH. *Mol Pharmacol* 39(4):570–8.
98. Pert CB, Pasternak G, Snyder SH (1973) Opiate Agonists and Antagonists Discriminated by Receptor Binding in Brain. *Source Sci New Ser* 182(4119):1359–1361.
99. Snyder SH, Pasternak GW (2003) Historical review: Opioid receptors. *Trends Pharmacol Sci* 24(4):198–205.
100. Strasser A, Wittmann H-J, Schneider EH, Seifert R (2015) Modulation of GPCRs by monovalent cations and anions. *Naunyn Schmiedebergs Arch Pharmacol* 388(3):363–380.
101. Tsai BS, Lefkowitz RJ (1978) Agonist-specific effects of monovalent and divalent cations on adenylate cyclase-coupled alpha adrenergic receptors in rabbit platelets. *Mol Pharmacol* 14:540–548.
102. Blume AJA, Lichtshtein D, Boone G (1979) Coupling of opiate receptors to adenylate cyclase: requirement for Na+ and GTP. *Proc Natl Acad Sci U S A* 76(11):5626–30.
103. Selley DE, Cao CC, Liu Q, Childers SR (2000) Effects of sodium on agonist efficacy for G-protein activation in mu-opioid receptor-transfected CHO cells and rat thalamus. *Br J Pharmacol* 130(5):987–996.
104. Quitterer U, AbdAlla S, Jarnagin K, Müller-Esterl W (1996) Na+ ions binding to the bradykinin B2 receptor suppress agonist-independent receptor activation. *Biochemistry* 35(41):13368–77.
105. Seifert R, Wenzel-Seifert K (2002) Constitutive activity of G-protein-coupled receptors: cause of disease and common property of wild-type receptors. *Naunyn Schmiedeberg's Arch Pharmacol* 366:381–416.
106. Pasternak GW, Snowman AM, Snyder SH (1975) Selective enhancement of [3H]opiate agonist binding by divalent cations. *Mol Pharmacol* 11(6):735–44.
107. Pert CB, Synder SH (1974) Opiate Receptor Binding of Agonists and Antagonists Affected Differentially by Sodium. *Mol Pharmacol* 10(6):868–879.
108. Chen X, Wang Q, Ni F, Ma J (2010) Structure of the full-length Shaker potassium channel Kv1.2 by normal-mode-based X-ray crystallographic refinement. *Proc Natl Acad Sci U S A* 107(25):11352–7.
109. Oliver D, et al. (2001) Intracellular Anions as the Voltage Sensor of Protein, the Outer Hair Cell Motor Protein. *Science (80-)* 292(June):2340–2343.
110. Siefani E, Bezanilla F (1998) Cut-open oocyte voltage-clamp technique. *Methods Enzymol* 293(1987):300–318.
111. Bezanilla F (2008) How membrane proteins sense voltage. *Nat Rev Mol Cell Biol* 9(4):323–332.

112. Rinne A, Mobarec JC, Mahaut-Smith M, Kolb P, Bunemann M (2015) The mode of agonist binding to a G protein-coupled receptor switches the effect that voltage changes have on signaling. *Sci Signal* 8(401):ra110-ra110.
113. Rinne A, Birk A, Bünemann M (2013) Voltage regulates adrenergic receptor function. *Proc Natl Acad Sci U S A* 110(4):1536–41.
114. Gurung IS, Martinez-Pinna J, Mahaut-Smith MP (2008) Novel consequences of voltage-dependence to G-protein-coupled P2Y1 receptors. *Br J Pharmacol* 154(4):882–9.
115. Mahaut-Smith MP, Martinez-Pinna J, Gurung IS (2008) A role for membrane potential in regulating GPCRs? *Trends Pharmacol Sci* 29(8):421–429.
116. Martinez-Pinna J, Tolhurst G, Gurung IS, Vandenberg JI, Mahaut-Smith MP (2004) Sensitivity limits for voltage control of P2Y receptor-evoked Ca^{2+} mobilization in the rat megakaryocyte. *J Physiol* 555(Pt 1):61–70.
117. Ben Chaim Y, Bochnik S, Parnas I, Parnas H (2013) Voltage affects the dissociation rate constant of the m2 muscarinic receptor. *PLoS One* 8(9):e74354.
118. Ben-Chaim Y, et al. (2006) Movement of "gating charge" is coupled to ligand binding in a G-protein-coupled receptor. *Nature* 444(7115):106–9.
119. Ramoa AS, Mccormick DA (1994) Developmental Changes in Electrophysiological Properties of LGNd Neurons during Reorganization of Retinogeniculate Connections. 14(April).
120. Kandel ER, Schwartz JH, Jessell TM (2000) *Principles of Neural Science* doi:10.1036/0838577016.
121. Kupchik YM, et al. (2011) A novel fast mechanism for GPCR-mediated signal transduction--control of neurotransmitter release. *J Cell Biol* 192(1):137–51.
122. Yang M, Brackenbury WJ (2013) Membrane potential and cancer progression. *Front Physiol* 4 JUL(July):1–10.
123. Holcman D, Yuste R (2015) The new nanophysiology: regulation of ionic flow in neuronal subcompartments. *Nat Rev Neurosci* 16(October):685–692.
124. Zhou Y, et al. (2015) Membrane potential modulates plasma membrane phospholipid dynamics and K-Ras signaling. *Science (80-)* 349(6250):873–876.
125. Vickery ON, Machtens J-P, Zachariae U (2016) Membrane potentials regulating GPCRs: insights from experiments and molecular dynamics simulations. *Curr Opin Pharmacol* 30:44–50.
126. Navarro-Polanco R a, et al. (2011) Conformational changes in the M2 muscarinic receptor induced by membrane voltage and agonist binding. *J Physiol* 589(Pt 7):1741–1753.
127. Weichert D, et al. (2014) Covalent agonists for studying G protein-coupled receptor activation. *Proc Natl Acad Sci U S A* 111(29):10744–8.
128. Ring AM, et al. (2013) Adrenaline-activated structure of β2-adrenoceptor stabilized by an engineered nanobody. *Nature* 502(7472):575–9.
129. Rasmussen SGF, et al. (2011) Crystal structure of the β2 adrenergic receptor-Gs protein complex. *Nature* 477(7366):549–55.
130. Huang W, et al. (2015) Structural insights into μ-opioid receptor activation. *Nature* 524(7565):315–321.

131. Kruse AC, et al. (2013) Activation and allosteric modulation of a muscarinic acetylcholine receptor. *Nature* 504(7478):101–106.
132. McCammon JA, Gelin BR, Karplus M (1977) Dynamics of folded proteins. *Nature* 267(5612):585–590.
133. Leach AR (2001) *Molecular Modelling: Principles and Applications* doi:10.1093/bib/2.2.199.
134. Saito M (1994) Molecular dynamics simulations of proteins in solution: Artifacts caused by the cutoff approximation. *J Chem Phys* 101(5):4055–4061.
135. Darden T, York D, Pedersen L (1993) Particle mesh Ewald: An $N \cdot \log(N)$ method for Ewald sums in large systems. *J Chem Phys* 98(12):10089–10092.
136. Lindorff-Larsen K, et al. (2010) Improved side-chain torsion potentials for the Amber ff99SB protein force field. *Proteins* 78(8):1950–8.
137. Hornak V, et al. (2006) Comparison of multiple Amber force fields and development of improved protein backbone parameters. *Proteins Struct Funct Bioinforma* 65(3):712–725.
138. Berger O, Edholm O, Jähnig F (1997) Molecular dynamics simulations of a fluid bilayer of dipalmitoylphosphatidylcholine at full hydration, constant pressure, and constant temperature. *Biophys J* 72(May 1997):2002–2013.
139. Cordomí A, Caltabiano G, Pardo L (2012) Membrane protein simulations using AMBER force field and Berger lipid parameters. *J Chem Theory Comput* 8:948–958.
140. Berendsen HJC, Grigera JR, Straatsma TP (1987) The Missing Term in Effective Pair Potentials. *J Phys Chem* 91(24):6269–6271.
141. Jorgensen WL, Chandrasekhar J, Madura JD, Impey RW, Klein ML (1983) Comparison of simple potential functions for simulating liquid water. *J Chem Phys* 79(2):926–935.
142. Miyamoto S, Kollman PA (1992) Settle: An analytical version of the SHAKE and RATTLE algorithm for rigid water models. *J Comput Chem* 13(8):952–962.
143. Hess B, Bekker H, Berendsen HJC, Fraaije JGEM (1997) LINCS: A linear constraint solver for molecular simulations. *J Comput Chem* 18(12):1463–1472.
144. Feenstra KA, Hess B, Berendsen HJC (1999) Improving efficiency of large time-scale molecular dynamics simulations of hydrogen-rich systems. *J Comput Chem* 20(8):786—798.
145. Bussi G, Donadio D, Parrinello M (2007) Canonical sampling through velocity rescaling. *J Chem Phys* 126. doi:10.1063/1.2408420.
146. Kutzner C, Grubmüller H, de Groot BL, Zachariae U (2011) Computational electrophysiology: the molecular dynamics of ion channel permeation and selectivity in atomistic detail. *Biophys J* 101(4):809–17.
147. Kutzner C, et al. (2016) Biochimica et Biophysica Acta Insights into the function of ion channels by computational electrophysiology simulations. *BBA - Biomembr*. doi:10.1016/j.bbamem.2016.02.006.
148. Delemotte L, Tarek M, Klein ML, Amaral C, Treptow W (2011) Intermediate states of the Kv1.2 voltage sensor from atomistic molecular dynamics simulations. *Proc Natl Acad Sci* 108(15):6109–6114.
149. Khalili-Araghi F, et al. (2010) Calculation of the gating charge for the Kv1.2 voltage-activated

potassium channel. *Biophys J* 98(10):2189–2198.

150. Treptow W, Tarek M, Klein ML (2009) Initial response of the potassium channel voltage sensor to a transmembrane potential. *J Am Chem Soc* 131(6):2107–9.
151. Machtens JP, Briones R, Alleva C, de Groot BL, Fahlke C (2017) Gating Charge Calculations by Computational Electrophysiology Simulations. *Biophys J* 112(7):1396–1405.
152. Kumar S, Bouzida D, Swendsen RH, Kollman PA, Rosenberg JM (1992) The weighted histogram analysis method for free energy calculations on biomolecules. I. The method. *J Comput Chem* 13(8):1011–1021.
153. Haga K, et al. (2012) Structure of the human M2 muscarinic acetylcholine receptor bound to an antagonist. *Nature* 482(7386):547–551.
154. Šali A, Blundell TL (1993) Comparative Protein Modelling by Satisfaction of Spatial Restraints. *J Mol Biol* 234(3):779–815.
155. Case D, et al. (2016) Amber 2016.
156. Vickery ON, et al. (2018) Intracellular Transfer of Na + in an Active-State G-Protein-Coupled Receptor. *Structure* 26(1):171–180.e2.
157. Wolf MG, Hoefling M, Aponte-Santamaría C, Grubmüller H, Groenhof G (2010) G-membed: Efficient insertion of a membrane protein into an equilibrated lipid bilayer with minimal perturbation. *J Comput Chem* 31:2169–2174.
158. Berendsen HJC, Postma JPM, van Gunsteren WF, DiNola A, Haak JR (1984) Molecular dynamics with coupling to an external bath. *J Chem Phys* 81:3684–3690.
159. Pronk S, et al. (2013) GROMACS 4.5: a high-throughput and highly parallel open source molecular simulation toolkit. *Bioinformatics* 29(7):845–854.
160. Abraham MJ, et al. (2015) GROMACS: High performance molecular simulations through multi-level parallelism from laptops to supercomputers. *SoftwareX* 1–2:19–25.
161. Hub JS, De Groot BL, Van Der Spoel D (2010) G_wham a free Weighted Histogram Analysis implementation including robust error and autocorrelation estimates. *J Chem Theory Comput* 6:3713–3720.
162. Bashford D, Gerwert K (1992) Electrostatic calculations of the pKa values of ionizable groups in bacteriorhodopsin. *J Mol Biol* 224(2):473–486.
163. Baptista AM, Martel PJ, Soares CM (1999) Simulation of Electron-Proton Coupling with a Monte Carlo Method: Application to Cytochrome c3 Using Continuum Electrostatics. *Biophys J* 76(6):2978–2998.
164. Metropolis N, Rosenbluth AW, Rosenbluth MN, Teller AH, Teller E (1953) Equation of state calculations by fast computing machines. *J Chem Phys* 21(6):1087–1092.
165. Ridgway N, McLeod R (2015) *Biochemistry of Lipds, Lipoproteins and Membranes* (Elsevier).
166. Martinez-Pinna J, et al. (2005) Direct voltage control of signaling via P2Y1 and other Gαq-coupled receptors. *J Biol Chem* 280(2):1490–1498.
167. Sahlholm K, Nilsson J, Marcellino D, Fuxe K, Århem P (2008) Voltage-dependence of the human dopamine D2 receptor. *Synapse* 62(6):476–480.
168. Ben-Chaim Y, et al. (2006) Movement of /`gating charge/' is coupled to ligand binding in a G-

protein-coupled receptor. *Nature* 444(7115):106–109.

169. Souza CS, Amaral C, Treptow W (2014) Electric fingerprint of voltage sensor domains. *Proc Natl Acad Sci U S A* 111(49):17510–5.
170. Wang H-B, et al. (2010) Coexpression of delta- and mu-opioid receptors in nociceptive sensory neurons. *Proc Natl Acad Sci* 107(29):13117–13122.
171. Peng J, Sarkar S, Chang SL (2012) Opioid receptor expression in human brain and peripheral tissues using absolute quantitative real-time RT-PCR. *Drug Alcohol Depend* 124(3):223–8.
172. Shang Y, et al. (2014) Mechanistic Insights into the Allosteric Modulation of Opioid Receptors by Sodium Ions. *Biochemistry* 53(31):5140–9.
173. Dong H, Fiorin G, Carnevale V, Treptow W, Klein ML (2013) Pore waters regulate ion permeation in a calcium release-activated calcium channel. *Proc Natl Acad Sci U S A* 110:17332–7.
174. Hyeon C, Thirumalai D (2003) Can energy landscape roughness of proteins and RNA be measured by using mechanical unfolding experiments? *Proc Natl Acad Sci U S A* 100(18):10249–10253.
175. Nevo R, Brumfeld V, Kapon R, Hinterdorfer P, Reich Z (2005) Direct measurement of protein energy landscape roughness. *EMBO Rep* 6(5):482–486.
176. Miao Y, Caliman AD, McCammon JA (2015) Allosteric Effects of Sodium Ion Binding on Activation of the M3 Muscarinic G-Protein-Coupled Receptor. *Biophys J* 108(7):1796–1806.
177. Selent J, Sanz F, Pastor M, de Fabritiis G (2010) Induced effects of sodium ions on dopaminergic G-protein coupled receptors. *PLoS Comput Biol* 6(8). doi:10.1371/journal.pcbi.1000884.
178. Zhang XC, Sun K, Zhang L, Li X, Cao C (2013) GPCR activation: protonation and membrane potential. *Protein Cell* 4(10):747–60.
179. Zhang XC, Cao C, Zhou Y, Zhao Y (2014) Proton transfer-mediated GPCR activation. *Protein Cell*. doi:10.1007/s13238-014-0106-4.
180. Ranganathan A, Dror RO, Carlsson J (2014) Insights into the Role of $Asp79^{2.50}$ in β2 Adrenergic Receptor Activation from Molecular Dynamics Simulations. *Biochemistry* 53(46):7283–7296.
181. Kralj JM, Hochbaum DR, Douglass AD, Cohen AE (2011) Electrical Spiking in Escherichia coli Probed with a Fluorescent Voltage-Indicating Protein. *Science (80-)* 333(6040):345–348.
182. Pardo LA, Stühmer W (2014) The roles of K^+ channels in cancer. *Nat Rev Cancer* 14(1):39–48.
183. Ben-Chaim Y, Tour O, Dascal N, Parnas I, Parnas H (2003) The M2 muscarinic G-protein-coupled receptor is voltage-sensitive. *J Biol Chem* 278(25):22482–91.
184. Dekel N, Priest MF, Parnas H, Parnas I, Bezanilla F (2012) Depolarization induces a conformational change in the binding site region of the M2 muscarinic receptor. *Proc Natl Acad Sci* 109(1):285–290.
185. Massink A, et al. (2015) Sodium Ion Binding Pocket Mutations and Adenosine A2A Receptor Function. *Mol Pharmacol* 87(2):305–313.
186. Massink A, et al. (2016) 5′-Substituted Amiloride Derivatives as Allosteric Modulators Binding in the Sodium Ion Pocket of the Adenosine A 2A Receptor. *J Med Chem* 59(10):4769–4777.
187. Vanni S, Neri M, Tavernelli I, Rothlisberger U (2010) A Conserved Protonation-Induced Switch

can Trigger “Ionic-Lock” Formation in Adrenergic Receptors. *J Mol Biol* 397(5):1339–1349.

188. Palczewski K, et al. (2000) Crystal structure of rhodopsin: A G protein-coupled receptor. *Science* 289(5480):739–45.
189. Venkatakrishnan a J, et al. (2013) Molecular signatures of G-protein-coupled receptors. *Nature* 494(7436):185–94.
190. Huang W, et al. (2015) Structural insights into mu-opioid receptor activation. *Nature* 524:315–21.
191. Yuan S, Peng Q, Palczewski K, Vogel H, Filipek S (2016) Mechanistic Studies on the Stereoselectivity of the Serotonin 5-HT 1A Receptor. *Angew Chemie Int Ed* 55(30):8661–8665.
192. Peterson YK, Luttrell LM (2017) The Diverse Roles of Arrestin Scaffolds in G Protein–Coupled Receptor Signaling. *Pharmacol Rev Pharmacol Rev* 69(July):256–297.
193. Mahoney JP, Sunahara RK (2016) Mechanistic insights into GPCR-G protein interactions. *Curr Opin Struct Biol* 41:247–254.
194. Dror RO, et al. (2015) Structural basis for nucleotide exchange in heterotrimeric G proteins. *Science (80-)* 348(6241):1361–1365.
195. Ranjan R, Dwivedi H, Baidya M, Kumar M, Shukla AK (2017) Novel Structural Insights into GPCR–β-Arrestin Interaction and Signaling. *Trends Cell Biol* xx:1–12.
196. Maguire ME, Van Arsdale PM, Gilman a G (1976) An agonist-specific effect of guanine nucleotides on binding to the beta adrenergic receptor. *Mol Pharmacol* 12:335–339.
197. Liu W, et al. (2012) Structural Basis for Allosteric Regulation of GPCRs by Sodium Ions. *Science (80-)* 337(6091):232–236.
198. Zhu F, Hummer G (2012) Drying transition in the hydrophobic gate of the GLIC channel blocks ion conduction. *Biophys J* 103(2):219–227.
199. Beckstein O, et al. (2003) Ion channel gating: Insights via molecular simulations. *FEBS Lett* 555(1):85–90.
200. Shang Y, et al. (2014) Mechanistic insights into the allosteric modulation of opioid receptors by sodium ions. *Biochemistry* 53(31):5140–9.
201. Thomsen ARB, et al. (2016) GPCR-G Protein-B-Arrestin Super-Complex Mediates Sustained G Protein Signaling. *Cell* 166(4):907–919.
202. Kobilka BK, Deupi X (2007) Conformational complexity of G-protein-coupled receptors. *Trends Pharmacol Sci* 28(8):397–406.
203. Isom D, et al. (2013) Protons as second messenger regulators of G protein signaling. *Mol Cell* 51(4):531–538.
204. Moreno-Galindo EG, Alamilla J, Sanchez-Chapula JA, Tristani-Firouzi M, Navarro-Polanco RA (2016) The agonist-specific voltage dependence of M2 muscarinic receptors modulates the deactivation of the acetylcholine-gated K+ current (I KACh). *Pflügers Arch - Eur J Physiol*. doi:10.1007/s00424-016-1812-y.
205. Heifetz A, James T, Morao I, Bodkin MJ, Biggin PC (2016) Guiding lead optimization with GPCR structure modeling and molecular dynamics. *Curr Opin Pharmacol* 30:14–21.
206. Margolis EB, Fujita W, Devi LA, Fields HL (2017) Two delta opioid receptor subtypes are functional in single ventral tegmental area neurons, and can interact with the mu opioid receptor.

Neuropharmacology 123:420–432.

207. Malinsky J, Tanner W, Opekarova M (2016) Transmembrane voltage: Potential to induce lateral microdomains. *Biochim Biophys Acta - Mol Cell Biol Lipids* 1861(8):806–811.
208. Pavlos NJ, Friedman PA (2016) GPCR signaling and trafficking: the long and short of it. *Trends Endocrinol Metab* 28(3):Ahead of print.
209. Pardo L, Deupi X, Dölker N, López-Rodríguez ML, Campillo M (2007) The role of internal water molecules in the structure and function of the rhodopsin family of G protein-coupled receptors. *ChemBioChem* 8(1):19–24.
210. Vroling B, et al. (2010) GPCRDB: information system for G protein-coupled receptors. *Nucleic Acids Res* 39:D309–D319.
211. Mahalingam M, Martínez-Mayorga K, Brown MF, Vogel R (2008) Two protonation switches control rhodopsin activation in membranes. *Proc Natl Acad Sci U S A* 105(46):17795–17800.
212. Wang S, et al. (2017) D 4 dopamine receptor high-resolution structures enable the discovery of selective agonists. 386(October):381–386.
213. Carpenter B, Tate CG (2017) Active state structures of G protein-coupled receptors highlight the similarities and differences in the G protein and arrestin coupling interfaces. *Curr Opin Struct Biol* 45(Figure 1):124–132.
214. Scheer A, Fanelli F, Costa T, De Benedetti PG, Cotecchia S (1997) The activation process of the alpha1B-adrenergic receptor: potential role of protonation and hydrophobicity of a highly conserved aspartate. *Proc Natl Acad Sci U S A* 94(3):808–813.
215. Arnis S, Fahmy K, Hofmann KP, Sakmar TP (1994) A conserved carboxylic acid group mediates light-dependent proton uptake and signaling by rhodopsin. *J Biol Chem* 269(39):23879–81.
216. Neve KA, Cox B a, Henningsen R a, Spanoyannis A, Neve RL (1991) Pivotal role for aspartate-80 in the regulation of dopamine D2 receptor affinity for drugs and inhibition of adenylyl cyclase. *Mol Pharmacol* 39:733–739.
217. Neve A of Dopamine D2 Receptors by Sodium and pH.
218. Barchad-Avitzur O, et al. (2016) A Novel Voltage Sensor in the Orthosteric Binding Site of the M2 Muscarinic Receptor. *Biophys J* 111(7):1396–1408.

Chapter 8. Appendix

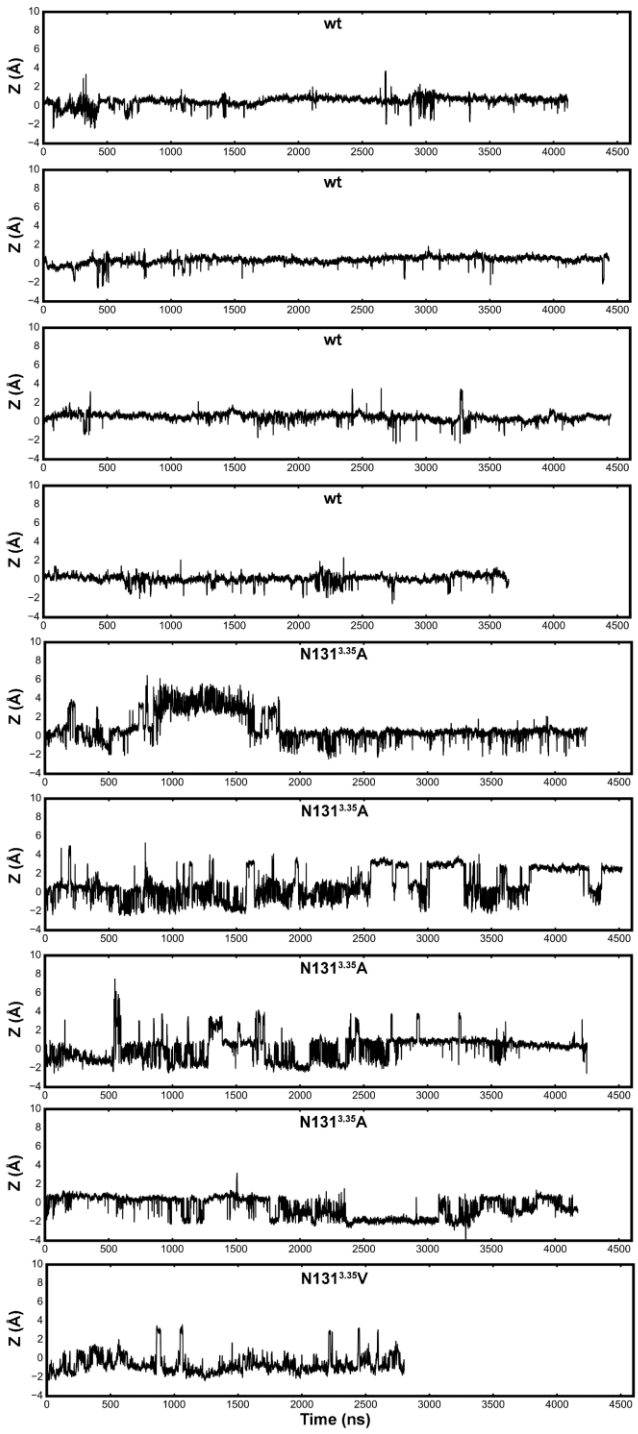

Appendix Figure 8-1: Effect of the N131$^{3.35}$ mutation upon Na^+ binding

Z-coordinate of the allosteric Na^+ ion bound within the Na^+ binding pocket in the wt δ-OR, N131$^{3.35}$A and the N131$^{3.35}$V δ-OR mutants. This figure shows the increasing destabilisation of the Na^+ ion within the N131$^{3.35}$ mutant receptors.

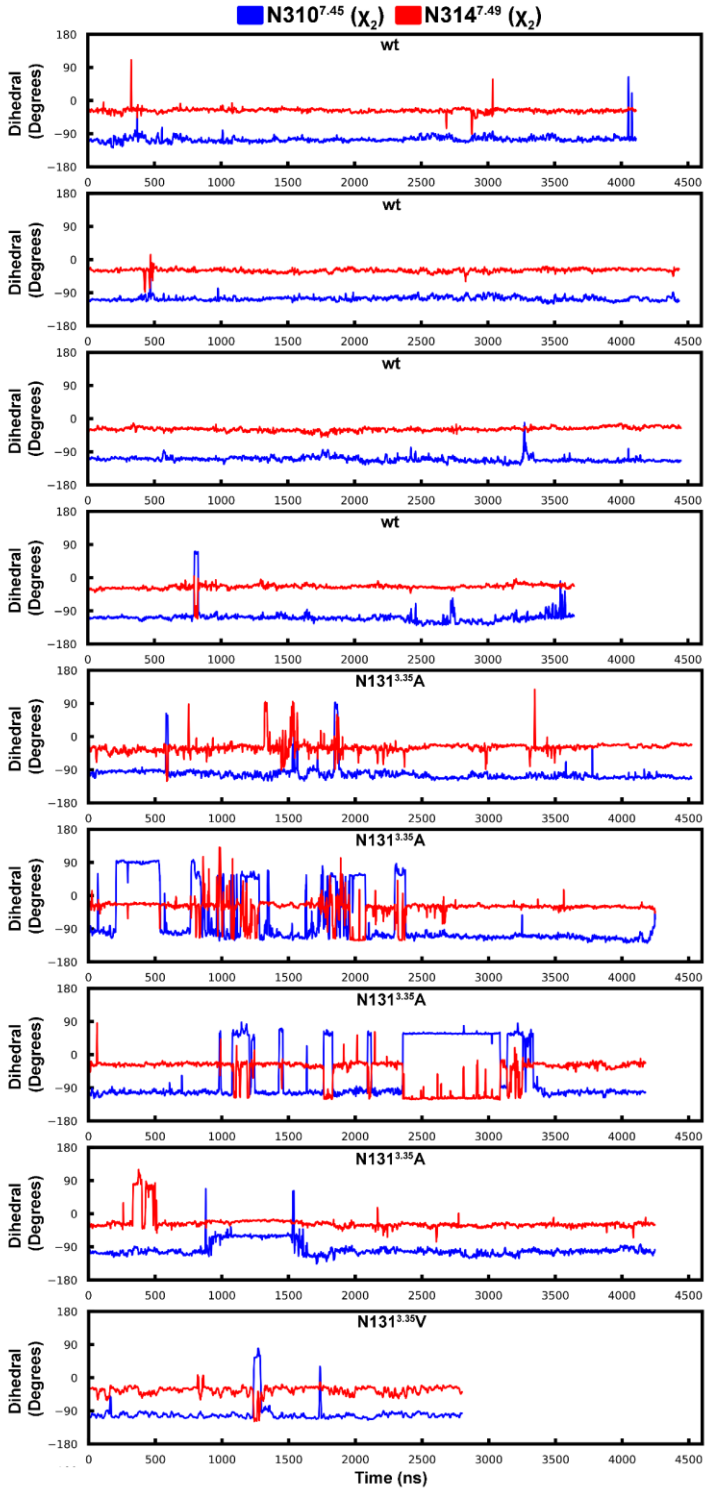

Appendix Figure 8-2: Effects of a charged D95$^{2.50}$ and D145$^{3.49}$ upon the Na^+ binding pocket

The dihedral angle χ_2 of the N310$^{7.45}$ (blue) and the N314$^{7.49}$ (red) sidechains. Shown here is the slight destabilisation of the Na^+ binding pocket upon mutation of N131$^{3.35}$, in contrast to the wt receptor.

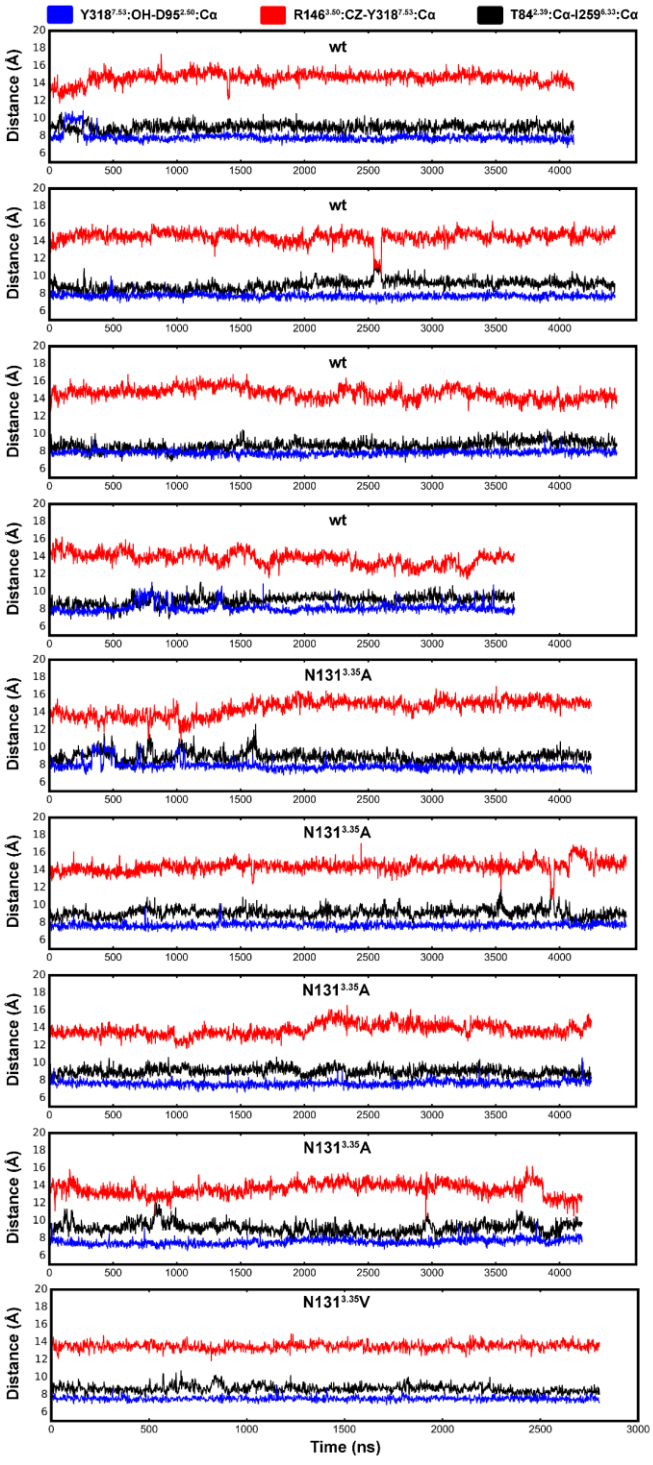

Appendix Figure 8-3: Activation criteria for the δ-OR with a charged D95$^{2.50}$ and D145$^{3.49}$

The criteria for the activation of the δ-OR receptor. With a negatively charged D95$^{2.50}$ and D145$^{3.49}$, both the wt and two δ-OR mutants do not deviate from their inactive state. Shown here the distance between Y318$^{7.53}$-OH and D95$^{2.50}$-Cα (blue), R146$^{3.50}$-CZ and Y318$^{7.53}$-Cα (red), and T84-Cα and I259-Cα (black).

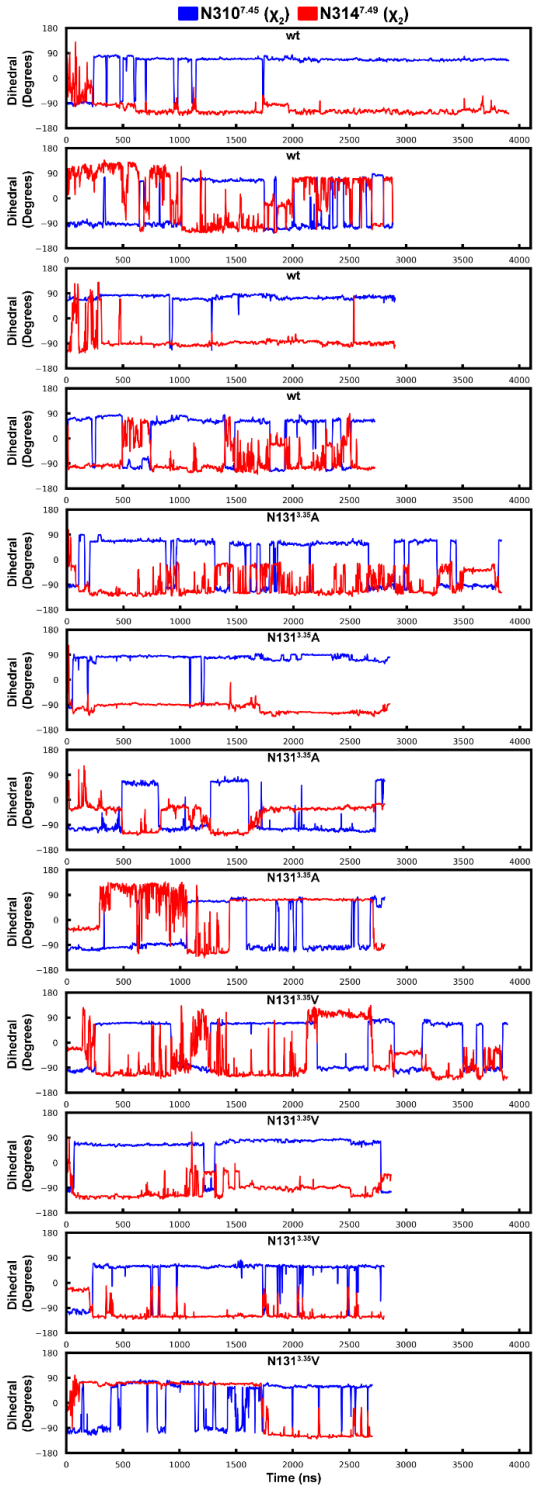

Appendix Figure 8-4: Effects of a neutral D95$^{2.50}$ and charged D145$^{3.49}$ upon the Na^+ binding pocket

The dihedral angle χ_2 of the N310$^{7.45}$ (blue) and the N314$^{7.49}$ (red) sidechains. Demonstrated here, is the destabilisation of the Na^+ binding pocket upon the protonation of D95$^{2.50}$.

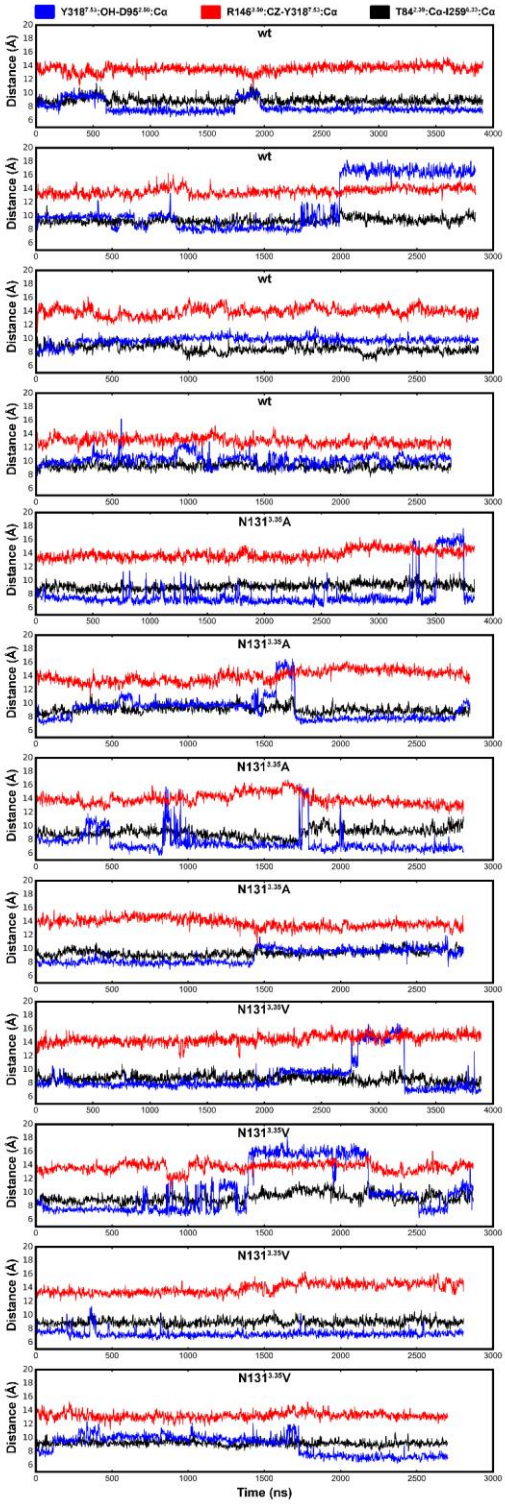

Appendix Figure 8-5: Activation criteria for the δ-OR with a neutral D95$^{2.50}$ and charged D145$^{3.49}$

The criterion for the activation of the δ-OR receptor. With a neutral D95$^{2.50}$, both the wt and two δ-OR mutants do not fulfil the criteria for the active conformation. The protonation of D95$^{2.50}$ increases the conformational flexibility of Y318$^{7.53}$, in which the inactive, intermediate and downward conformation is observed. The distance between Y318$^{7.53}$-OH and D95$^{2.50}$-Cα (blue), R146$^{3.50}$-CZ and Y318$^{7.53}$-Cα (red), and T84-Cα and I259-Cα (black).

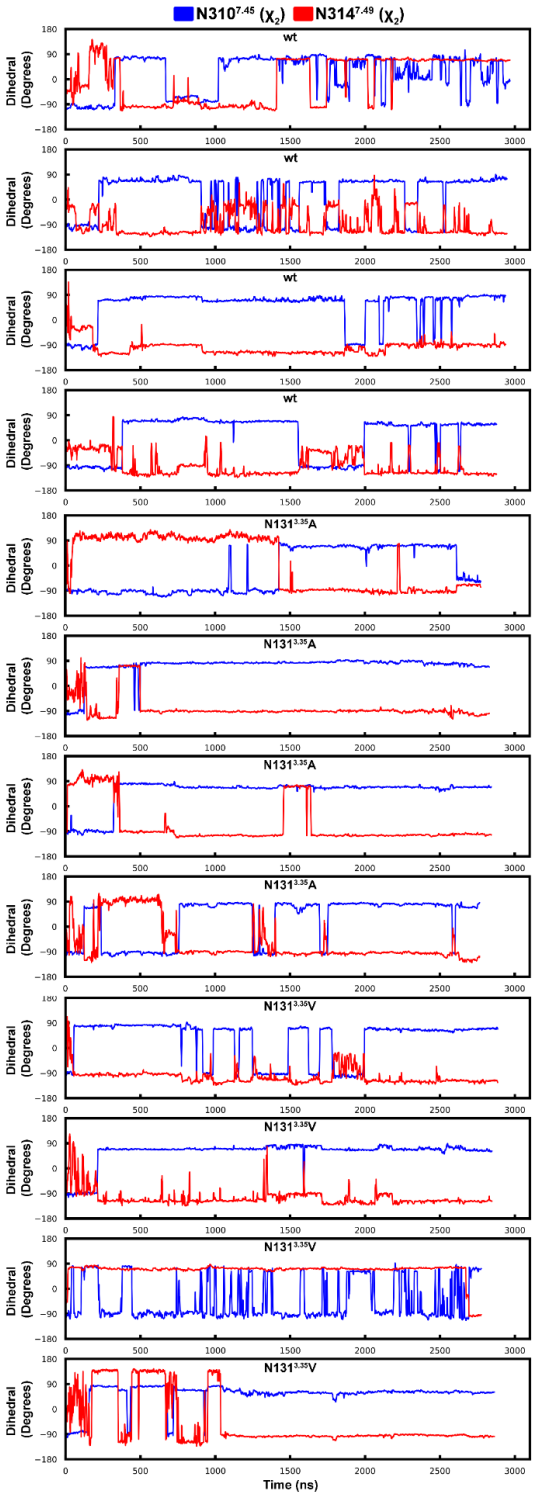

Appendix Figure 8-6: Effects of a neutral D95$^{2.50}$ and D145$^{3.49}$ upon the Na^+ binding pocket

The dihedral angle χ_2 of the N310$^{7.45}$ (blue) and the N314$^{7.49}$ (red) sidechains. Demonstrated here, is the destabilisation of the Na^+ binding pocket upon the protonation of D95$^{2.50}$ and D145$^{3.49}$.

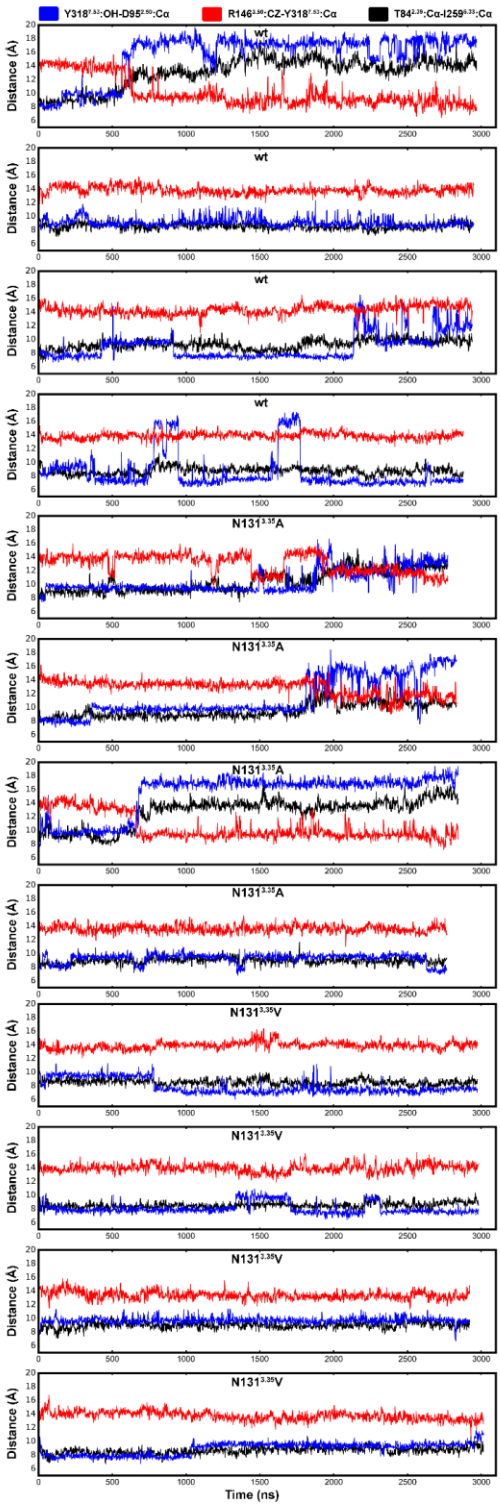

Appendix Figure 8-7: Activation criteria for the δ-OR with a neutral D95$^{2.50}$ and D145$^{3.49}$

The criteria for the activation of the δ-OR receptor. With a neutral D95$^{2.50}$, both the wt and two δ-OR mutants **(A-C)** do not fulfil the criteria for the active conformation. The protonation of D95$^{2.50}$ increases the conformational flexibility of Y318$^{7.53}$, in which the inactive, intermediate and downward conformation is observed. The distance between Y318$^{7.53}$-OH and D95$^{2.50}$-Cα (blue), R146$^{3.50}$-CZ and Y318$^{7.53}$-Cα (red), and T84-Cα and I259-Cα (black).

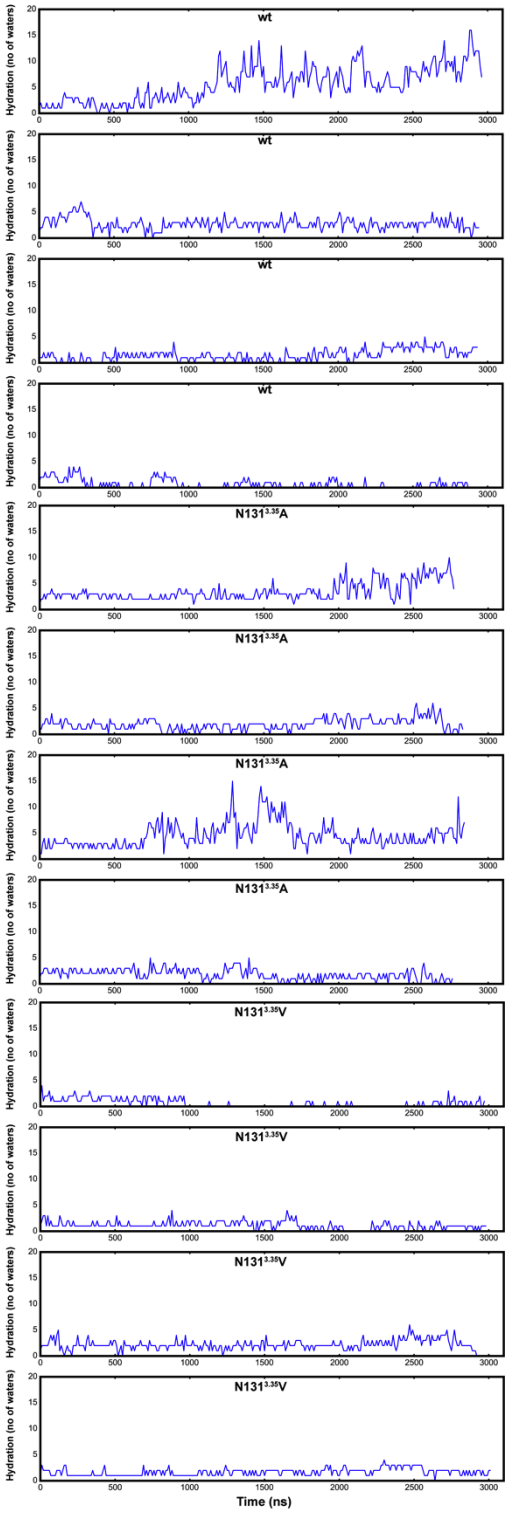

Appendix Figure 8-8: Hydration of the hydrophobic layer

The hydration of the hydrophobic layer upon δ-OR activation. The water molecules were counted every 10 ns, between a distance of Δz = -4Å from the D95$^{2.50}$ Cα atom and towards the intracellular with the z-coordinate of the R146$^{3.50}$ Cα.